

DESIGN, PRODUCTION AND PERFORMANCE ANALYSIS OF A MULTI-
PASS MATRIX OPTICAL SYSTEM FOR TRACE SPECTROSCOPY

A THESIS SUBMITTED TO
THE GRADUATE SCHOOL OF NATURAL AND APPLIED SCIENCES
OF
MIDDLE EAST TECHNICAL UNIVERSITY

BY

TUBA ÖNDER AKSAN

IN PARTIAL FULFILLMENT OF THE REQUIREMENTS
FOR
THE DEGREE OF MASTER OF SCIENCE
IN
PHYSICS

SEPTEMBER 2021

Approval of the thesis:

**DESIGN, PRODUCTION AND PERFORMANCE ANALYSIS OF A
MULTI-PASS MATRIX OPTICAL SYSTEM FOR TRACE
SPECTROSCOPY**

submitted by **TUBA ÖNDER AKSAN** in partial fulfillment of the requirements for
the degree of **Master of Science in Physics, Middle East Technical University** by,

Prof. Dr. Halil Kalıpçılar
Dean, Graduate School of **Natural and Applied Sciences**

Prof. Dr. Seçkin Kürkcüoğlu
Head of the Department, **Physics**

Assoc. Prof. Dr. Alpan Bek
Supervisor, **Physics, METU**

Dr. Ulaş Kürüm
Co-Supervisor, **Roketsan Inc.**

Examining Committee Members:

Prof. Dr. Barış Akaoglu
Physics Engineering, Ankara University

Assoc. Prof. Dr. Alpan Bek
Physics, METU

Prof. Dr. Raşit Turan
Physics, METU

Date: 09.09.2021

I hereby declare that all information in this document has been obtained and presented in accordance with academic rules and ethical conduct. I also declare that, as required by these rules and conduct, I have fully cited and referenced all material and results that are not original to this work.

Name Last name : Tuba Önder Aksan

Signature :

ABSTRACT

DESIGN, PRODUCTION AND PERFORMANCE ANALYSIS OF A MULTI-PASS MATRIX OPTICAL SYSTEM FOR TRACE SPECTROSCOPY

Önder Aksan, Tuba
Master of Science, Physics
Supervisor: Assoc. Prof. Dr. Alpan Bek
Co-Supervisor: Dr. Ulaş Kürüm

September 2021, 103 pages

The design and fabrication of a multi-pass matrix optical system (MMS) for the atmospheric trace gas measurement system planned to be established is described. The measurement system is a sealed thermal vacuum-capable chamber in which synthetic atmosphere configurations can be obtained by releasing various gases into the system. To increase the sensitivity of spectroscopic measurements, a MMS is designed to extend the optical path inside the chamber. The system, which is a modified Chernin cell design consisting of three objectives and two field mirrors, is adjustable to acquire up to 288 passes along the cavity. The design parameters of the system and the optimum configuration have been determined and simulated utilizing ray tracing technique with OpticStudio. Performance output and optical aberrations have been analyzed. As a result of the analysis, it has been shown that the geometric loss and astigmatism is negligible, off-axis angles are small, and the focal features are preserved. Performance experiments of the MMS were performed using a supercontinuum laser through an optical cuvette placed in open atmosphere environment. Two types of samples are chosen to simulate absorber and scatterer

behaviour. Absorption and scattering spectroscopy in the visible region of crystal violet (CV) and polypropylene (PP) were performed for different passage numbers and different concentrations. As a result of the measurements, the optimum number for the measurement system with a cuvette was determined as 32 with 4x4 matrix arrangement. The detection limit for CV is found to be 2.48 nM and for PP 16.8 μ M. The results have been compared to alternative spectroscopy techniques. They show that; the system can be used for detection measurements of molecules and scattering microparticles in many fields ranging from atmospheric studies to environmental science. It offers a reliable, simple, inexpensive, fast and portable solution that can compete with other measurement techniques.

Keywords: Mirror System Design, Optical Fabrication, Atmospheric Transmittance, Absorption and Scattering Spectroscopy

ÖZ

ESER MİKTARDA BULUNAN MADDE SPEKTROSKOPİSİ İÇİN ÇOKLU GEÇİŞ MATRİS OPTİK SİSTEMİ TASARIMI, ÜRETİMİ VE PERFORMANSI

Önder Aksan, Tuba
Yüksek Lisans, Fizik
Tez Yöneticisi: Doç. Dr. Alpan Bek
Ortak Tez Yöneticisi: Dr. Ulaş Kürüm

Eylül 2021, 103 sayfa

Bu çalışmada, kurulması planlanan atmosferik eser gaz ölçüm sistemi için çok geçişli matris optik sistemin (ÇGMS) tasarımı ve üretimi anlatılmaktadır. Ölçüm sistemi, çeşitli termal koşullarda sisteme çeşitli atmosferik gazların salınmasıyla sentetik atmosfer konfigürasyonlarının elde edilebildiği, sızdırmaz vakumlu bir odadır. ÇGMS, spektroskopik ölçümlerin hassasiyetini artırmak amacıyla, kavite içindeki optik yolu uzatmak için tasarlanmıştır. Üç objektif ve iki alan aynasından oluşan modifiye edilmiş bir Chernin hücre tasarımı olan optik sistem, kavite boyunca 288'e kadar geçiş elde etmek için ayarlanabilmektedir. Ayna sisteminin tasarım parametreleri ve optimum konfigürasyon, OpticStudio yazılımı ile ışın izleme tekniği kullanılarak simüle edilmiştir. Simülasyon sonucu performans çıktısı ve optik kusurlar analiz edilmiştir. Analiz sonucunda geometrik kaybın ve astigmatizmin ihmal edilebilir olduğu, eksen dışı açıların küçük olduğu ve odak özelliklerinin korunduğu gösterilmiştir. ÇGMS'nin performans deneyleri, açık atmosfer ortamına yerleştirilmiş bir optik kuvvet aracılığıyla süper sürekli lazer kullanılarak gerçekleştirilmiştir. Soğurucu ve saçıcı davranışını simüle etmek için iki tip numune seçilmiştir. Kristal viyole (CV) ve polipropilen (PP) için görünür spektral

bölgede farklı geçiş sayıları ve farklı konsantrasyonlar için soğurum ve saçılma spektroskopisi yapılmıştır. Analiz sonucunda küvetli ölçüm sistemi için optimum geçiş sayısı 4x4 matris düzeni ile 32 olarak belirlenmiştir. CV için minimum algılama limitinin 2.48 nM ve PP için 16.8 µM olduğu bulunmuştur. Sonuçlar alternatif spektroskopi teknikleri ile karşılaştırılmıştır. Performans çalışmaları ve karşılaştırmalar ÇGMS'nin atmosferik çalışmalardan çevre bilimine kadar birçok alanda moleküllerin ve saçıcı mikropartiküllerin tespit ölçümleri için kullanılabilir olduğunu göstermektedir. Sistem, diğer ölçüm teknikleri ile rekabet edebilir, güvenilir, basit, düşük maliyetli, hızlı ve taşınabilir bir çözüm sunmaktadır.

Anahtar Kelimeler: Ayna Sistemi Tasarımı, Optik Üretimi, Atmosferik Geçirgenlik, Soğurum ve Saçılım Spektroskopisi

To my brother

ACKNOWLEDGMENTS

I wish to express my deepest gratitude to my supervisor Assoc. Prof. Dr. Alpan BEK for his constant guidance, valuable advice, criticism, encouragements and insight throughout the research.

I am grateful to my co-advisor, Dr. Ulaş KÜRÜM, for his unwavering support and for taking me one step further every day in my career and academic life. I feel lucky to have had the opportunity to work with such a visionary team leader in my business life.

Special thanks to Roketsan Missiles Inc. for providing both financial and technical opportunities to complete this study.

I would like to thank my manager Ali Şimşek TEKEREK for supporting my master education.

Special thanks to METU Environmental Engineering Department for providing microplastic samples for use in my studies.

Many thanks to my dear friends Sinan ÇELİK and Hudayberdi GURDOV for their friendship and fruitful scientific discussions throughout my undergraduate and graduate education.

I would like to express my deepest gratitude to my mother Arzu ÖNDER, my father, Ali ÖNDER and my brother, Burak ÖNDER for their continuous support and encouragement through all my life. They have always strived to provide everything necessary for me to get the best education.

Last but not least, I would like to thank to my husband Çağrı AKSAN for his love, endless patience and faith in me. I am grateful for always making me feel happy, peaceful and strong.

TABLE OF CONTENTS

ABSTRACT.....	v
ÖZ.....	vii
ACKNOWLEDGMENTS	x
TABLE OF CONTENTS.....	xi
LIST OF TABLES	xiii
LIST OF FIGURES	xiv
1 INTRODUCTION	1
1.1 Spectral Signature Studies in Defence Applications.....	2
1.1.1 Thermal Emission and Blackbody Radiation.....	2
1.1.2 Spectral Signature	4
1.1.3 Atmospheric Absorption.....	5
1.1.4 Spectral Modelling of Atmospheric Effects	8
1.1.5 Atmospheric Trace Gas Measurement System	11
1.2 Molecular Absorbant Spectroscopy (Crystal Violet).....	13
1.3 Scattering Microparticles Spectroscopy (Microplastics)	15
1.4 Multi-pass Mirror Designs	15
1.4.1 White Cell Design.....	15
1.4.2 Modified White Cell Designs	18
1.4.3 Chernin Cell Design.....	21
2 THE OPTICAL SYSTEM	23

2.1	Optimum Cell Design Criteria	23
2.2	Design of the Optical System	24
2.2.1	Definition of Optical Design Parameters	28
2.2.1.1	Number of Passes	28
2.2.1.2	Mirror Dimensions	32
2.2.1.3	Path Length	35
2.2.1.4	Resolution	35
2.2.2	The Design Process	36
2.2.3	Simulation Analysis.....	44
2.2.4	Tolerancing.....	52
2.3	Production of the Optical System	56
2.3.1	Materials of the Optics	57
2.3.2	Optomechanical Mounts.....	64
3	EXPERIMENTAL RESULTS AND PERFORMANCE ANALYSIS	67
3.1	Instruments and Experimental Setup	67
3.2	Trace Detection of a Molecular Absorber	70
3.3	Trace Detection of a Microscopic Scatterers	77
3.4	Limit of Detections	79
4	DISCUSSION & CONCLUSION.....	81
	REFERENCES	93
	APPENDIX A	103

LIST OF TABLES

TABLES

Table 1 The Tunable Laser Absorption Spectroscopy (TLAS) equipments coupled to the trace gas measurement system	12
Table 2 Limit of Detection of CV measurements and methods.....	14
Table 3 Several beam characteristics of lasers to be used.	33
Table 4 Best resolutions obtainable by the multi-pass matrix optical system according to different spectral ranges.	36
Table 5 Positions of multi-pass optics in mm.	42
Table 6 Power analysis of incoming and outgoing beams.....	45
Table 7 Spot information of laser beams at different wavelengths.....	49
Table 8 The Zernike coefficients and corresponding optical aberrations at 600 nm wavelength.	51
Table 9 The basic properties of multi-pass matrix optical system after tolerancing analysis.....	55
Table 10 Specifications of silver and gold coating.....	58
Table 11 Surface map of multi-pass matrix optics with surface irregularity (PV) and roughness (RMS) values.	63
Table 12 Specifications of the optics of multi-pass matrix system after manufacturing.	64
Table 13 PV and RMS values of surface of T ₁ before and after bonding process..	66
Table 14 General properties of absorption cuvette [59].	69
Table 15 Several specifications of PP type microplastics.	77
Table 16 Comparison of different methods to detect trace amount of crystal violet.	90

LIST OF FIGURES

FIGURES

Figure 1 Spectral radiative power of a blackbody $R(\lambda,T)$ vs wavelength, λ at different temperatures [4].	3
Figure 2 Spectral signature modeling of a target obtained via FEMVIEW IR software [5].	4
Figure 3 The vertical profile of the mixing ratio of the atmospheric components according to the US Standard Model of Atmosphere [6].	6
Figure 4 Atmospheric transmission for 1.8 km horizontal path at sea level [3].	7
Figure 5 Atmospheric transmission graph in the spectral range of 1-5 μm at 23 km and 5 km altitude [10].	8
Figure 6 Atmospheric transmission as measured with a spectroradiometer at 6.5 km distance between the spectral range 2 and 14 μm [13].	9
Figure 7 The vertical temperature profile of the atmosphere between 0-100 km altitude according to US Standard Model of Atmosphere [6].	10
Figure 8 Schematic representation of atmospheric trace gas measurement system.	12
Figure 9 The chemical structure of crystal violet [16].	13
Figure 10 (a) White cell design. (b) Photograph of White cell. (c) Images on the field mirror.	16
Figure 11 (a) Bernstein and Herzberg's multi-pass mirror design. (b) Images on the field mirror.	16
Figure 12 (a) Tobin <i>et. al.</i> multi-pass mirror design. (b) Images on the field mirror.	17
Figure 13 (a) Hanst's multi-pass matrix design. (b) Images on the field mirror group.	18
Figure 14(a) Horn and Pimentel's multi-pass matrix design. (b) Number of images on the field mirror group.	19
Figure 15 (a) Photograph of Herriott cell. (b) Images on mirrors of Herriott cell.	19

Figure 16 (a) Doussin <i>et. al.</i> 's multi-pass matrix system. (b) Images of field mirror group.	20
Figure 17 (a) Chernin's multi-pass matrix three objective system. 1-entrance aperture, 2-exit aperture, 3,4,10-objective mirrors, 5-turning plate, 6-holder, 7-vertical axis, 8,9-Field mirrors, 11-horizontal axis. (b) Objective mirror group. 3,4,5,6- objective mirrors, 7-mirror holder, 8-vertical axis, 9-horizontal axis, 10'-11'- curvature centers of field mirrors. (c) Field mirror group. 1-entrance aperture, 2-exit aperture, 3'-6'-curvature centers of objective mirrors, 10,11-field mirrors [1].	21
Figure 18 Chernin's modified three objective multi-pass matrix system. 1-entrance aperture, 2-exit aperture, 8,9-field mirrors.....	22
Figure 19 Three objective multi-pass matrix system scheme.	25
Figure 20 Images of the field mirror T ₁ and T ₂	26
Figure 21 Typical reflectance curves for metallic mirror coatings from near-infrared to mid-infrared region [51].	29
Figure 22 Technical drawing of field mirrors T ₁ and T ₂	34
Figure 23 Flow chart of the design process of multi-pass matrix optical system...	37
Figure 24 Wavelengths section in System Explorer tab.	39
Figure 25 Non-sequential component editor in OpticStudio.	39
Figure 26 Aperture definition for T ₁ and T ₂ field mirrors.	40
Figure 27 Solid models of multi-pass mirrors.	41
Figure 28 (a) The detector placed at the point where the light reflected from O ₁ aims to hit. (b) Spot position on the detector before optimization. (c) Spot position on the detector after optimization.	42
Figure 29 (a) Criteria settings in optimization wizard. (b) Local Optimization tab. (c) Merit Function Editor.	43
Figure 30 Shaded Model of multi-pass matrix optical system designed via Zemax OpticStudio Software.	44

Figure 31 Spatial irradiance distribution of simulated incoming (a) and outgoing (b) gaussian laser beams and cross section graphs of incoming (c) and outgoing (d) gaussian laser beams.....	45
Figure 32 Reflection vs wavelength graph of protected silver coating in OpticStudio.	46
Figure 33 Power density vs wavelength graph of NKT Compact Supercontinuum White Light Laser [53].	47
Figure 34 Intensity vs wavelength graphs for incident (a) and outgoing (b) light beams.....	47
Figure 35 Spatial irradiance distribution of laser beams at (a) 500 nm (b) 550 nm (c) 600 nm (d) 650 nm wavelengths.	48
Figure 36 Spatial irradiance distribution of laser beams at 450, 500, 550, 600, 650 nm.	49
Figure 37 Wavefront of laser beam.	52
Figure 38 Tolerance data editor in OpticStudio.	53
Figure 39 (a) Set up section and (b) criterion section in tolerancing tab.	54
Figure 40 Monte Carlo section in tolerancing tab.	54
Figure 41 Photographs of the multi-pass matrix optical system in operation in different number of passes configurations. (a) and (b) field mirror group. (c) objective mirror group.....	57
Figure 42 Microscope measurements of multi-pass matrix optics. (a) Left edge of mirror T ₁ , 10x magnification, Stereo microscope. (b) Edge of O ₁ , 10x magnification, Stereo microscope. (c) Top edge of T ₁ , 5x magnification, Nomarski microscope. (d) Middle of T ₁ , 5x magnification, Nomarski microscope. (e) A scratch on O ₁ , 50x magnification, Nomarski microscope. (f) T ₂ , 5x magnification, Nomarski microscope.....	60
Figure 43 Reflectivity vs wavelength graph of protected Silver coating of multi-pass mirror matrix system from 300 nm to 2500 nm spaectral range.	61
Figure 44 The layers and thicknesses given as an example of silver coating [58]..	62

Figure 45 Surface maps of field mirror T ₁ before bonding (a) and after bonding (b).	65
Figure 46 Schematic representation of experimental setup.	68
Figure 47 3D representation of experimental setup.	68
Figure 48 A round trip of ray of light inside the multi-pass matrix optical system.	70
Figure 49 Photograph of the experimental setup of measurement system for trace amounts of molecular absorbers.	73
Figure 50 The normalized absorption vs number of passes graph of crystal violet with the concentration of 10 ⁻⁸ M at 509.5 nm wavelength.	74
Figure 51 The normalized absorption vs number of passes graph of crystal violet with the concentration of 10 ⁻⁸ M at 545.2 nm wavelength.	75
Figure 52 The normalized absorption vs number of passes graph of crystal violet with the concentration of 10 ⁻⁸ M at 592.0 nm wavelength.	75
Figure 53 Normalized absorption vs wavelength graph of crystal violet for different concentrations.	76
Figure 54 Photographs of PP type microplastics inside the cuvette.	78
Figure 55 Normalized extinction vs wavelength graph of PP type microplastics according to different concentrations.	79
Figure 56 Reflective curves for metallic mirror coating [63].	84
Figure 57 48 passes with 6x4 matrix arrangement. In this configuration quartz cuvette filled with water was placed in the optical path between field and objective mirrors.	85
Figure 58 The normalized absorption vs number of passes graph of crystal violet with the concentration of 10 ⁻⁸ M at 509.5 nm (a) at 545.2 nm (b) at 592.0 nm wavelengths.	87
Figure 59 Spectrally averaged absorption vs concentration graph of Crystal Violet.	89
Figure 60 Laser beam passages through cuvette obtained by OpticStudio software.	90

Figure 61 Spectrally averaged extinction vs concentration graph of PP type microplastics.....91

CHAPTER 1

INTRODUCTION

For a ballistic missile defence (BMD) system that utilize an imaging infrared (IIR) seeker, it is of utmost important to define an accurate IR signature model. For an IIR seeker, number of photons detected is the most important aspect to define the detection range. The photons that are radiated by the target are naturally interacting with the atmospheric molecules they are travelling in. Therefore, it is crucial to define the amount of extinction caused by the atmospheric gas components. The extinction characteristics of the molecules is significantly affected by the environmental parameters such as temperature and pressure. These parameters are highly dependent on altitude, resulting a characteristic behaviour of these “trace” gas molecules. As a result, it is vital to measure the transmissivity of trace gases in the high-altitude atmospheric conditions. It is quite hard to perform these experiments at these altitudes. While establishing similar conditions in a laboratory environment is also quite hard to accomplish, it is comparatively easier to achieve. Since these photon movements are almost instantaneous compared to molecules along the path, and the path length is usually in the order of kilometres, the interaction can be modelled with a statistical approach. Thus, depending on the altitude and corresponding trace gas pressure, it is possible to be replicated in 100s of meters. It is still not viable to build a 100s of meters long test environment, yet it is possible to extend the optical path with reflective surfaces to simulate such interaction conditions. Therefore, the need for a reflective optical system in which the light can pass and interact multiple times with the trace gas molecules in the limited testing envelope has emerged. In order to satisfy this, a multi-pass optical system has been designed, built and set up for trace spectroscopic applications. To evaluate the mirror design, extinction spectroscopy studies of crystal violet (CV) as molecular absorber

and polypropylene (PP) as scattering microparticles were carried out in a quartz cuvette placed in the multi-pass beam path between the mirrors of the system in an open atmosphere environment. To analyse the performance of the novel multi-pass measurement technique, the limit of detections (LoD) have been defined. Optical design parameters, ray-trace analysis and post-production test results are also presented.

1.1 Spectral Signature Studies in Defence Applications

1.1.1 Thermal Emission and Blackbody Radiation

The objects are made up of constantly vibrating atoms which create electromagnetic waves. The vibration is observed more often in higher energetic atoms. When the temperature of an object increases, the vibration also rises and hence it causes higher the spectral radiation energy. Therefore, depending on the spectral emissivity (ϵ) and the temperature of the objects, all objects hotter than -273 C° emit radiation according to an intensity and wavelength distribution. This phenomenon is usually defined in terms of blackbody which is an object that absorbs all the incident radiation and radiate them perfectly according to Kirchoff's law [3].

The number of photons that objects emit, also called radiative power, $R(\lambda, T)$ and the wavelength distribution can be defined by Planck's radiation law:

$$R(\lambda, T) = \frac{2\pi hc^2}{\lambda^5 \left[e^{\left(\frac{hc}{\lambda kT}\right)} - 1 \right]} \quad Wcm^{-2}\mu m^{-2} \quad (1)$$

$$P(\lambda, T) = \frac{2\pi c}{\lambda^4 \left[e^{\left(\frac{hc}{\lambda kT}\right)} - 1 \right]} \quad photons\ s^{-1}cm^{-2}\mu m^{-1} \quad (2)$$

where λ is the wavelength, T is the temperature, h is Planck's constant, c is the speed of light, k is the Boltzmann's constant.

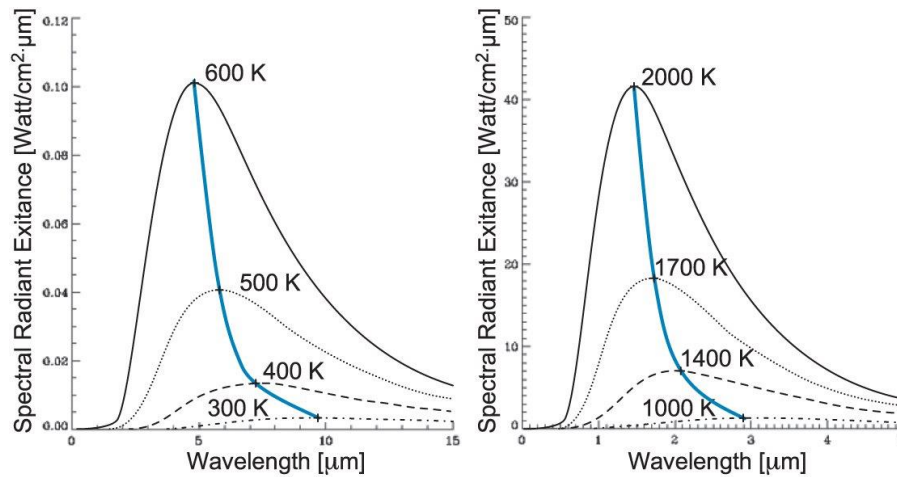


Figure 1 Spectral radiative power of a blackbody $R(\lambda, T)$ vs wavelength, λ at different temperatures [4].

According to Planck's law of radiation, the objects above a certain temperature, radiate in the visible region while at relatively lower temperatures they shift to the infrared part of the spectrum. In Figure 1, the radiation graphs depending on the wavelength of blackbodies at 300 K, 400 K, 500 K, 600 K, 1000 K, 1400 K, 1700 K and 2000 K temperatures are given. According to the graph, a blackbody with a temperature of 300 K radiates the most in the Long Wave Infrared (LWIR) region, a blackbody with a temperature of 600 K radiates the most in the Medium Wave Infrared (MWIR) region, and a blackbody with a temperature greater than 1700 K radiates at wavelengths close to the visible region.

1.1.2 Spectral Signature

Within the scope of engagement modeling studies of missile systems, it is very important to accurately model the space-based infrared signature detection systems or an infrared seeker in a ballistic missile defence (BMD) system analyzed in engagement. The functions of searching/detecting/tracking the ballistic system must be transferred to the model properly. For this reason, the infrared signature information of the model should be known with the same accuracy.

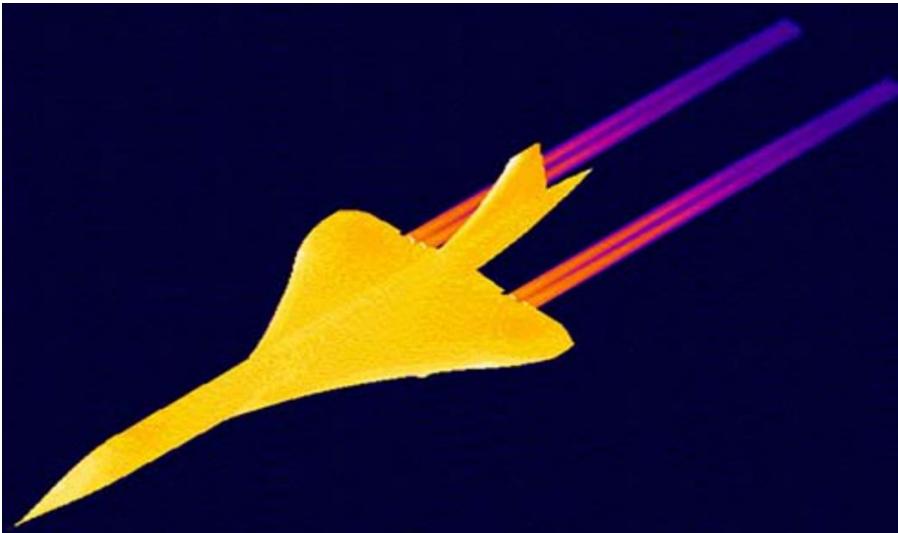


Figure 2 Spectral signature modeling of a target obtained via FEMVIEW IR software [5].

In an infrared signature modeling and calculation study, the outer surface geometry of the system is created in the computer environment. The defined geometric structure is divided into a number of surfaces, namely the nose and bodies. The target reaches different temperatures on each of these surfaces during its trajectory in a given scenario. Surfaces emit blackbody radiation according to their emissivity characteristics, which can be defined as a function of the radiation spectrum, depending on the temperature, type and surface structure of the material. Therefore,

the choice of material directly affects the spectral signature calculations. Moreover, the emissivity varies with surface conditions such as, surface roughness, oxidation etc. Figure 2 shows an example of spectral signature modeling of a target obtained by using FEMVIEW IR [5] which is an infrared signature prediction and analysis software.

The infrared signature also depends on the environment of the target and even on the parameters of the sensor monitoring this system. These factors should also be evaluated in order to reveal the spectral signature correctly and effectively. The radiometric characteristics of a target, especially its infrared signature, which defines its radiation in the infrared region, is very crucial. Since the infrared signature directly affects the detection and lock-in range of the infrared seeker used in countermeasure systems, and hence the performance evaluation.

Among the environmental effects the atmospheric absorption is one of most substantial parameters that affects the number of photons reaching to the detector. Although the density of the atmosphere is very low at the high altitudes especially above 40 km, when the distance between the target and the sensor is too long, most of the radiation emitted is absorbed by trace gasses.

1.1.3 Atmospheric Absorption

Depending on the characteristics of the molecule and temperature, the gas molecules that make up the atmosphere resonate when their natural frequency coincides with the frequency of the radiation they are exposed to. Then, they absorb the radiation coming from the threat, which heats up and makes blackbody radiation according to its emissivity characteristics, at a certain rate.

Absorption of radiation caused by atmospheric gas molecules results in losses in the signal coming to the detector during the signature measurements. Among the gas molecules that make up the atmosphere; ozone, water vapor, carbon dioxide,

methane, nitrous oxide, carbon monoxide gases are the most important molecules that cause absorption, especially in the infrared spectral band range [6].

In Figure 3, the mixing ratios of the gas molecules forming the atmosphere between 0-80 km altitude are given. It is observed that the mixing ratios of gases, which absorb especially in infrared spectral bands, vary significantly with altitude.

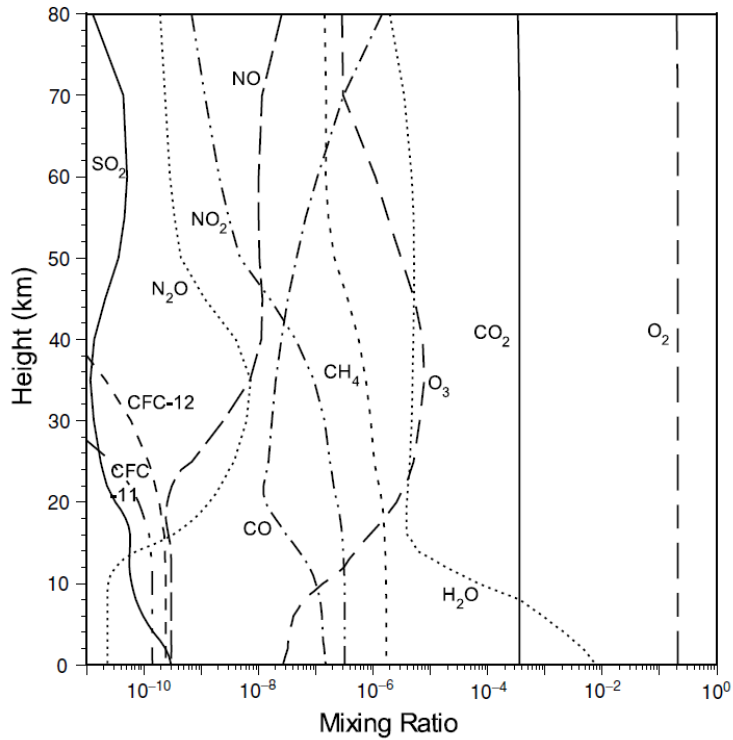


Figure 3 The vertical profile of the mixing ratio of the atmospheric components according to the US Standard Model of Atmosphere [6].

Since atmospheric absorption is directly related with the gas density, the amount of absorption changes as the gas density changes. This phenomenon can be explained by the Beer-Lambert law whose formula is given below:

$$A = \epsilon cl = -\log\left(\frac{I}{I_0}\right) \quad (3)$$

where A is the absorption, ε is the molar absorptance of the gasses, c is the gas concentration, l is the optical path that light travels, I_0 is the intensity of incident light, I is the intensity of the light passing through the atmosphere.

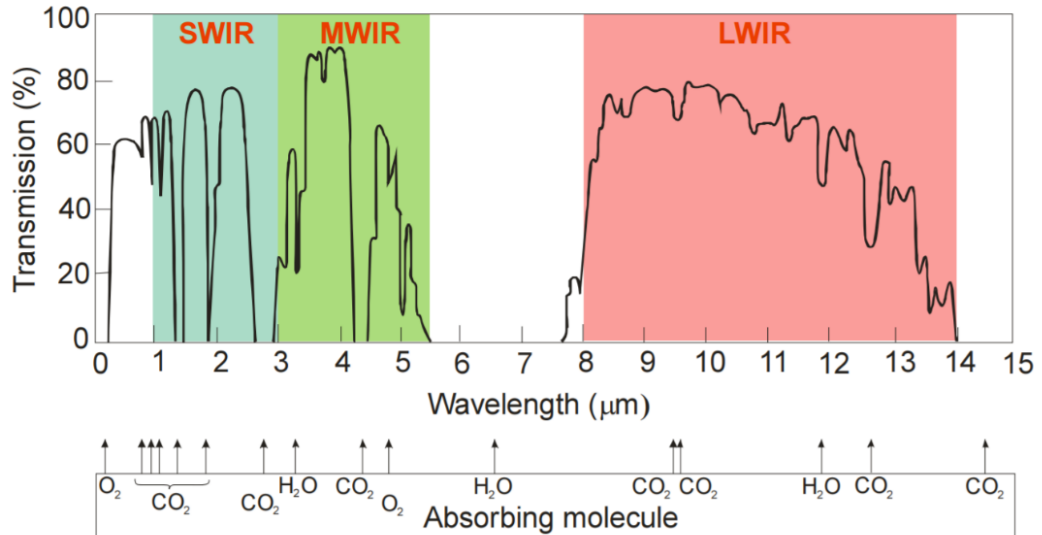


Figure 4 Atmospheric transmission for 1.8 km horizontal path at sea level [3].

The Figure 4 illustrates the transmission of the atmosphere through 1.8 km of air path with respect to wavelength at sea level where the atmosphere has greater concentration compared to higher levels. Due to the absorption bands of the major molecules such as ozone, carbon dioxide, water, the atmospheric windows are restricted between 3-5 μm and 8-14 μm at the sea level. Compared to the major molecules mentioned; nitrous oxide, carbon monoxide, methane etc. become negligible absorbing components in the atmosphere. However, if the optical path is too long, even weak lines of trace gasses would play an urgent role in the spectroscopic calculations. Therefore, those molecules should also be taken account during the spectral signature measurements and theoretical calculations.

1.1.4 Spectral Modelling of Atmospheric Effects

PcModWin MODTRAN [7] is an open source software that is used to model spectral transmission of the atmosphere in several user-defined configurations. The software uses 1976 US Standard Atmospheric Model [8] for physical and chemical parameters of the atmosphere and HITRAN [9] database which is a collection of spectroscopic parameters used by various computer codes to predict and simulate the transmission and propagation of light in the atmosphere. The HITRAN database is a long-running project initiated by the Air Force Cambridge Research Laboratories in the late 1960s in response to the need for detailed information on the infrared properties of the atmosphere. Some of the parameters available in HITRAN are calculated and some are obtained from the analysis and fit results of spectroscopic laboratory experiments [9].

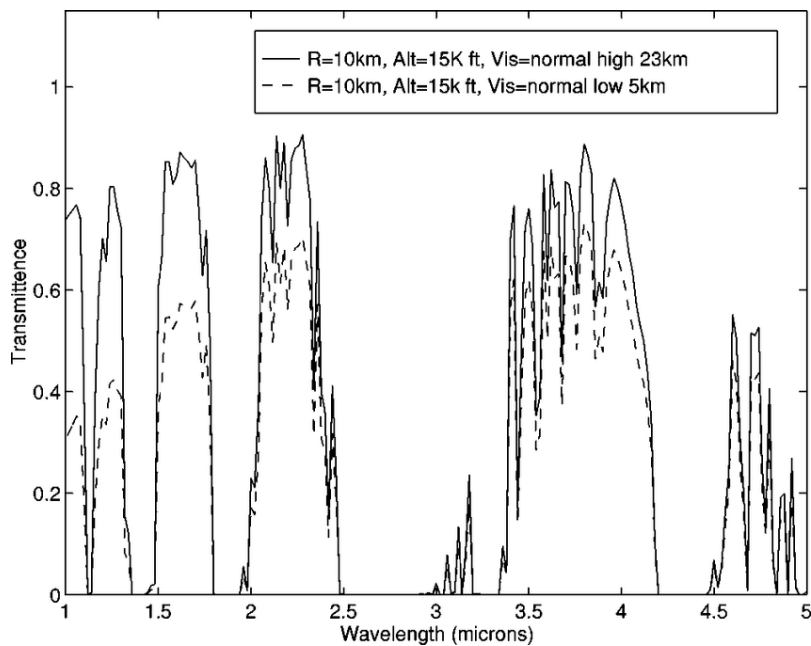


Figure 5 Atmospheric transmission graph in the spectral range of 1-5 μm at 23 km and 5 km altitude [10].

In Figure 5, the transmission graph of the atmosphere at 5 km and 23 km altitude is given by using MODTRAN software. Atmospheric composition has a dynamic structure that changes not only depending on altitude, but also depending on

geography and time [11, 12]. Therefore, since the gases in the atmosphere have different concentrations in different geographies, years and seasons; the amount of absorption will also be different.

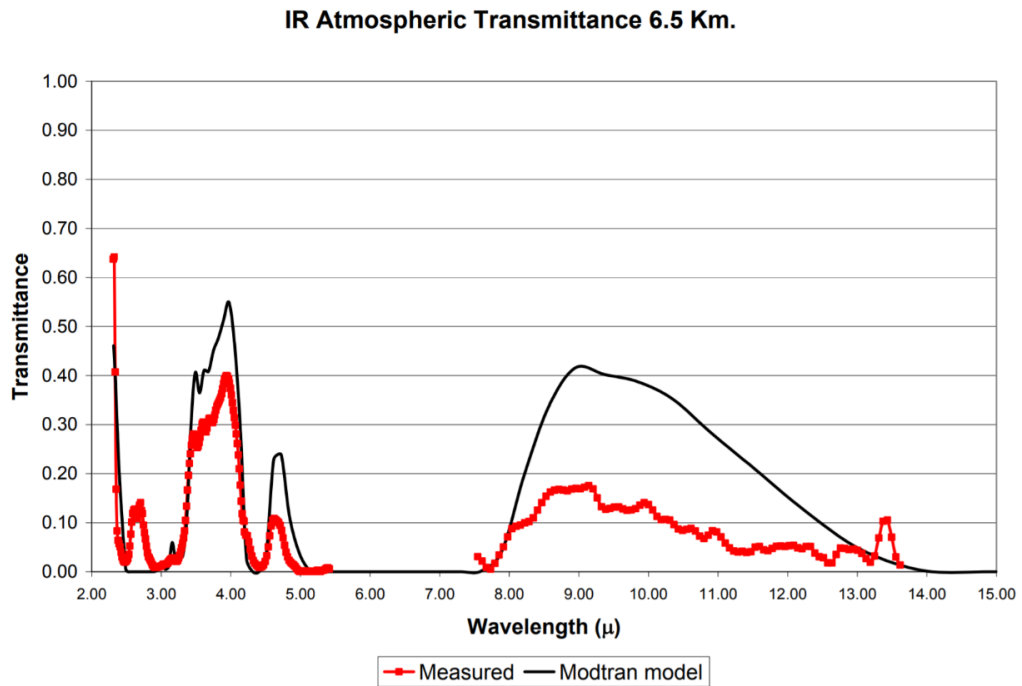


Figure 6 Atmospheric transmission as measured with a spectroradiometer at 6.5 km distance between the spectral range 2 and 14 μm [13].

As the software calculates with statistical characterization method using average atmospheric values in the spectral band range, it causes errors. The software, which does not have geographical specialization other than six atmospheric gas composition models which are Tropical, Mid-latitude summer, Mid-latitude winter, Sub-polar latitudes summer, Sub-polar latitudes winter, has not been validated in the literature for thin atmospheric conditions at high altitudes. Hence, the reliability of the software in different regions and different atmospheric conditions is discussed [13]. Figure 6 shows the difference between the measured spectral atmospheric transmission with a spectroradiometer and modeled one by using MODTRAN software at 6.5 km distance, between the spectral range 2 and 14 μm .

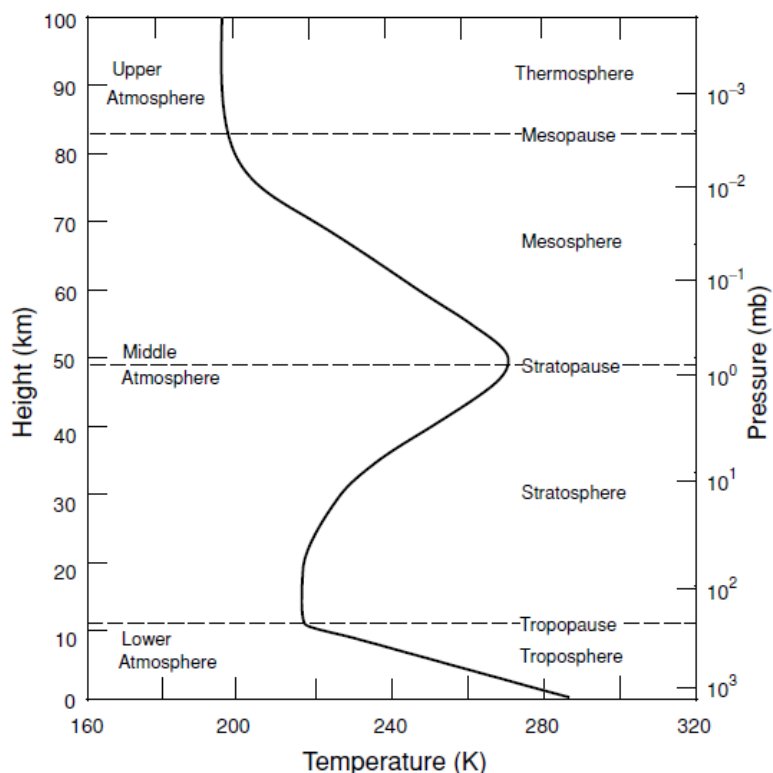


Figure 7 The vertical temperature profile of the atmosphere between 0-100 km altitude according to US Standard Model of Atmosphere [6].

Since the vertical temperature profile of the atmosphere has a very variable structure, it causes the spectral radiation of gas molecules at each altitude to be of different intensities and to shift their spectrum. In Figure 7, the vertical temperature profile between 0-100 km altitude of the atmosphere is given. According to the graph, the temperature values vary between approximately 200 K and 290 K within the specified altitude range.

In the HITRAN database, spectral radiation values specific to atmospheric gas molecules are given according to the constant temperature which is 296 K. MODTRAN software calculates the spectral radiance values at different temperatures by using the radiance value corresponding to the 296 K temperature obtained from HITRAN. Spectral information at different temperature values of the

atmosphere is theoretically obtained between 70-3000 K temperature values. In the literature, the reliability of the HITRAN database in sensitive applications is discussed due to the variability between different published versions [14,15].

Atmospheric spectroscopy experiments were needed to meet the need to accurately reveal the infrared signature of the threat, due to the low reliability of the software and models used. In line with this requirement, it is aimed to make the measurements with the atmospheric environment created under laboratory conditions.

Data sets will be obtained within the scope of high-altitude infrared trace modeling studies by supplying and operating the equipment required for these studies, which will be carried out in laboratory conditions. It is considered that together with the hardware to be installed, the theoretical knowledge to be gained with these data sets and the models to be created will form an important infrastructure in high altitude and space-based projects in the long run.

1.1.5 Atmospheric Trace Gas Measurement System

In order to model the effects of the atmosphere, a sealed vacuum-capable chamber is designed and planning to be built. Atmospheric Trace Gas Measurement System illustrated in Figure 8, is a cylindrical stainless-steel chamber whose effective volume is approximately $300 \times 230 \times 920 \text{ mm}^3$. The chamber will be thermally adjustable between $-100 \text{ }^\circ\text{C}$ and $+100 \text{ }^\circ\text{C}$ and pressure can be varied from 10^{-3} mbar to 1.5 bar . One of the purposes of the system is to realize trace gas absorption spectroscopy experiments for several atmospheric configurations. Therefore, the atmospheric trace gasses which are active especially in the infrared spectral region can be released to the simulation chamber in a controlled manner. By this way, synthetic atmosphere will be created by controlling the temperature, gas content and pressure as realistic as possible in the chamber. The synthetic atmosphere inside the chamber will be used as a medium to measure atmospheric transmission for several conditions.

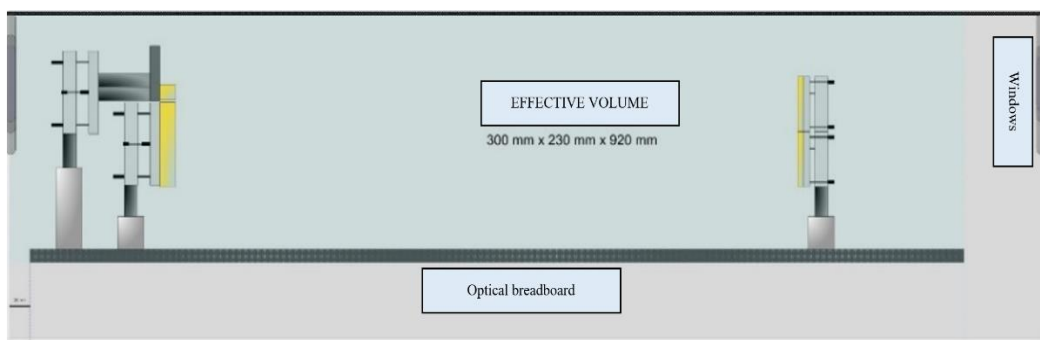


Figure 8 Schematic representation of atmospheric trace gas measurement system.

Atmospheric simulation system will be coupled with tunable laser absorption spectroscopy equipment given in the table below:

Table 1 The Tunable Laser Absorption Spectroscopy (TLAS) equipment coupled to the trace gas measurement system

<i>Equipment</i>	<i>Model</i>
Optical Parametric Oscillator (OPO) / 2-12 μ m	NT242 Ekspla
Optical Parametric Oscillator (OPO) / 200-2400 nm	NT277 Ekspla
Supercontinuum laser	SuperK Compact NKT
Wavelength selector	NKT
Lock-in amplifier 600 MHz	Zurich Instruments
Spectrometer VIS	Ocean Optics
Spectrometer NIR	Arcoptix
Spectrometer MWIR	Arcoptix
Photodetectors	Thorlabs
Translation optics and optomechanics	Thorlabs / Edmund
View ports	Knight Optical
Multi-pass Matrix Optical System	My design

As the density of atmospheric gasses dramatically decreases with high altitudes, to detect especially the weak lines would be challenging with the direct spectroscopy.

Therefore, the need arises to extend the optical path to absorb more molecules of the radiation in order to increase the measurement sensitivity. The optical system that would be located to the trace gas measurement setup is illustrated in the Figure 8.

1.2 Molecular Absorbant Spectroscopy (Crystal Violet)

In this thesis, crystal violet was used to demonstrate the spectroscopic measurements of molecular absorbers. The absorption band of crystal violet is well-known and its spectroscopic studies are frequently encountered in the literature. Crystal violet dye shows high absorption characteristics due to strong pigmentation. Since the cuvette used in the performance studies has large volume, it is necessary to use a large amount of absorber molecules. Moreover, as crystal violet is an easy-to-find material, it is suitable for use in large quantities. Solution preparation is inexpensive and easy as it is soluble in water. In addition, it is important to develop sensitive and reliable detection methods and produce new solutions due to the damage to nature.

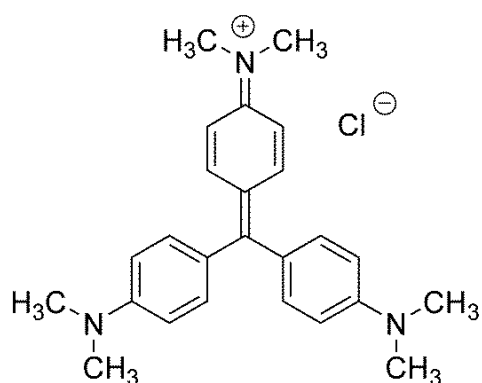


Figure 9 The chemical structure of crystal violet [16].

Due to lack of natural resources, the fishery productions are supplied via aquaculture production which results in an increase in waste materials and organic compounds in fishponds and hence a dramatically increased risk of fish diseases [17]. Since the crystal violet (CV) is one of the banned drugs in aquaculture, this has become an issue of concern for consumers and regulators. CV (Figure 9) which is used as

antifungal drug is a purple cationic triphenylmethane dye [18]. The residues of CV in foods lead to potential health risks such as cancer by reason of prolonged exposure. For this reason, the use of CV in aquaculture has been prohibited by many countries such as USA, Japan, China and European Union [19]. Therefore, it is urgent to develop simple, reliable and sensitive methods for the determination of trace amount of CV in aqueous solution. To date, there has been several methods developed to detect CV such as surface enhanced Raman scattering (SERS), chromatography, electrophoresis, fluorescence, mass spectrometry, spectrophotometry, electrochemiluminescence, high performance liquid chromatography (HPLC) etc. The limit of detections (LOD) and the related methods applied to detect trace amount of CV are given in the Table 2.

Table 2 Limit of Detection of CV measurements and methods.

<i>Source</i>	<i>Limit of detection (LoD)</i>	<i>Method</i>
Y. Han <i>et. al.</i> , 2018 [20]	6.1×10^{-8} mol/L	Fluorescence
Q. Lan <i>et. al.</i> , 2018 [21]	3.2×10^{-9} mol/L	Electrochemiluminescence
G. Shi <i>et. al.</i> , 2018 [22]	5×10^{-10} mol/L	SERS
Z. Zhou <i>et. al.</i> , 2018 [23]	1.96×10^{-10} mol/L	Mass spectrometry
S. Sadeghi, <i>et. al.</i> , 2018 [24]	3.4×10^{-9} mol/L	Spectrophotometry
X. Yan, <i>et. al.</i> , 2019 [25]	10^{-10} mol/L	SERS
Y. Hu and Z. Gao, 2020 [26]	7.3×10^{-9} mol/L	Fluorescence
G. Yang <i>et. al.</i> , 2020 [27]	8.1×10^{-8} mol/L	SERS
X. Wu <i>et. al.</i> , 2020 [28]	9.8×10^{-11} mol/L	Solid-phase extraction
K. Wang <i>et. al.</i> , 2020 [29]	7.24×10^{-10} mol/L	SERS
Y. Miao <i>et. al.</i> , 2021 [30]	10^{-12} mol/L	SERS
Wen-Xian <i>et. al.</i> [31]	10^{-10} mol/L	SERS

1.3 Scattering Microparticles Spectroscopy (Microplastics)

Today, plastics are widely used in industry due to their low cost, light weight and durability [32]. However, as a result of its erosion over time, it causes water pollution and endanger the health of species in the aquatic environment [33]. Primary micro-sized plastic particles used in many industrial products, including cosmetics and toothpastes, reduce the quality of the water and endangering biodiversity [34]. Therefore, it is of paramount importance to develop techniques for the in-situ detection of microplastics in natural water bodies and water treatment systems. Due to their small size and low concentration, microplastics are difficult to detect in the aquatic environment. To date for detection of microplastics in aquatic environment, there has been proposed many methods, including visual, chemical and optical. Techniques such as Surface Enhanced Raman Spectroscopy (SERS) [35]. Laser-based photoluminescence [36], integrated holography and Raman spectroscopy [37] are used for the detection of microplastics. However, new measurement systems need to be developed since the techniques are laborious, time-consuming, complex and costly. In this work, it is aimed to measure the detection of microplastics in liquid environment with multi-pass matrix optical system.

1.4 Multi-pass Mirror Designs

1.4.1 White Cell Design

The White Cell [38] which was intended to measure the vapor phase spectra of material with high boiling points by enhancing the optical path length were designed by John U. White in 1942 for the first time. The White Cell is made up of three concave spherical mirrors that all have exactly same radii of curvature R . A single field mirror is placed at one end and two adjacent objective mirrors at the other end at a distance equal to their radius of curvature. While the center of curvature of the field mirror is aligned halfway between the two adjacent objective mirrors, in order

to obtain a confocal resonator, the centers of the objective mirrors are slightly misaligned. Therefore, the light coming from the source is refocused onto the field mirror until it leaves from the mirror as shown in the Figure 10. The working principle of the White cell named as White rule [39] states that the position of the successive objective and image position, near the curvature center of spherical mirror, lie on a straight line whose midpoint falls on the center of curvature of the last objective mirror.

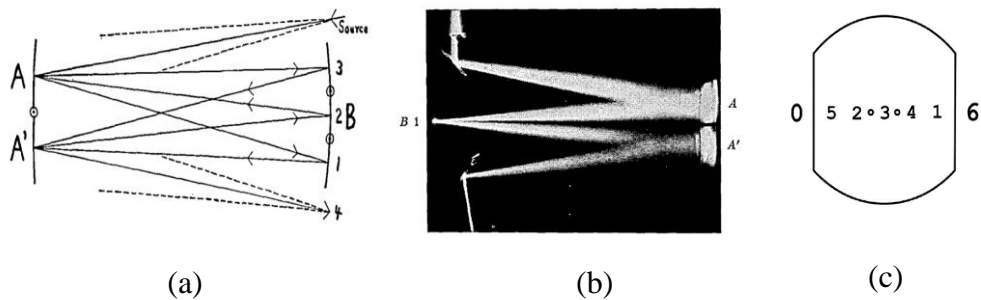


Figure 10 (a) White cell design. (b) Photograph of White cell. (c) Images on the field mirror.

Bernstein and Herzberg [40] slightly modified the White cell by using a T shaped mirror to investigate the spectrum of fluoroform under high resolution. The geometry of the field mirror given in Figure 11 provides a doubling the optical path with two rows of light beam on the field mirror.

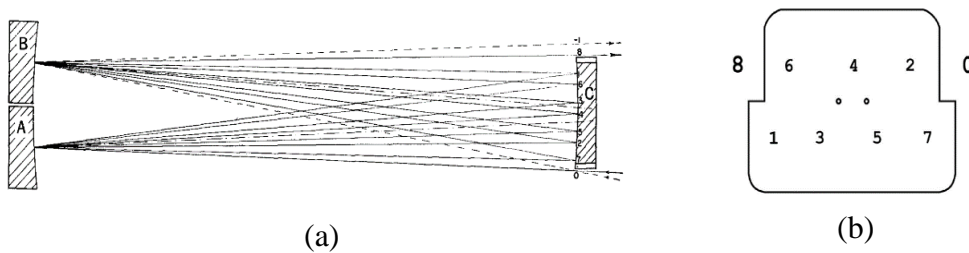


Figure 11 (a) Bernstein and Herzberg's multi-pass mirror design. (b) Images on the field mirror.

Similarly, in order to measure water vapor continuum coefficients, Tobin *et. al.* [41] designed a multi-pass mirror system with two rows of light beam on a rectangular field mirror as shown in Figure 12.

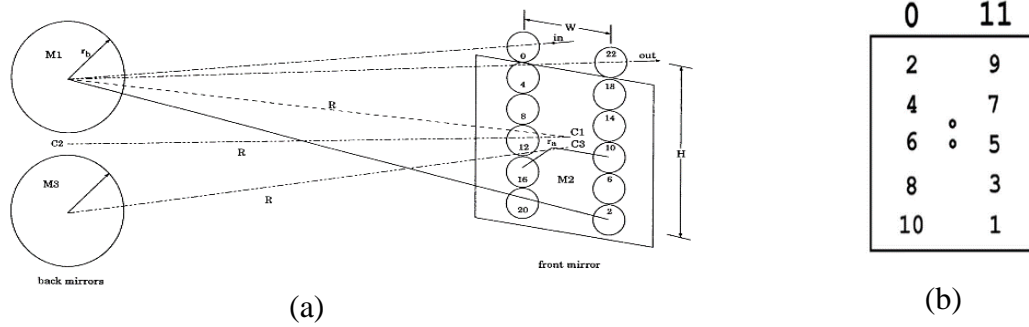


Figure 12 (a) Tobin *et. al.* multi-pass mirror design. (b) Images on the field mirror.

Although, the designs of both Bernstein *et. al.* and Tobin are almost similar with the currently introduced ones, they suffer from basically three limitations. First of all, with this arrangement, only two rows of images can be produced on the field mirror. Thus, doubling the number of light beams on the field mirror requires twice the width of the field mirror. When the width of the field mirror increases to obtain large number of passes, it would only be possible by using high reflective coatings on a huge area which causes extreme material cost, more rugged mechanical mounts, heavier field mirror [42].

Secondly, astigmatic image broadening is a common concern as image aberrations for Bernstein and Herzberg modified White cells. According to the small angle approximation, the radius of curvature of the spherical mirror and the square of the incident light ray angle are directly related with astigmatism aberration. When the number of passages increases, images are formed further away from the axis which causes astigmatic image broadening. Consequently, only a small amount of light passing from the cell is able to reach to the detector.

Thirdly, the limitation on the vibrostability was also a common issue that all the designers tried to overcome. Due to the fact that the vibrostability of the alignment of the objective mirrors is directly related with the number of columns on the field mirror, matrix form is much more preferable rather than two row orientation.

1.4.2 Modified White Cell Designs

Due to the limitation of the design of Bernstein and Herzberg's multi-pass mirror systems, several modified designs have been introduced. By splitting the field mirror into four parts and adding two objective mirrors to the system, Hanst produced a matrix of light beam on the field mirror group as shown in the Figure 13. The design was used in Shetter *et. al.*'s [43] evacuable thermal chamber for atmospheric gas absorption studies.

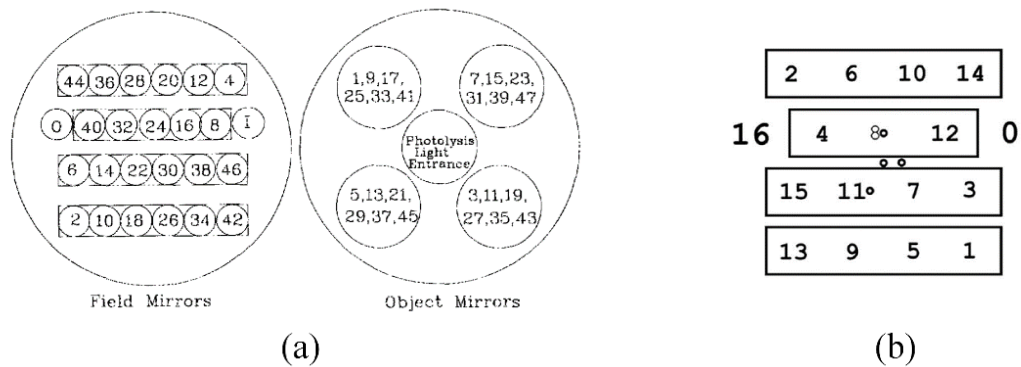


Figure 13 (a) Hanst's multi-pass matrix design. (b) Images on the field mirror group.

To obtain matrix form on the mirror, Horn and Pimentel [44] separated the field mirror group to several pieces similar to Hanst's design shown in Figure 14.

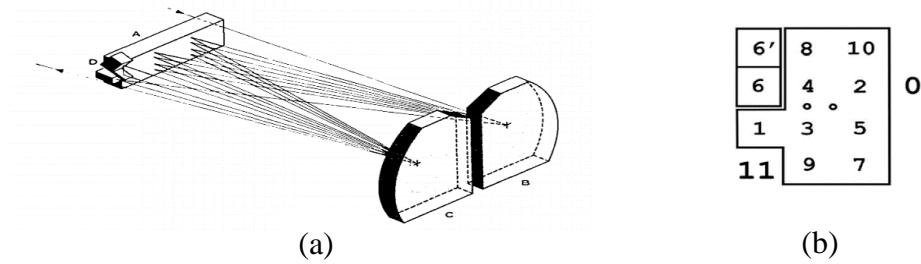


Figure 14 (a) Horn and Pimentel's multi-pass matrix design. (b) Number of images on the field mirror group.

Herriott and Schulte [45] proposed a multi-pass mirror system consists of two spherical mirrors placed opposite each other so that the distance between them is equal to the radius of curvature. One of the mirrors has a hole in its center through which incident light beam can enter in an off-axis direction. The light circulates between the mirrors inside the cell until it leaves from the hole through which entered the system. Thus, the system acts as an off-axis resonator shown in Figure 15. The number of pass is determined by the angle of incident light beam. However, the design requires extreme precision in construction which makes it financially unsuitable. Moreover, the Herriott design is ineffective for incoherent broadband light sources because of lack of focal properties [42].

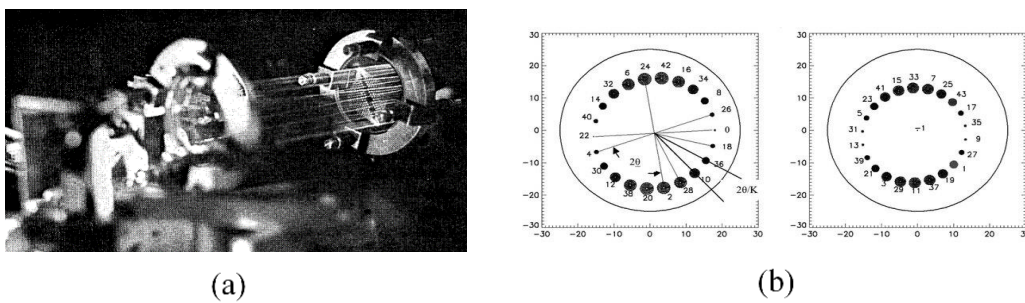


Figure 15 (a) Photograph of Herriott cell. (b) Images on mirrors of Herriott cell.

To achieve accurate spectroscopic measurements, optical path and noise are vital factors which affect the intensity of the light beam and signal respectively. If

misalignments and vibrations increase with increasing optical path length, the system would be ineffective. Therefore, some designers have proposed stabilized systems to come through the limits [46].

To reduce the loss of alignment caused by the fluctuation of refractive index and vibration, White [47] proposed a new design by adding two pairs of retroreflectors to his original one. For UV spectrometry applications, Ritz *et. al.* [48] further developed the new design of White by adding three right angle prisms to increase the vibro-stability. Doussin *et. al.* developed the design and customize the system to perform infrared spectroscopic studies in an atmospheric simulation chamber shown in Figure 16.

Despite the modifications introduced in this section bring better stability to misalignments and vibrations, Grassi and Guzzi [39] proposed a theoretical ray tracing study that shows modified White cells with retroreflectors and prisms leads to extreme negative effects on optical throughput which is hard to predict without detailed ray trace analysis. They state that when flat surfaces such as prisms or retroreflectors are used inside the system, due to beam divergence caused by the surfaces, the symmetry of the White cell (White rule) is broken.

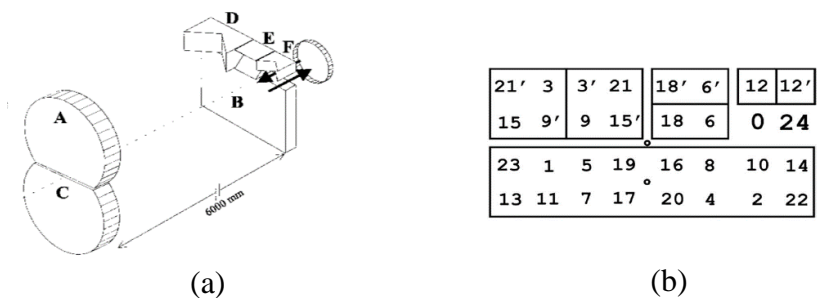


Figure 16 (a) Doussin *et. al.*'s multi-pass matrix system. (b) Images on field mirror group.

The modified White cells which are made up of plenty of mirrors, prisms, retroreflectors, mirror mounts, lenses etc., may not be practicable due to complex

alignment and probable vibration issues. Also, in some of the modified cells, the input aperture is adjacent to or overlaps the output aperture, making it difficult to separate the input and output light and to align the detector and source.

1.4.3 Chernin Cell Design

Compared to the modified and complicated designs mentioned in the previous section, Chernin published a group of papers that included designs which are simpler and easier to align. The designs named as Soviet matrix multi-pass systems introduce less aberrations, and higher vibration stability.

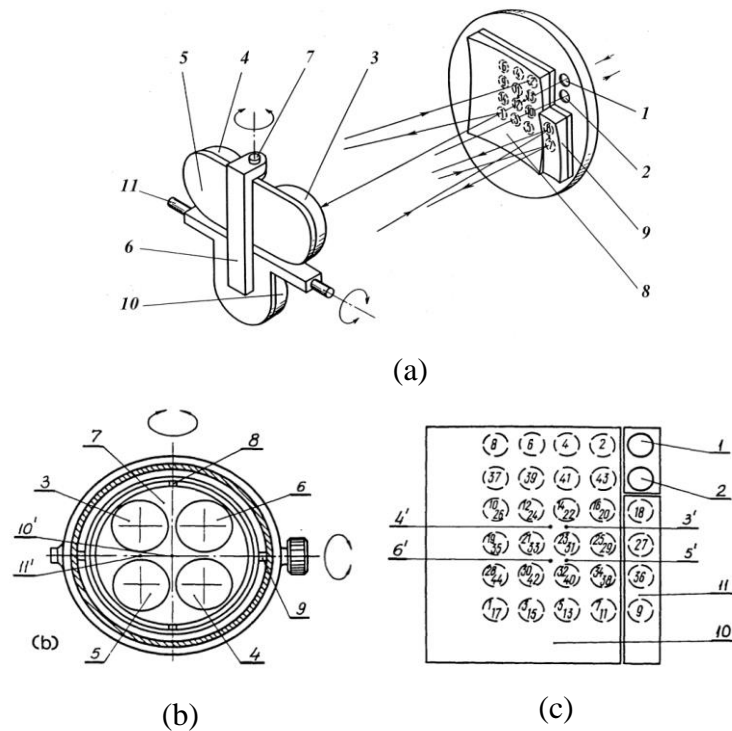


Figure 17 (a) Chernin's multi-pass matrix three objective system. 1-entrance aperture, 2-exit aperture, 3,4,10-objective mirrors, 5-turning plate, 6-holder, 7-vertical axis, 8,9-Field mirrors, 11-horizontal axis. (b) Objective mirror group. 3,4,5,6- objective mirrors, 7-mirror holder, 8-vertical axis, 9-horizontal axis, 10'-11'- curvature centers of field mirrors. (c) Field mirror group. 1-entrance aperture, 2-exit aperture, 3'-6'-curvature centers of objective mirrors, 10,11-field mirrors [1].

Figure 17 illustrates three and four objective mirror multi-pass matrix system designs of Chernin and Barskaya. In three objective mirror system, first two rows of images are formed by paired objective mirrors 3 and 5 as illustrated in Figure 17(a). Then field mirror 8 reflects the light beam onto objective mirror 10 that sends the light beam back to the same field mirror. Then the light beam again reflects to the objective mirror 3 which is the first mirror met the incoming light. Therefore, it opens a new entrance with a different angle to obtain a matrix form. In each cycle a matrix with 2 rows are formed, until the light beam exists the system.

Although three objective multi-pass design of Chernin is promising, being adjacent of input and output apertures makes the separation of incident and outgoing light beams and alignment of light source and detector inconvenient. Therefore, in 2001-2002 Chernin modified his design that includes three or four objective mirrors and a field mirror through which light beam can enter from two opposite ends shown in Figure 18. When the system is used with an instrument having large angular beam divergence such as diode lasers, the design has become much more accurate with this arrangement.

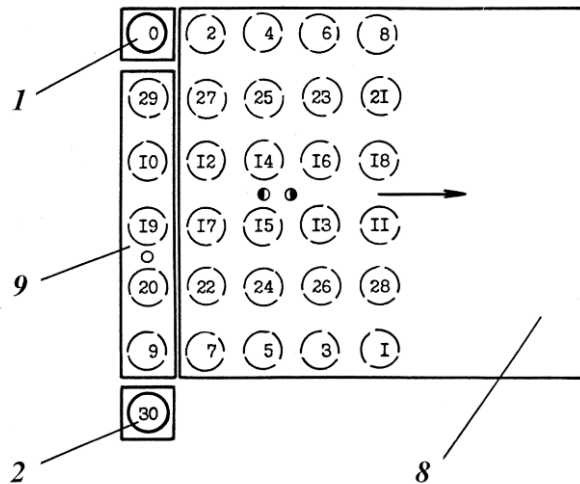


Figure 18 Chernin's modified three objective multi-pass matrix system. 1-entrance aperture, 2-exit aperture, 8,9-field mirrors.

CHAPTER 2

THE OPTICAL SYSTEM

In this section, the design, production and post-production optical characterization processes of the multi-pass matrix optical system are explained in detail. The general features of the selected model and why this model is more advantageous than other models for atmospheric trace gas measurement studies are discussed, and the general features and working principle of the model are explained. In the design, design parameters such as optimum number of passes, mirror sizes, laser beam diameter, divergence of the laser, wavelength to be used, and resolution, which are among the design criteria aimed at extending the optical path, are discussed. After the parameters were determined, a ray trace simulation of the optical system was created with Zemax OpticStudio software. The position and angle parameters of the mirrors were selected as variable and the optimum values were determined according to the RMS radius and centroid of the system. As a result of the simulation, optical aberrations were detected and the performance of the system was evaluated by assigning tolerance values. The optics were produced with the parameters obtained as a result of the simulation. Finally, surface characterizations of the optics such as irregularity and roughness were measured with a test plate and the reflectivity value of the coating was measured with a spectrophotometer. The defects formed on the coating over time were detected with Nomarski and Stereo microscopes.

2.1 Optimum Cell Design Criteria

Contrast to other type of cell designs, Chernin cell is much more uncomplicated, easy to align, vibrationally stable, astigmatic free and also it obeys the White rule mentioned in the previous chapter. A Chernin based three objective multi-pass cell as already been installed to an atmospheric simulation chamber which is used for

photochemical smog measurements constructed at the University of Leeds in UK and it performed good results [42].

Steyert *et. al.* [49] published a paper describing the analysis of Chernin's three objective multi-pass matrix optical system for tunable laser spectroscopy. They stated that, the Chernin type cell is extremely stable at harsh environmental conditions for planetary atmospheric applications. They state that the cell can be successfully used both at low and positive atmospheric pressures, also at the temperatures above -148 °C. The atmospheric absorption experiments will be done for high-altitude environmental conditions in a simulation chamber in some cases which require extremely low pressure and temperature. Since Steyert and Glowacki stated that the system works stably under these conditions, the Chernin type cell becomes more suitable contrast to other type of cells.

As the absorption is very low at high altitudes, the number of passes should be high enough to increase the optical path length and hence the sensitivity of the system. For some applications, the optical multi-pass system will not only be used to increase the sensitivity of the system but also to obtain the real path length between our detector and the target to be measured. Therefore, the number of transitions between the mirrors should be adjustable easily and very high if necessary, as provided by the Chernin type cells.

Despite the fact that, the original White cell designs require more basic optomechanics for the mirrors, the stated reasons make Chernin type cells quite more prominent.

2.2 Design of the Optical System

In my design, the multi-pass matrix system which is made up of three objective (O_1 , O_2 , O_3) and two field mirrors (T_1 , T_2), is constructed for at least 72 passages provided by 6x6 matrix arrangement on the field mirror group. The mirrors which are all spherical concave and have the radius of curvature exactly the same are located

opposite each other so that the same mirror groups are together. The distance between the objective and field mirror groups that determine the optical path length is placed so that it is equal to the radius of curvature. Since the focal point (f) of a spherical concave mirror is the half of the center of curvature, all the mirrors are located at $2f$ distance to each other.

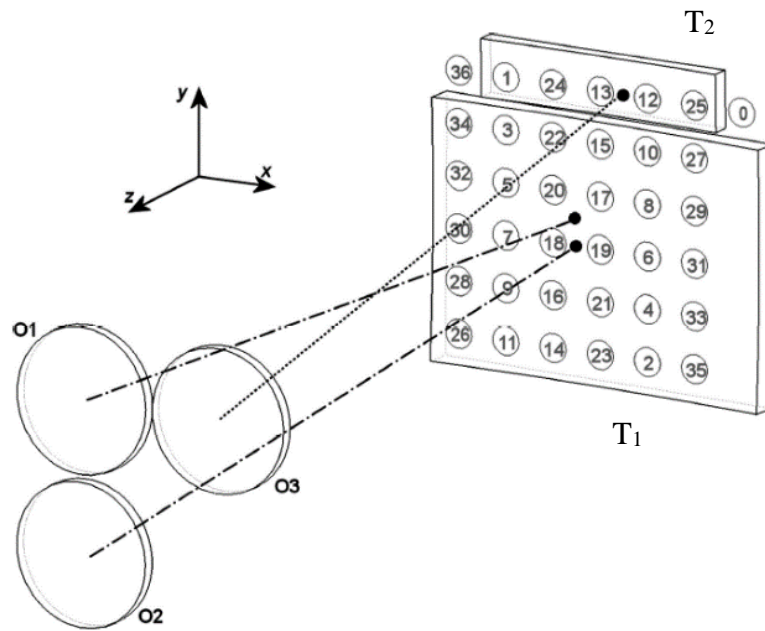


Figure 19 Three objective multi-pass matrix system scheme.

As shown in the Figure 19 the images of the light beams are seen on the field mirrors, T_1 and T_2 . The width of the field mirror T_2 is smaller than T_1 to avoid blocking the entrance and outgoing apertures. In contrast to the final Chernin design, T_2 is located above T_1 in order to get the outgoing light beam that reflects from the last mirror at the same height with the incoming one. While the center of curvature of T_1 is located between the objective mirrors O_1 and O_2 at the intersection point, the center of curvature of T_2 is located between O_1 and O_3 at the intersection point.

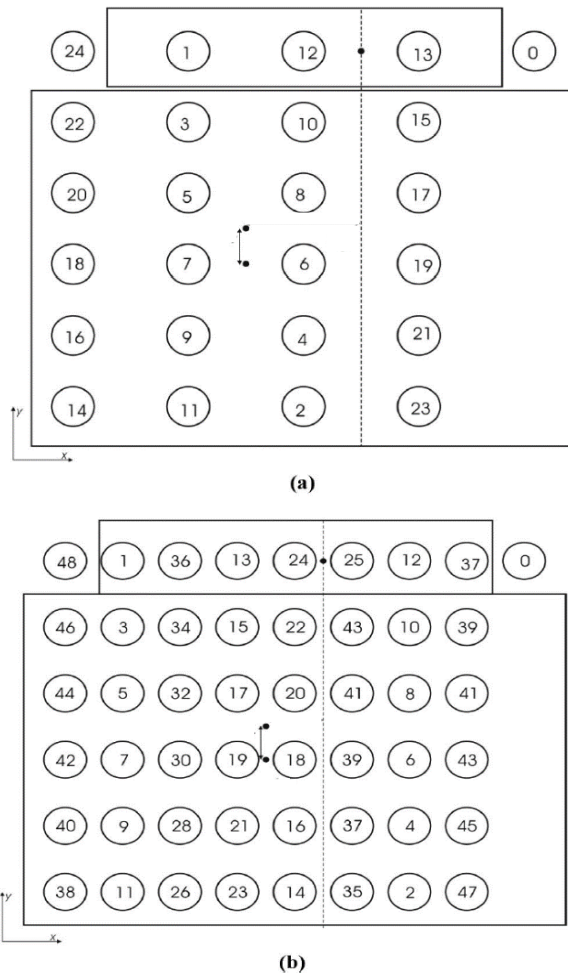


Figure 20 Images of the field mirror T_1 and T_2 .

The center of O_3 that is the mirror that light meets first is located perpendicular to the incident ray of light contrast to original design of Chernin. Since the objective mirror O_3 is tilted about the vertical axis, the center is placed midway between the position of the incident light and the position of the first image on the field mirror T_2 . Then the light is reflected from the surface of T_2 to O_1 due to the fact that the center of curvature of T_2 is placed between the mirrors O_1 and O_3 . The reflected light from surface O_1 is projected to the surface of T_1 at the desired point which is shown in Figure 20 as 2, since the center of curvature of O_1 is located between so that the location of second image is symmetrically located to the location of first image. Then

the light beam reflecting from the surface of T_1 to O_2 is reflected to T_1 again with the same logic. Until the image 12, the light is reflected between O_2 , T_1 and O_1 in a cycle. After the reflection of 12th image to the surface of the objective mirror O_3 , the first two columns of image on the field mirrors are completed. Therefore, the cycle is again started from a new entrance aperture with a different angle. Until 36th image that is the last beam of light leaves from the output aperture of the system, the reflection cycles repeat one another. Therefore, within the multi-pass system 72 passes are obtained.

If the distance between the center of curvature of O_2 and the center of curvature O_1 are kept the same while travelling up or down together, the number of rows on field mirrors does not change. This property can be used to fix the objective mirrors O_2 and O_1 in order to increase the vibrostability. On the contrary, if the distance of them are not kept the same while shifting up or down, the number of rows can be enhanced by getting closer the center of curvature of the objective mirrors. In that case the mirrors should be controlled independently during the alignment. In my design the number of rows is easily adjustable and only depends on the beam diameter on the field mirror.

In the design, since the working principle of the system is White Rule, the number of columns is restricted with even numbers because of the symmetry. In order to increase the number of columns on the field mirrors, there are two ways to apply. The first way is to keep the center of curvature of O_2 and O_1 together and locate the center of curvature of O_3 closer to that of O_2 and O_1 in the horizontal axis. In this case, the first image on T_2 should be as close as possible to the left corner of the mirror. While this arrangement leads to increasing the number of images, it also causes the location of the output aperture to shift. This is the way that Chernin [50] suggested to keep vibrostability while increasing the number of columns.

The second way which provides more images compared to first way is that, the center of curvature of O_1 and O_2 should be located closer to the input aperture and the center of curvature of O_3 is getting closer to the output aperture which means that the

distance between the center of curvatures of the mirrors should be as small as possible as shown in the Figure 20. The second case shows weaker vibrostability than the first one, but the latter allows the system to keep the position of the output beam at exactly the same point as the number of columns increases. This ensures that the positions of the equipment outside the cabinet such as transfer optics, detector etc. remain the same for each configuration.

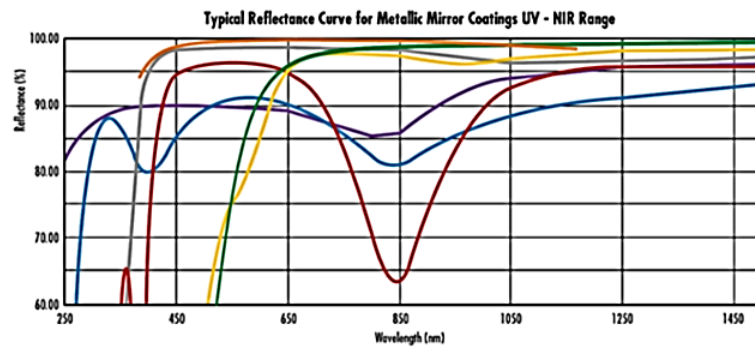
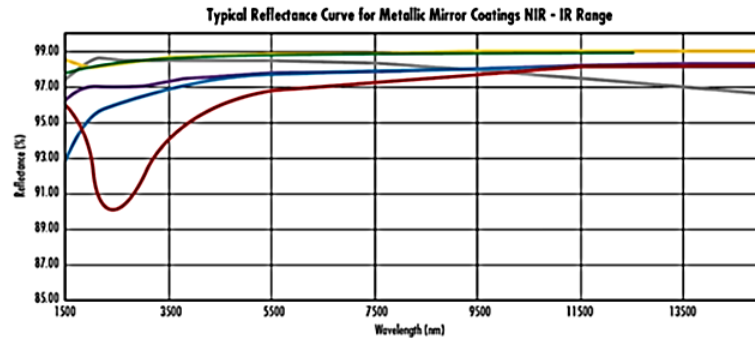
All mirrors have their mechanical mountings that provide them to rotate in three dimensions. The reason why all mirrors should rotate independently is that different number of passes configurations require the mirrors to rotate in different angles. The number of passes can be adjusted by two degrees of freedom for all mirrors except for O_3 that needs only tilt screws. Although only the screws that enable pan and tilt to the mirrors are sufficient for the design, if the optics are not manufactured with desired precision, the extra degrees of freedoms would be vital for alignment.

2.2.1 Definition of Optical Design Parameters

2.2.1.1 Number of Passes

The number of passes between the objective mirror and field mirror groups is obviously related with the matrix orientation. The number of columns and rows depend on the reflectivity of the coating on the optics. Therefore, the coating with the highest reflectivity should be selected according to the wavelength range to be studied. Since the current design was produced for mid-infrared atmospheric spectroscopic studies, the material of the coating was selected as protected silver whose reflectivity between 2-10 μm is greater than 98%.

Figure 21 gives typical reflectance curves for metallic mirror coatings from near-infrared to mid-infrared region.



Protected Aluminum	Enhanced Aluminum	UV Enhanced Aluminum	Protected Gold	Bare Gold	Protected Silver	Ultrafast Enhanced Silver
Range (µm) % Reflection	Range (µm) % Reflection	Range (µm) % Reflection	Range (µm) % Reflection	Range (µm) % Reflection	Range (µm) % Reflection	Range (µm) % Reflection
0.4 - 0.7 85	0.45 - 0.65 95	0.25 - 0.45 89	0.7 - 2.0 96	0.7 - 0.8 94	0.45 - 2.0 98	0.6 - 1.0 99
0.4 - 2.0 90	- -	0.25 - 0.70 85	2.0 - 10.0 96	0.8 - 2.0 97	2.0 - 10.0 98	
				2.0 - 12.0 98		

Figure 21 Typical reflectance curves for metallic mirror coatings from near-infrared to mid-infrared region [51].

Since the reflectivity of the mirrors are not ideally perfect, there occurs such losses for each pass in the multi-pass system. By considering the measurement, the maximum achievable signal to noise ratio (SNR) for optical path length should be determined. When the optical path is too long, the intensity of the light decreases dramatically that cannot be detected with regard to the noise level of the system. On the contrary, while the optical path is too short, the absorption cannot be detected for the weak lines. Therefore, the SNR of the system and the absorption level of weak lines are the constraints to determine the optimum path length and the number of passes. Steyert [49] states that since the principle noise level is caused by the photon variation in thermal background, it does not depend on the laser to be used. For weak

lines, the optimum number of passes was studied by Doussin *et. al.* [46] for the case where the noise of the system is caused by the photon.

For the case of weak line absorption, the absorbance A can be expressed as,

$$A = \ln \frac{I_0}{I} \approx \frac{I_0 - I}{I} \quad (4)$$

$I_0(\lambda)$, the incident intensity of light, is almost equal to $I(\lambda)$, the intensity after weak line absorption. The optimum pathlength can be determined by maximizing the SNR defined as follows,

$$SNR = \frac{A}{\delta A} \quad (5)$$

Now, by differentiating the absorbance which is given in Equation 4, δA can be obtained as following,

$$\delta A \approx \delta \left(\frac{I_0 - I}{I} \right) \approx \frac{\delta I_0}{I} + \frac{I_0 \times \delta I}{I^2} \quad (6)$$

Since the spectrum is measured in the same experimental conditions, the variations on the incoming light δI_0 will be almost equal to δI . Therefore, δA can be expressed as,

$$\delta A \approx 2 \frac{\delta I}{I} \quad (7)$$

The photons are distributed on a detector according to Poisson's law, intensity error can be defined as the standard deviation σ that is linear with \sqrt{I} .

$$\delta A \approx 2 \frac{\sqrt{I}}{\sqrt{I^2}} \approx \frac{2}{\sqrt{I}} \quad (8)$$

The absorbance defined by Beer-Lambert's law directly depends on the optical path length and therefore the number of passes. If the number of reflections is defined as p , the number of pass will be $p+1$ and absorbance can be written as,

$$A \propto (p + 1) \quad (9)$$

As it mentioned before, in a multi-pass optical system, the major energy lost originates from the absorption of light via the mirrors. Thus, the intensity coming to the detector is proportional to p^{th} power of the reflectivity.

$$I \propto R^p$$

As a result, the SNR becomes,

$$SNR \propto \frac{p + 1}{2\sqrt{R^p}} \propto \frac{1}{2} (p + 1) R^{p/2} \quad (10)$$

Finally, the optimum number of reflections in a multi-pass matrix system can be found by maximizing the Equation 10. It can be found by differentiating the equation with respect to n and equating it to 0.

$$p = \frac{-2}{\ln(R)} - 1 \quad (11)$$

By using the formula obtained in Equation 11, the importance of the reflectivity of coating on the number of passes in a multi-pass matrix system can easily be seen [46]. For instance, if the reflectivity of the coating is $R=0.98$, the optimum number of passes for the weak lines is approximately 99; if $R=0.99$, the number of passes would be 199.

In my design, since the reflectivity of the coating on the mirrors is roughly 0.98 for mid-infrared spectral range, the optimum number of passes should not exceed 99 for the absorption measurements of weak lines. Therefore, the multi-pass matrix system has been designed for minimum 6x6 matrix form which provides 72 passes. However, with this design to obtain less or greater number of passes are also possible.

Since the absorption can be observed clearly in strong line spectroscopic measurements, SNR is not the case taking into consideration anymore. However, it can be calculated numerically without using the approximation which was used for weak line calculation given in Equation 4. Therefore, the formula given in Equation 11 is not valid for that case.

2.2.1.2 Mirror Dimensions

In my design, with 6x6 matrix arrangement there exists 36 images on the field mirror group, T_1 and T_2 . Therefore, the mirror T_1 contains 30 images (6x5) of radius r_i where no images overlap. Although Glowacki *et. al.* [42] states that T_1 should have a dimension of at least $16r_i \times 14r_i$ and T_2 should have a dimension of at least $14r_i \times 2r_i$, due to the constraints caused by mechanical mounts, the dimensions given are not possible. Even though the mechanical mounts would not obstruct the clear aperture of the mirrors, there should be a gap between T_1 and T_2 that allows them to rotate about the horizontal axis. Therefore, the images on the Glowacki *et. al.*'s proposed minimum-size field mirrors are all adjacent to each other, which is not possible for the images in the T_2 mirror and the images in the top row of the T_1 mirror.

In order to calculate the optimum length and width of the field mirrors, entrance beam diameter should be known. If the source provides a divergent light beam, the divergence and the focal length of the transfer optics should be taken account. The beam diameter can be calculated by using the following paraxial formula,

$$D = \frac{a \cdot d}{f_f} + 2r_0 \quad (12)$$

where D is the beam diameter at a distance d from the source's exit aperture whose size is $2r_0$. a is the aperture size, and f_f is the focal length of the final mirror which is an off-axis parabolic mirror.

Since the design was made considering the atmospheric gas absorption studies in the mid-infrared spectral region, the field mirrors were designed according to the characteristics of the infrared laser that can be found in the following table.

Table 3 Several beam characteristics of lasers to be used.

<i>Light source</i>	<i>Type</i>	<i>Beam diameter</i>	<i>Beam divergence</i>	<i>Wavelength range</i>
NT242 Ekspla	OPO	3x6 mm	10 mrad	210 nm – 2.6 μm
NT277 Ekspla	OPO	6 mm	10 mrad	2.5 μm – 12 μm
SuperK Compact NKT	Supercontinuum	1-3 mm	collimated	450 nm – 2.4 μm

Since the beam divergence is significant for Optical Parametric Oscillators (OPO), an off-axis parabolic mirror should be used to collimate the divergent light.

The initial performance analysis was done by using the SuperK Compact White Light Supercontinuum Laser source of NKT Photonics. Since the beam is collimated,

the beam diameter measured at the output aperture of the laser is equal to the beam diameter projected on to the field mirrors.

According to the optimum number of passes calculation mentioned in design parameters section, it was determined as 6x6 matrix form with 72 passes. Mirror dimensions should be determined according to the beam diameter and beam divergence of the laser or other light sources to be used.

While determining the mirror dimensions, not only the clear aperture but also the chip-zone should be considered, especially since the field mirrors are placed one above the other. Since the laser source to be used in the experiments produces collimated light with a beam diameter of 1 mm at a wavelength of 532 nm, its size on the field mirrors will also be approximately 1 mm. A 2 mm chip zone is left for each of the small and large area mirrors. Since the distance between the mirrors is determined as 2 mm, there should be at least 6 mm difference between the beams formed on the mirror.

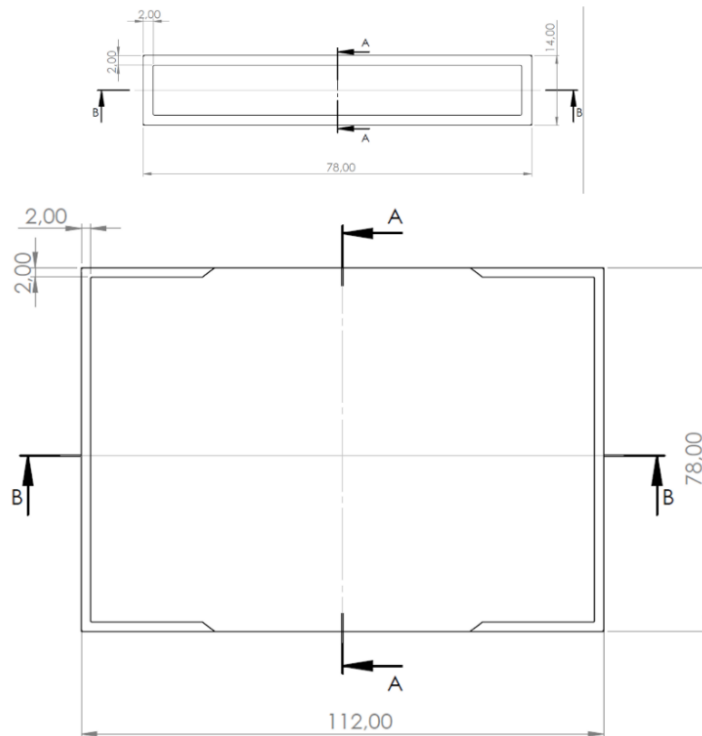


Figure 22 Technical drawing of field mirrors T₁ and T₂.

Therefore, for the 6x6 matrix configuration, the dimensions of the T₁ mirror with the chip zone must be at least 28 mm x 5 mm and the dimensions of the T₂ must be 39 mm x 28 mm. However, the dimensions of the field mirrors have been chosen as 112 mm x 78 mm for T₁ and 78 mm x 14 mm for T₂ (Figure 22) so that the design can also be used with laser sources with much larger beam diameter and beam divergence.

2.2.1.3 Path Length

The path length that is equal to the radius of curvature of the mirrors is arbitrary. Since the effective length of the trace gas measurement chamber is 1 meter, at first the mirrors were designed so that the radius of curvature is 1000 mm long. However, in our facilities, since the test plate cannot measure the surface of the optics with their radius of curvature is greater than 600 mm, the design has been changed. Therefore, with 6x6 matrix arrangement, the optical path length becomes 43.2 meters.

2.2.1.4 Resolution

In the design, the needed resolution that has an impact on aperture size should also be considered as the aperture size directly related with the image size on the field mirrors. The resolution can be expressed as following,

$$\Delta\nu_{attainable} = \frac{a^2}{8f_f^2} \nu_{maximum} \quad (13)$$

where $\Delta\nu_{attainable}$ gives the best and the smallest possible resolution attainable that can be obtained at all wavenumbers less than $\nu_{maximum}$. In my design, the best resolutions obtainable according to different spectral ranges are given in the following table.

Table 4 Best resolutions obtainable by the multi-pass matrix optical system according to different spectral ranges.

<i>Spectral range</i>	<i>Aperture size</i>	$\Delta\nu_{attainable}$	$\nu_{maximum}$	<i>Resolution of Spectrometer</i>	<i>Spectrometer</i>
Visible range	1 mm	2.31×10^{-2}	4167 cm^{-1}	0.18 nm	Maya 450 to 2400 nm Ocean Insight
NWIR range	3 mm	1.92×10^{-1}	3846 cm^{-1}	4 cm^{-1}	FT-NIR Rocket 900 to 2600 nm Arcoptix
MWIR range	6 mm	1.66×10^{-1}	833 cm^{-1}	0.5 cm^{-1}	FT-IR Rocket 2 to 12 μm Arcoptix

It is assumed that an off-axis parabolic mirror with 150 mm focal length is used. As shown in the table, the resolution obtained by multi-pass matrix system is higher than the resolution of the spectrometers. Therefore, it is limited with the instrument.

2.2.2 The Design Process

The design process starts with defining the initial parameters that include row number, column number, system width, system height and the base length which is the distance between the mirrors. Then, by using Equation 11, the number of passes for the weak lines is calculated and it is controlled whether the calculated pass number exceeds the maximum value, or not. In addition, ratio of the width of the field mirror to the number of rows should not be exceed the size of the light beam. If the parameters are satisfied then, the ray trace simulations via Zemax OpticStudio can be run. After that, the variables, boundary conditions and the merit functions are defined and optimized the system. Until the performance analysis becomes good enough for the system requirements, the previous process is repeated. For this case, the performance is evaluated with chromatic aberration since the source is white light

supercontinuum laser; wave front peak to valley (PV) value, and Zernike coefficients. Then, after tolerancing, the required parameters are defined for manufacturing process. Figure 23 indicates the general flow of the design process of multi-pass matrix optical system.

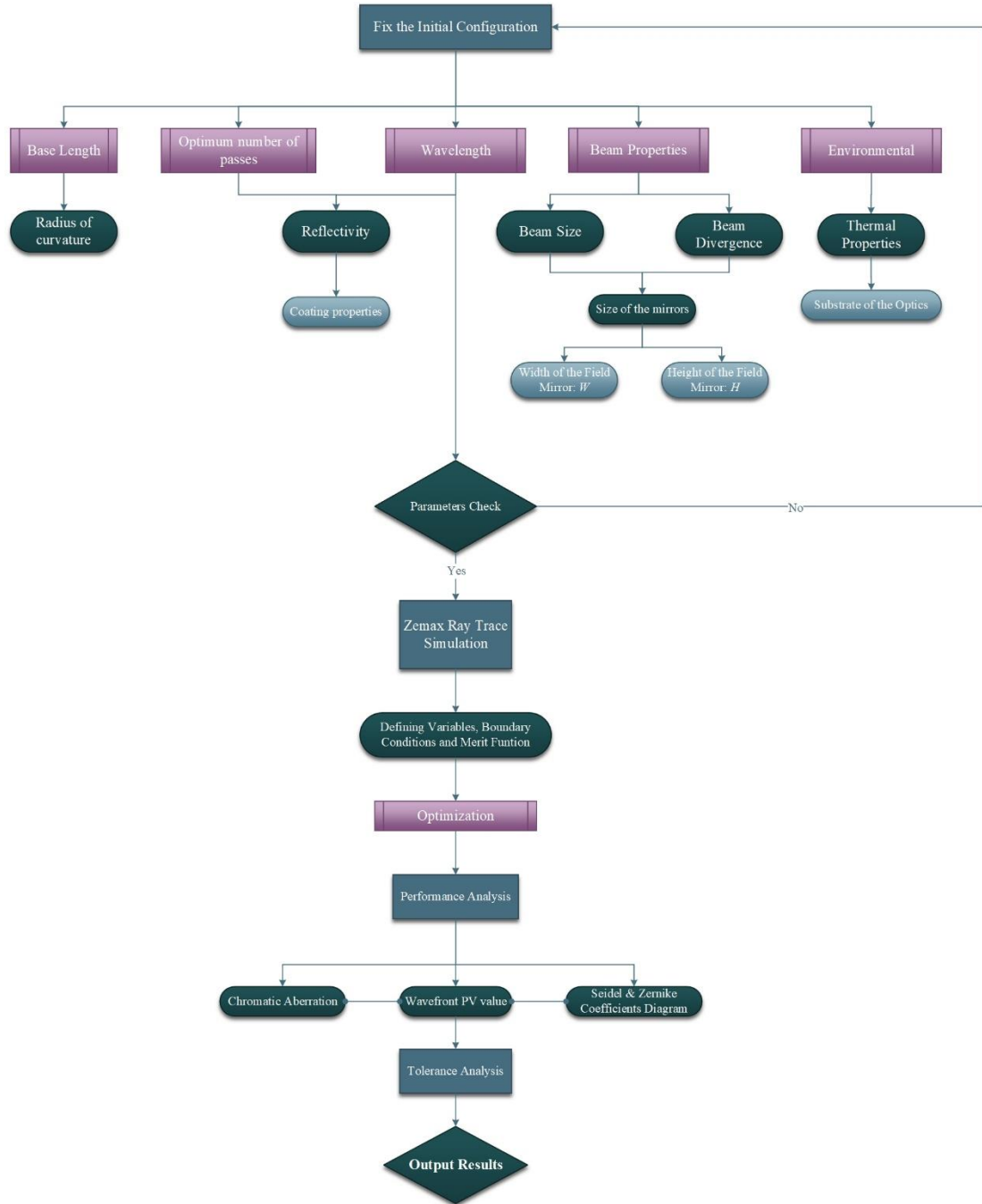


Figure 23 Flow chart of the design process of multi-pass matrix optical system.

Ray tracing simulation of the optical system was done in non-sequential mode of Zemax OpticStudio software. In non-sequential ray tracing mode, optical components include solids and surfaces, are defined as 3-dimensional independent objects. In this mode, each object can be placed in the desired position in the Cartesian coordinate system, with the desired angles. Unlike the sequential ray tracing mode, this mode does not require a surface to be hit by the traced rays in a sequential manner. Therefore, the defined rays do not have to hit any part of the objects. On the contrary, it may hit a specific place or hit the same object multiple times. Non-sequential mode is generally used in situations where it cannot be modelled accurately in sequential mode, complex, where the exact path of the beam cannot be predicted, or where light has to pass repeatedly between optical elements, such as in a multi-pass matrix optical system.

Non-sequential ray tracing can be modelled by using pure non-sequential mode or using the mixed sequential mode. In pure non-sequential ray tracing mode, all optical elements, including detectors, light sources, are in a single non-sequential group, and the light source is not a point source as in sequential mode, but has a diverse library. Detectors, on the other hand, are effective in examining various types of data, including incoherent irradiance, coherent irradiance, coherent phase, irradiance intensity etc. Mixed mode ray tracing, which is a mix of sequential and non-sequential ray tracing, is generally used for optical designs where objects that cannot be identified sequentially need to be identified, but due to the nature of the system, they must be examined sequentially [52]. For multi-pass matrix optical design, both mixed non-sequential and pure non-sequential ray tracing mode were performed.

The simulation starts by determining the wavelengths to be studied in the system explorer using the pure non-sequential mode of OpticStudio. Although the first design was carried out in the infrared region, which is more significant in atmospheric trace gas measurement studies, the wavelengths to be studied within the scope of this thesis were determined to be between 450-850 nm as shown in Figure 24.



Figure 24 Wavelengths section in System Explorer tab.

Next, the multi-pass optics, the detectors to be used, and the light source must be defined in the non-sequential component editor. The non-sequential component editor is used to add and delete objects, select object types and properties, and to set solves and variables. In this tab, the position and angle of the objects in the cartesian coordinate system can be defined, the radius of curvature, clear apertures and mechanical apertures, materials and coatings can be determined. An example image of the non-sequential component editor is shown below:



Figure 25 Non-sequential component editor in OpticStudio.

The laser source should be defined in the non-sequential component editor. Since the light source to be used in performance analysis studies is a supercontinuum white light laser with a gaussian beam profile, it is defined as "Source Gaussian" in OpticStudio. In the editor, the beam radii at $1/e^2$ point in light intensity of the gaussian light source was determined as 0.5 mm. It is also necessary to define the

position parameter, which states the divergence of the light beam. Since laser beams are collimated, this value is equal to 0.

The position of the light source was determined to pass through the aperture between T_1 and T_2 . Layout rays represent the number of rays seen in the simulation, while analysis rays show the number of rays to be analyzed by the detector.

The next step is to define the field and objective mirrors in the editor. Since the objective mirrors have a standard 2 inches concave circular shape, they can be selected as standard surface or standard lens among the object types, but since the field mirrors have a special geometry, they cannot be defined as a standard object.

One of the ways to create optical surfaces with non-standard forms in OpticStudio is to define aperture manually. First, the standard surface is selected as the object in the nonsequential component editor, then the desired aperture can be defined with the "edit aperture file" in the "user defined aperture" section in the object properties tab. In this method, center of the object is at the origin and edge points of the closed surface are defined in cartesian coordinate system. Surface apertures for T_1 and T_2 are defined as given in the Figure below:

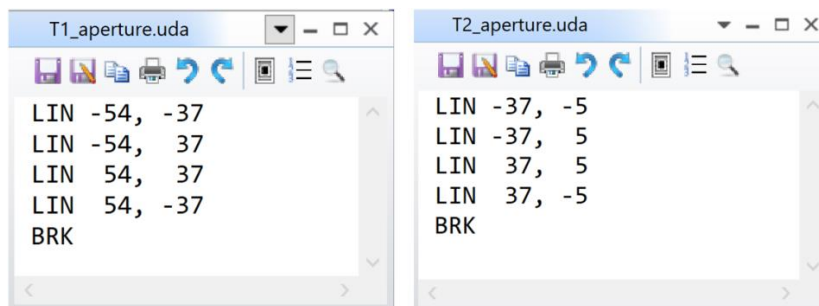


Figure 26 Aperture definition for T_1 and T_2 field mirrors.

After determining the radius of curvature, position and the material of the mirror whose aperture is defined, protected silver coating is selected in the "coat/scatter" section in the object properties tab. Since there is no Zerodur that is planned to be

used as a material in the Schott catalogue, the material properties can be entered manually from the library/material catalogue tab. For this study, no thermal analysis will be performed, so only the coating on the optics is important, not the substrate.

Another way to define non-standard optical objects in OpticStudio is to import the objects to be created in CAD programs. The downside of this method is that parameters such as radius of curvature, size, and thickness cannot be changed, but since it becomes a 3-dimensional object, it is ideal for analysis such as temperature etc. Therefore, in this study, after the design was completed, solid models were created in SolidWorks software and imported into OpticStudio. 3-D models can be found in the Figure 27:

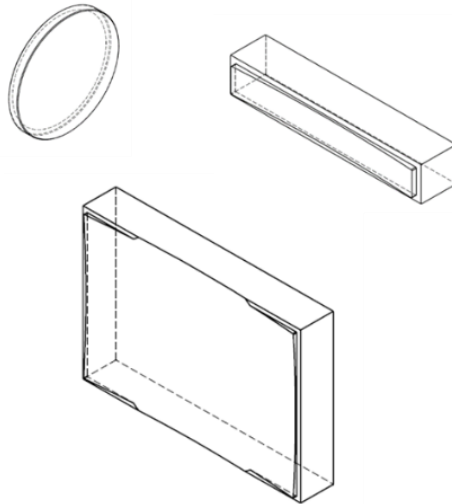


Figure 27 Solid models of multi-pass mirrors.

The objective mirrors were chosen as standard lenses and their dimensions were determined to be 2 inches and the chip zone to be 2 mm for mechanical mountings. The radius of curvature of field mirrors facing +z direction defined as 600 mm and of objective mirrors facing -z direction as -600 mm. Then, the positions of the objects in the Cartesian system were determined as given in the table below:

Table 5 Positions of multi-pass optics in mm.

<i>Object</i>	<i>x position</i>	<i>y position</i>	<i>z position</i>
Source Gaussian	48	48	0
T ₁	0	0	0
T ₂	0	48	0
O ₁	48	48	600
O ₂	-11	48	600
O ₃	-11	-11	600

After the light comes out of the source, it first falls in the middle of the O₁ mirror, and according to the model, a certain angle must be given to it so that the light reflected from the surface can fall on the mirror, T₂. At this point, the position where the light should fall is calculated and a "detector rectangle" object is placed at that point as shown in the Figure 28. The x and y halfwidths of the detector are defined as 2 mm and the number of pixels as 250x250.

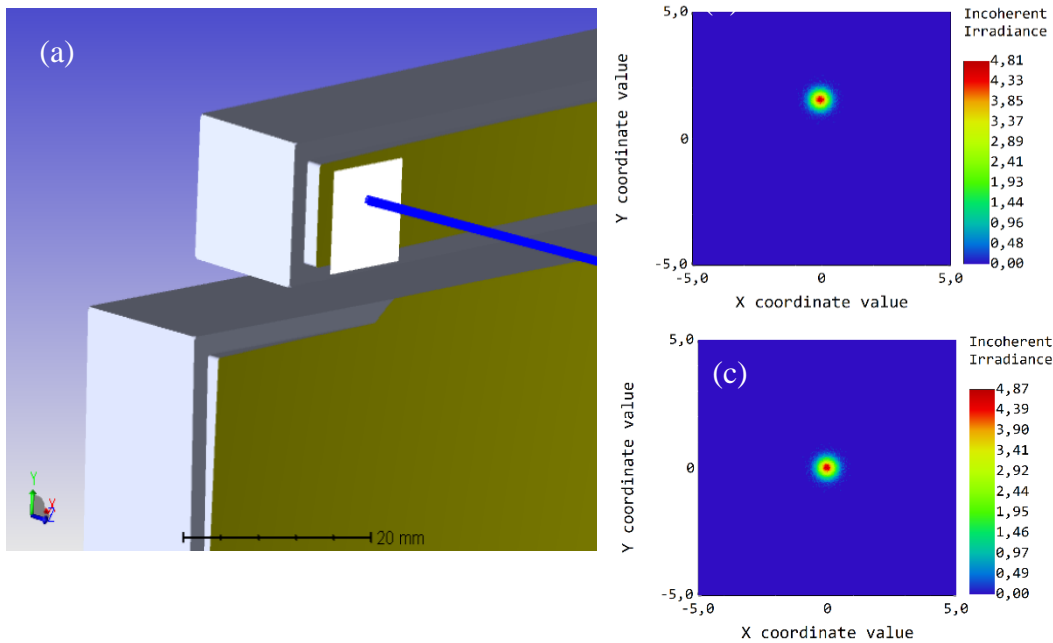


Figure 28 (a) The detector placed at the point where the light reflected from O₁ aims to hit. (b) Spot position on the detector before optimization. (c) Spot position on the detector after optimization.

After assigning “variables” to the “x tilt” and “y tilt” parameters of the mirror, optimization criteria is determined in the optimization wizard tab in the merit function editor. Since the aim is to direct the laser beam to the middle point of the detector, “x centroid” and “y centroid” were determined as optimization criteria, the target was selected as 0 and it was specified which detector would be optimized by reference before local optimization. An example for merit function editor is given in Figure 29.

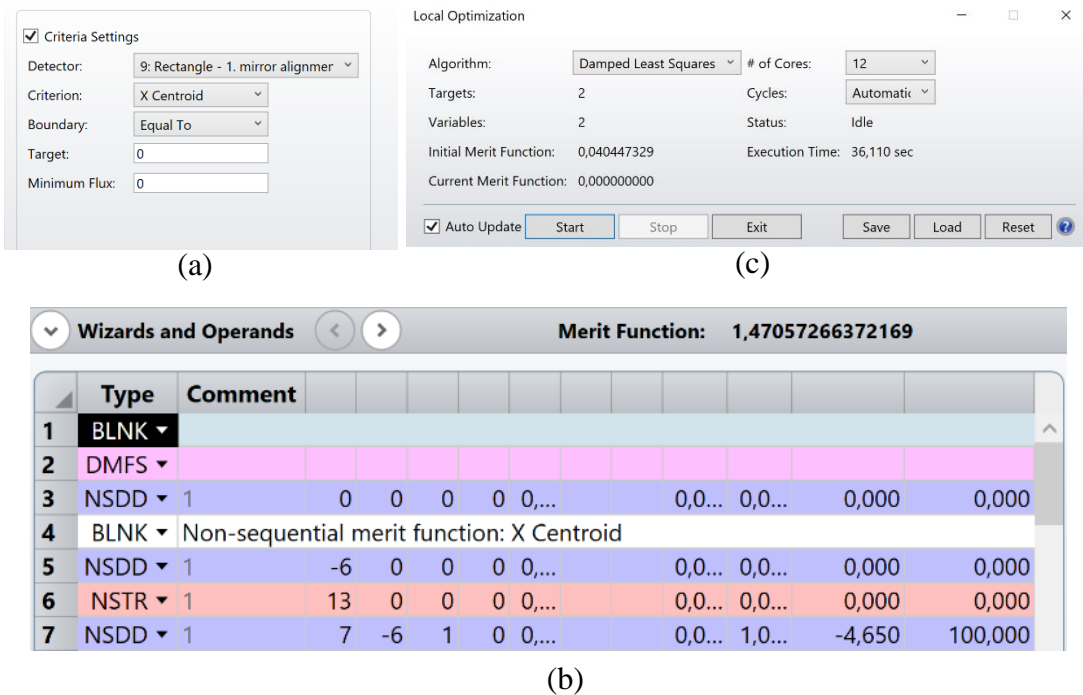


Figure 29 (a) Criteria settings in optimization wizard. (b) Local Optimization tab. (c) Merit Function Editor.

After defining the criteria in the optimization wizard, the merit function is created automatically. In Figure 30 (c), operators that allow the light to center the detector are given. BLNK is used for separating portions of the operand list. DMFS is default merit function start. NSDD is non-sequential incoherent intensity data and NSTR is non-sequential ray trace.

After making sure that the light falls on the point where it should fall on the mirror T_2 , the detector is removed and placed in the middle of the O_2 mirror. This time, the same operations are performed after the variables are assigned to the "tilt x" and "tilt y" parameters of the mirror T_2 . These processes are repeated until the alignment of mirrors O_2 , T_1 , O_3 is completed respectively. Finally, another detector rectangle is placed at the point where the light will exit the system for analysis of the beam.

Figure 30 shows the ray trace simulation of the multi-pass matrix optical system designed via Zemax OpticStudio software. The simulation indicates 72 passes with 6x6 matrix arrangement.

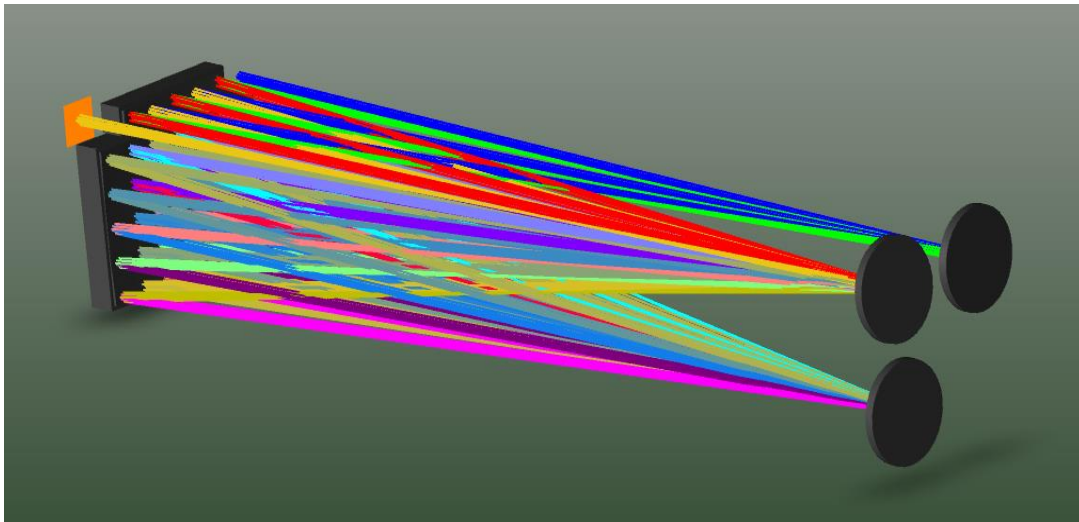


Figure 30 Shaded Model of multi-pass matrix optical system designed via Zemax OpticStudio Software.

2.2.3 Simulation Analysis

Detector rectangles were placed in front of the laser source and at the exit point of the laser completing 72 passes. According to the analysis, it was observed that there were distortions after the transition in the beam with Gaussian profile at the beginning.

The spatial irradiance distribution, cross-section graphs (Figure 31) and power values (Table 6) for the final light beam which completes the transition between the multi-pass mirrors and the input beam are given below:

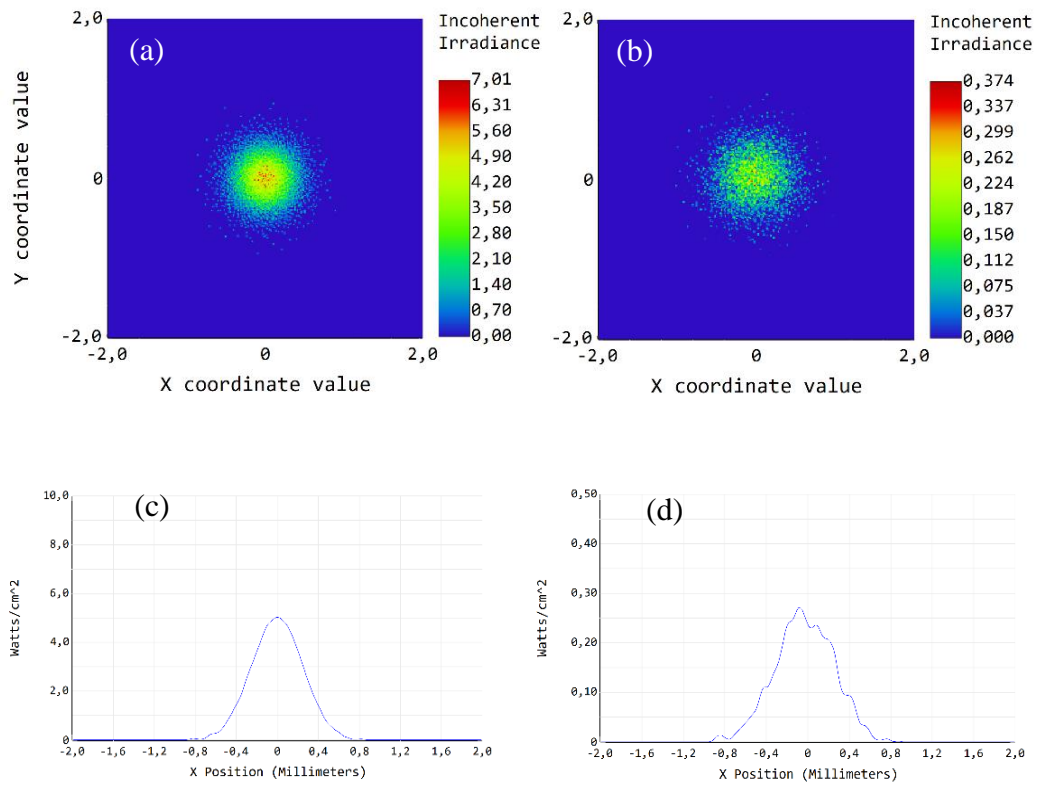


Figure 31 Spatial irradiance distribution of simulated incoming (a) and outgoing (b) gaussian laser beams and cross section graphs of incoming (c) and outgoing (d) gaussian laser beams.

Table 6 Power analysis of incoming and outgoing beams.

<i>Detector</i>	<i>Peak Irradiance</i>	<i>Total Power</i>
Input	7 W/cm ²	2x10 ⁻² W
Output	3.74 x10 ⁻³ W/cm ²	8.55x10 ⁻⁴ W

In OpticStudio, reflective coating of the optics has been selected as protected silver that provide above 95,7% reflectivity (Figure 32) for visible spectral range. The reduction in the power of the laser beams obtained after 72 passes is the result of the amount of absorption of protected silver coating. Roughly speaking, since the light loses approximately 4% of its power in each reflection from the mirror, the final power of the light beam will be equal to approximately $I_0.(95,7 \%)^{72}$ which is $8.55 \times 10^{-4} \text{ W}$.

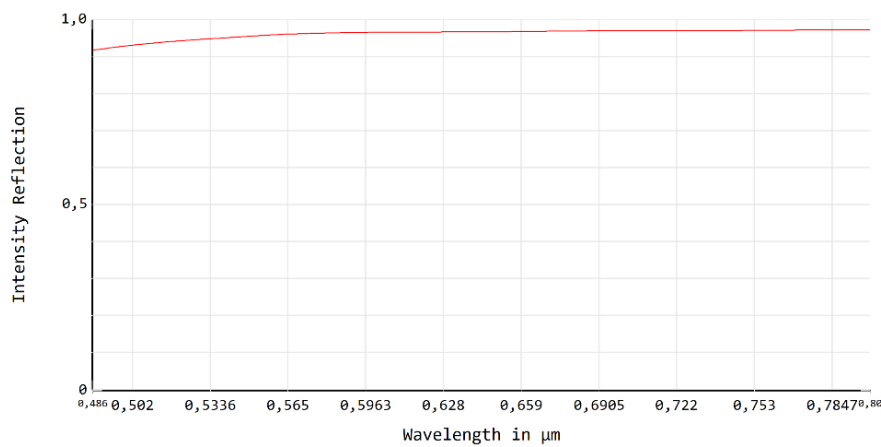


Figure 32 Reflection vs wavelength graph of protected silver coating in OpticStudio.

The reflectivity value for the protected silver coating is different at each wavelength, and as the wavelength increases in the range of 450-850 nm, the reflectivity also increases. In this case, in spectroscopy studies, lower wavelengths of broadband laser beams from a super-continuum white light source will reach the detector relatively less than those with longer wavelengths. Although the spectra of the laser source was not properly defined in OpticStudio, it has been assumed that it contains all wavelengths homogeneously between 450-650 nm spectral range. The real spectral radiation graph of the laser source to be used in performance studies is given below:

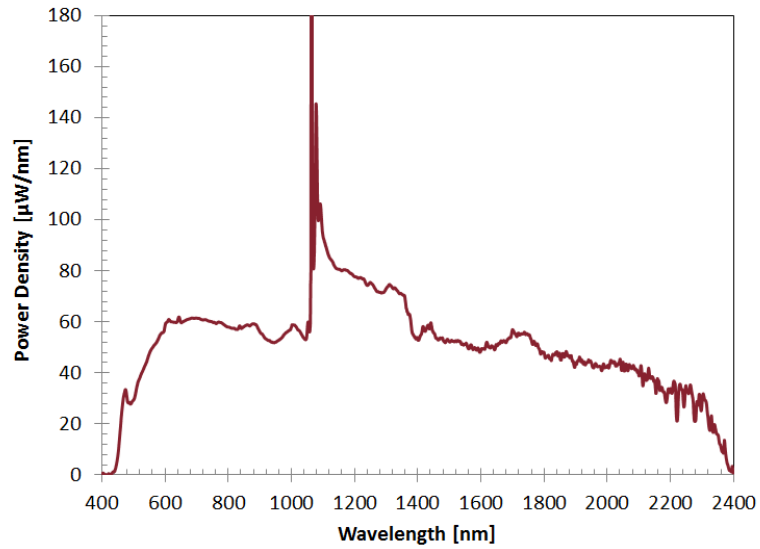


Figure 33 Power density vs wavelength graph of NKT Compact Supercontinuum White Light Laser [53].

The wavelength graphs against the light intensity obtained from the detectors placed in the entrance and exit aperture are given in Figure 34.

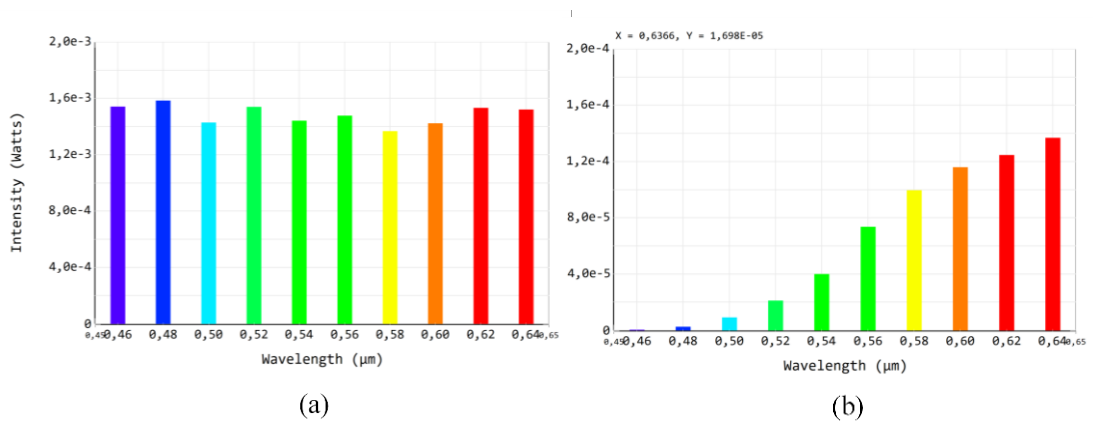


Figure 34 Intensity vs wavelength graphs for incident (a) and outgoing (b) light beams.

According to the graph, it is observed that near the wavelength of 450 nm, incoming rays according to the 72-transition configuration are highly absorbed by the mirrors.

If the intensity at all wavelengths was not considered the same in the simulation and the real laser spectrum was used as in Figure 33, only long wavelengths would be able to reach the detector. Thus, it may not be very suitable to use this system for materials with low wavelength absorption bands in multiple pass measurements to be made with this coating.

Figure 35 and Figure 36 show the spatial irradiance distribution of laser beams at different wavelengths and at all wavelengths between 450 nm and 650 nm.

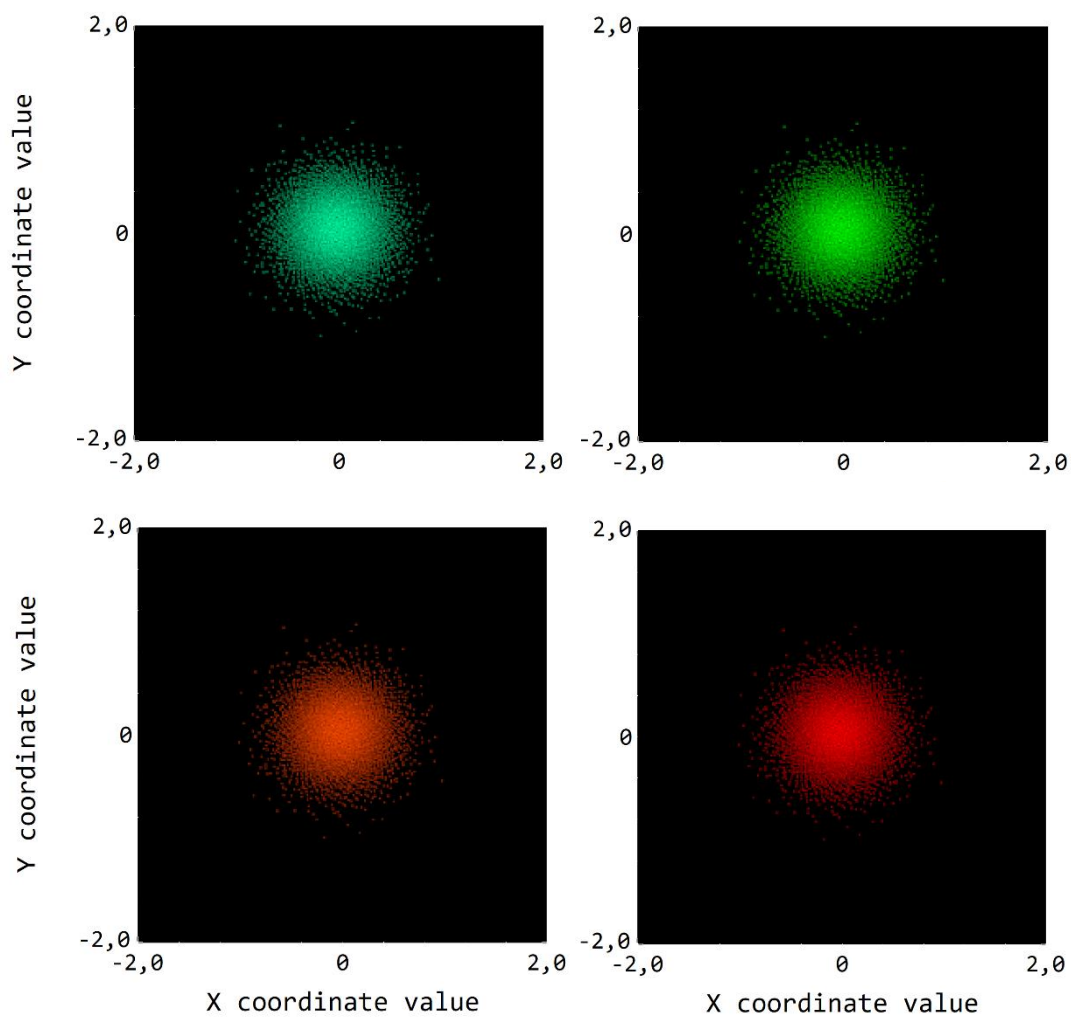


Figure 35 Spatial irradiance distribution of laser beams at (a) 500 nm (b) 550 nm (c) 600 nm (d) 650 nm wavelengths.

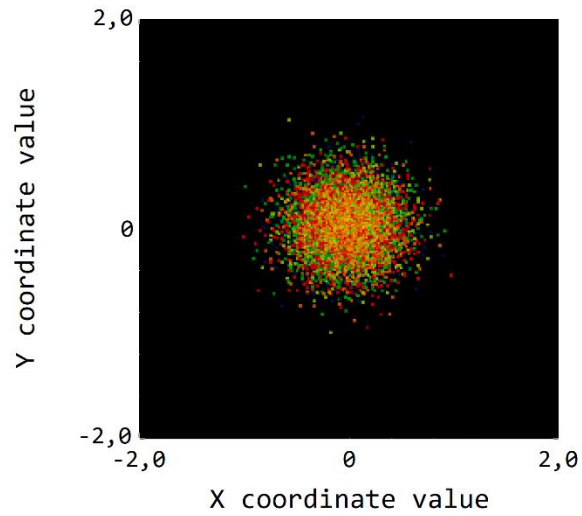


Figure 36 Spatial irradiance distribution of laser beams at 450, 500, 550, 600, 650 nm.

Table 7 Spot information of laser beams at different wavelengths.

<i>Wavelength</i>	<i>RMS Spot Radius</i>	<i>RMS Spot x</i>	<i>RMS Spot y</i>	<i>Centroid x</i>	<i>Centroid y</i>
0.450 - 0.516	0.3953812	0.28881433	0.27002332	-0.02133025	0.04514792
0.516 - 0.583	0.3944444	0.28272975	0.27504605	-0.02833959	0.04359940
0.583 - 0.650	0.3963283	0.28509439	0.27531319	-0.03671505	0.04187253

According to the spot analysis for wavelengths between 450 and 650 nm spectral range obtained by ray tracing simulation, the RMS and geometric spot deviations at different wavelengths show slight variation.

Since this design is not an imaging system, optical aberrations do not have a significant negative impact. The aberrations are expected to be such that they do not simply reduce the amount of signal falling on the detector. In this design, since the output beam is not directly coupled to the fiber of the spectrometer, there is no need for focusing. Therefore, it is not concerned how the image of the light beam is distorted after a couple of off-axis reflections.

However, the image quality of the output beam is investigated in terms of Zernike Polynomials which are all orthogonal over the unit circle and can be used to represent wave front errors such as coma, astigmatism etc. in optics [54].

In the polar coordinates the wave aberration function can be expressed as a complete set of Zernike polynomials:

$$W(\rho, \theta) = \sum_{j=1}^{\infty} a_j Z_j(\rho, \theta), \quad (14)$$

where j is the number of the polynomial, a_j is the expansion coefficient, $Z_j(\rho, \theta)$ is the Zernike coefficient in polar coordinates which can be expressed as:

$$Z_j(\rho, \theta) = \left[\frac{2(n+1)}{1 + \delta_{m0}} \right] R_n^m(\rho) \cos m\theta, \quad (15)$$

where n is the radial degree and m is azimuthal frequency, $R_n^m(\rho)$ is the radial part of the Zernike polynomial. Therefore, if $m=0$, the delta function is 1 and vice versa. a_j is the expansion coefficient can be written as:

$$a_j = \frac{1}{\pi} \int_0^1 \int_0^{2\pi} W(\rho, \theta) Z_j(\rho, \theta) \rho d\rho d\theta \quad (16)$$

The Table 8 indicates the Zernike coefficients in polar coordinates from 1st to 10th, their corresponding wave front aberrations and values obtained from OpticStudio software.

Table 8 The Zernike coefficients and corresponding optical aberrations at 600 nm wavelength.

<i>j</i>	$Z_j(\rho, \theta)$	<i>Aberration</i>	<i>Value</i>
1	1	Piston	0,42183851
2	$2\rho \cos\theta$	Tilt x	-0,00026313
3	$2\rho \sin\theta$	Tilt y	-0,00005185
4	$\sqrt{3} (2\rho^2 - 1)$	Defocus	0,24355073
5	$\sqrt{6} \rho^2 \sin 2\theta$	Astigmatism (45°)	0,00029711
6	$\sqrt{6} \rho^2 \cos 2\theta$	Astigmatism (0°)	0,02012239
7	$\sqrt{8} (3\rho^3 - 2\rho) \sin\theta$	Coma x	-0,00001830
8	$\sqrt{8} (3\rho^3 - 2\rho) \cos\theta$	Coma y	-0,00009309
9	$\sqrt{8} \rho^3 \sin 3\theta$	Trifoil (30°)	-0,00001788
10	$\sqrt{8} \rho^3 \cos 3\theta$	Trifoil (0°)	0,00000361

According to the Zernike coefficients obtained from the image surface, piston and defocus aberrations stand out compared to other aberrations. In optical systems, piston can be defined as the mean value of the wavefront profile across the pupil and when the image is out of focus, this aberration is called defocus. However, as noted, these aberrations have no effect on system performance since there is no imaging intent. If imaging is needed in another application, the existing optical system can be worked on or additional optics can be designed to correct the wavefront deviation.

In addition, the wavefront of the laser beam is also examined in terms of Peak to Valley (PV). At 600 nm, PV value is 0.8937 and RMS is 0.244 waves as shown in Figure 37.

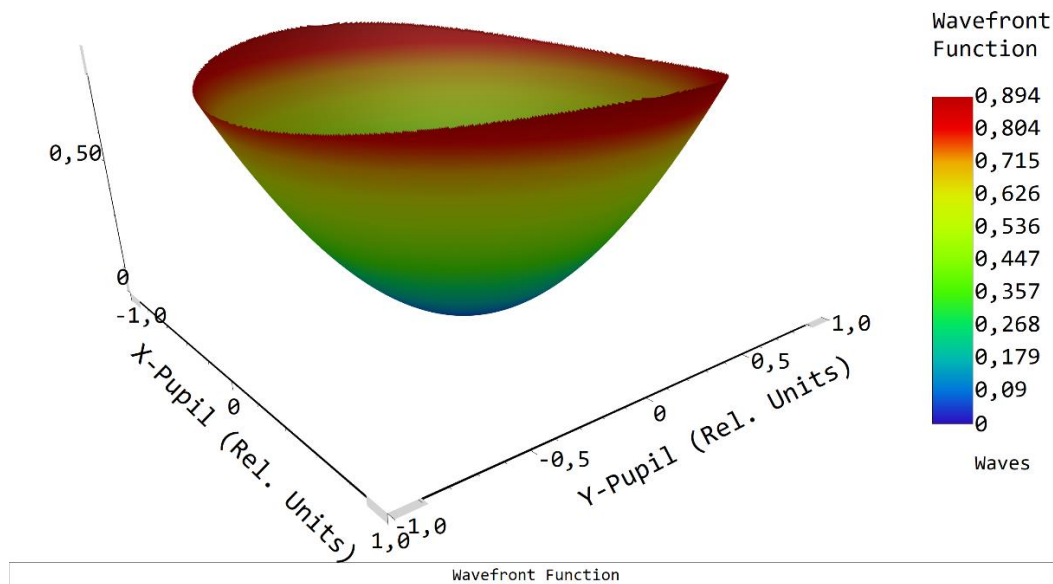


Figure 37 Wave front of laser beam.

2.2.4 Tolerancing

Before an optical system is produced, tolerances must be made due to errors such as production, assembly and material. The tolerance process is necessary to determine how the system will be affected by these faults and to see how these faults will be applied to the system. There are three operands to tolerance non-sequential objects in non-sequential mode. The TNPS operator is used for tolerating the positions and tilts of non-sequential objects, the TNPA operator is used for parameters, and TNMA is used for material properties. In addition, the CNPS and CNPA operator provide non-sequential object positions/tilts and parameters to be assigned as compensators [55].

In non-sequential mode tolerance analysis, the variables are defined only by compensators. Therefore, all variables used during optimization should be removed. Then, it is necessary to evaluate the errors that may cause the manufactured system to perform worse than the optimized system. These errors are manufacturing errors, the location and direction of the optics, the location and direction of the light source, the location and direction of the detector, and mounting errors.

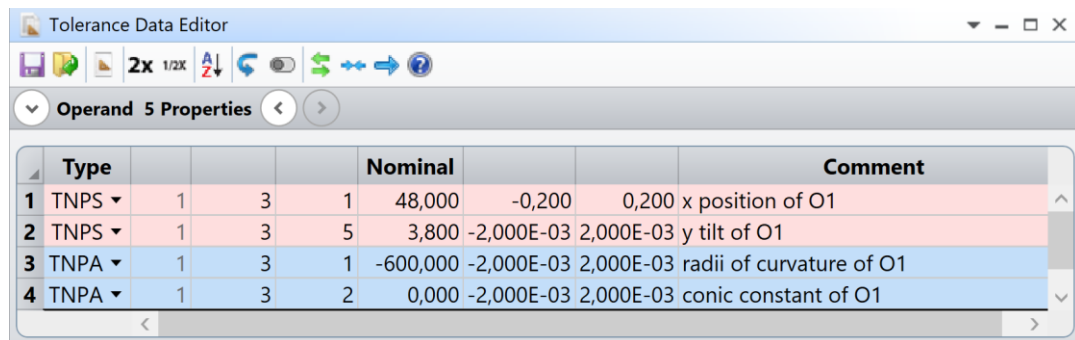
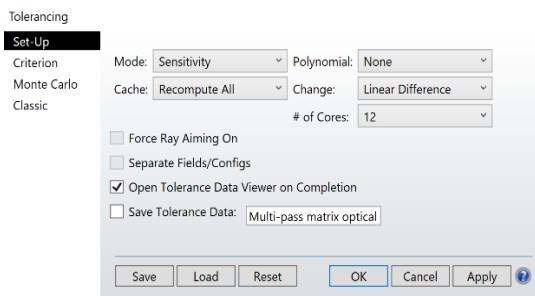


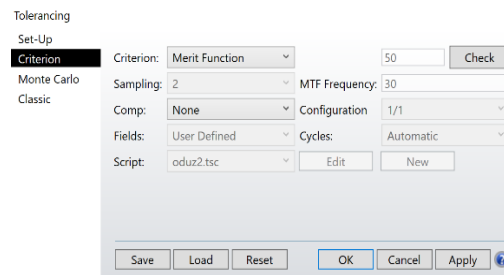
Figure 38 Tolerance data editor in OpticStudio.

For the multi-pass matrix optical system, the errors that will affect the system may be the radius of curvature, the size and the conic constant of the mirrors. However, since the system is inherently flexible, all these errors are manually tolerable during optical setup. For example, the distance between the mirrors must be equal to the radius of curvature of the mirrors. In this case, if the radius of curvature of any mirror is produced more or less than the desired value, the problem can be solved by adjusting the distance according to this value. However, this only applies to desktop prototypes that allow flexible positioning. On the contrary, if the mirrors of the multi-pass matrix optical system are to be mounted on the inner walls of the atmosphere chamber, then the focal properties of the beam will be lost, so an increase in the diameter of the beam emerging from the system can be observed. Therefore, it is necessary to evaluate the possible faults that may change the performance of the system.

Next, the tolerance settings need to be defined. In this study, tolerancing was done using sensitivity analysis and Monte Carlo simulation. The sensitivity mode calculates the change in the tolerance criterion for each of the extreme values of the tolerances that have been set as the minimum and maximum in the tolerance data editor. The tolerance criterion is defined as the merit function in the tab labeled 'Criterion' given in Figure 39 (b).



(a)



(b)

Figure 39 (a) Set up section and (b) criterion section in tolerancing tab.

Then, tolerancing can be started. After all tolerances have been calculated, the software provides various statistics including estimated change and performance in the specified criteria.

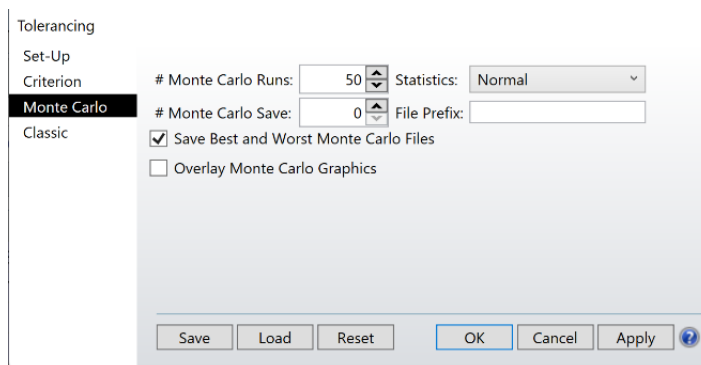


Figure 40 Monte Carlo section in tolerancing tab.

While "sensitivity" analysis in tolerance analyzes the effect of each parameter on system performance separately, Monte Carlo analysis simulates the effect of all disturbances at the same time. Similar to the sensitivity in Monte Carlo simulation, first of all, tolerances are defined in a certain range for the required parameters. Then the Monte Carlo simulation takes place in this defined range by choosing random values according to a statistical model.

After the tolerance analysis performed in OpticStudio, the manufacturing parameters given in the Table 9 are determined.

Table 9 The basic properties of multi-pass matrix optical system after tolerancing analysis.

<i>Specification</i>	<i>T₁</i>	<i>T₂</i>	<i>O₁, O₂, O₃</i>
Radius of curvature	600 ±0.02 mm	600 ±0.02 mm	600 ± 0.02 mm
Dimension	112 mm x 78 mm	78 mm x 14 mm	50.8 mm
Surface quality	20/10	20/10	20/10
Surface roughness	10 Å RMS	10 Å RMS	10 Å RMS
Clear aperture	108 mm x 74 mm	74 mm x 10 mm	46.8 mm
Irregularity (P-V)	λ/4	λ/4	λ/4
Tilt	15 arcsec	15 arcsec	15 arcsec
Material	Zerodur	Zerodur	Zerodur
Center Thickness	15 mm ±0.05 mm	15 mm ±0.05 mm	4mm ±0.05 mm

The quality of an optical surface is defined by surface imperfections called scratch, pits and digs. Although these defects do not have significant effects on optical performance, they increase the amount of light scattered from the surface. Scratches are determined by comparing the scratches on optical surface determined as standard in illuminated conditions according to specified standards. Dig is explained by dividing the dig diameter in microns by 10. 80-50 Scratch/dig is typically considered as standard quality, 60-40 as precision quality, and 20-10 as high precision quality.

The irregularity of optical surfaces is a term used to determine how much the surface form deviates from the reference surface form. The regularity measured with an interferometer or test plate refers to the sphericity of the circular fringes, which are the interference patterns of the reference and measured surfaces.

Surface roughness, unlike surface irregularity, is a parameter used to specify small-scale irregularities of the optical surface. The roughness is formed during surface polishing process in the optical production. Since rough surfaces are susceptible to rapid wear, they are prone to forming small cracks or imperfections. Therefore, it is a parameter to be considered for applications such as laser. Standard manufacturing tolerances for surface roughness are rated at 50 Å RMS for typical grade, 20 Å RMS for precision grade, and 5 Å RMS for high precision grade. For the multi-pass matrix optical system, this value is determined as 20 Å [56].

2.3 Production of the Optical System

Since the ray trace simulation obtained from Zemax OpticStudio software provides sufficient results and minimum loss, the final specifications given in the Table 9 are

determined for manufacturing. The optics were produced in Worldhawk Optics (China).

The photographs of the multi-pass optical system, the production processes of which have been completed and ready for use, taken in the Photonics Technologies and Spectroscopy Laboratory are given in Figure 41.

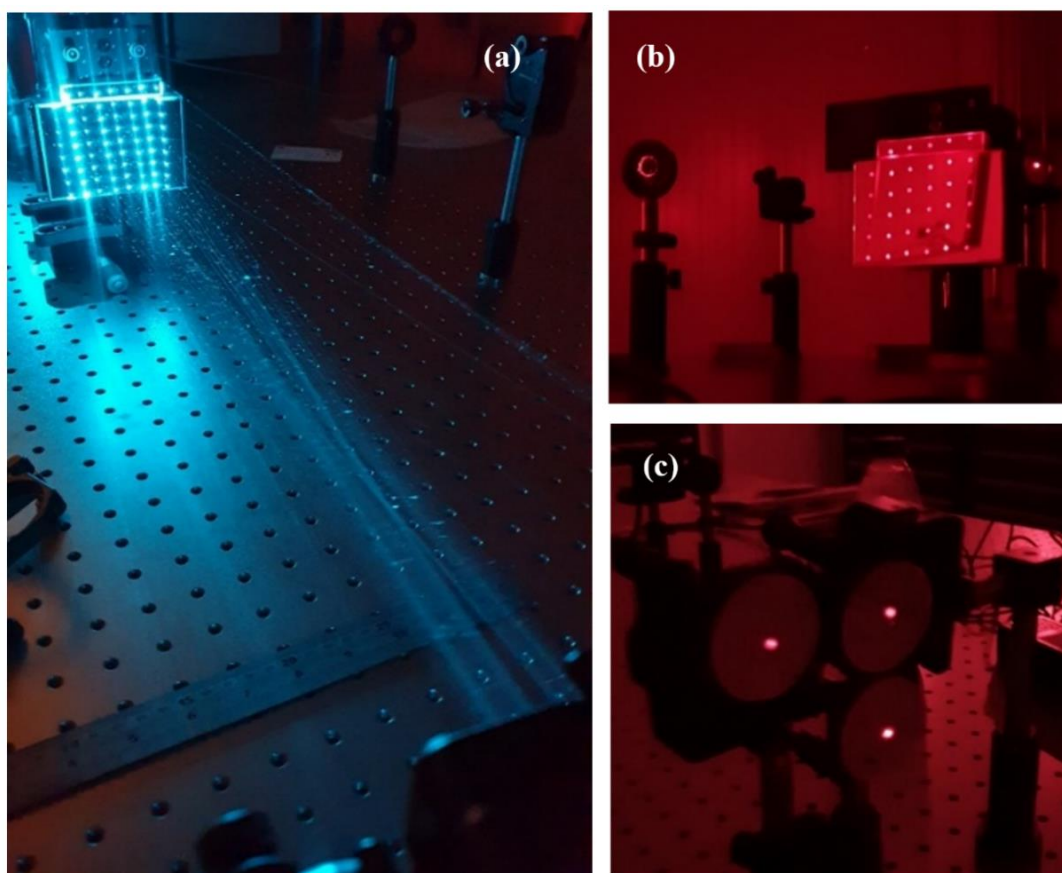


Figure 41 Photographs of the multi-pass matrix optical system in operation in different number of passes configurations. (a) and (b) field mirror group. (c) objective mirror group.

2.3.1 Materials of the Optics

Since the final tests will be carried out in the atmospheric trace gas measurement system, the mirrors must be resistant to extreme temperature conditions ranging from

-100 °C to +100 °C. Therefore, all optics inside the chamber are made of Zerodur [57] with a thermal expansion coefficient of $0.05 \pm 0.10 \times 10^{-6} / \text{K}$ from 20 °C to 300 °C.

Zerodur which is a homogeneous, inorganic, non-porous lithium aluminum silicon oxide glass ceramic, has high strength and small defect rate compared to other optical glasses. However, since the optics that will be outside the atmospheric trace gas simulation system are not exposed to extreme conditions, fused silica was chosen as the raw material for it.

Table 10 Specifications of silver and gold coating.

<i>Type of coating</i>	<i>Wavelength Range</i>	<i>Reflection Specifications</i>	<i>Typical Energy Density Limit</i>
Protected Silver	450-2000 nm 2000-10000 nm	$R_{\text{avg}} > 98\%$ $R_{\text{avg}} > 98\%$	0.5 J/cm ² @ 532nm & 1064nm, 10ns
Ultrafast Enhanced Silver	600-1000 nm	$R_{\text{avg}} > 96\%$	0.3 J/cm ² @ 532nm & 1064nm, 10ns
Protected Gold	700-2000 nm 2000-10000 nm	$R_{\text{avg}} > 96\%$ $R_{\text{avg}} > 96\%$	0.8 J/cm ² @ 1064nm, 10ns
Bare Gold	700-800 nm 800-20000 nm 2000-12000 nm	$R_{\text{avg}} > 94\%$ $R_{\text{avg}} > 97\%$ $R_{\text{avg}} > 98\%$	

Silver and gold coating options were evaluated for the multi-pass optical system, especially due to their high reflectivity in the infrared region. Although silver coating

has a harder structure than gold coating, gold shows better durability. In addition, since silver coating is six times more economical and has slightly higher reflectivity than gold coating, optics were coated with silver. The reflectivity provided by silver coating is more than 98% in the 2 μm to 12 μm spectral range required for trace gas atmospheric spectroscopy studies.

The typical energy density limit given in the Table 10 refers to the laser damage threshold, giving the maximum amount of laser power per area that a surface can withstand before being damaged. This is a very important material property for multi-pass mirror optics because the laser beams will fall on the same point of the mirror in the specified number of passes configuration, and it will cause damage on the mirror over time. For example, the energy density limit given in the table below means that the silver mirror can withstand energy densities of 0.5 J per square centimeter for 10 nanoseconds at wavelengths of 532 nm and 1064 nm.

Although silver comes to the fore with its high reflective feature, it is a structurally problematic material to manufacture and protect. Even though, silver has a very stable structure as a bulk, when it is produced as a thin film, it deteriorates very quickly and becomes unstable. For this reason, it is never coated in bare form, it must be coated as protected or enhanced to strengthen the structure. If the silver coating is not protected, it starts to deteriorate as soon as it interacts with the atmosphere after coating process in vacuum environment.

Figure 42 gives Stereo and Nomarski microscope measurements of surface of multi-pass mirrors from different points. The coatings were examined with microscopes approximately 6 months after they were produced. According to the investigations, the coating tends to deteriorate as a result of oxidation. The tendency of deterioration in areas with scratches and mirror edges is higher than in other regions.

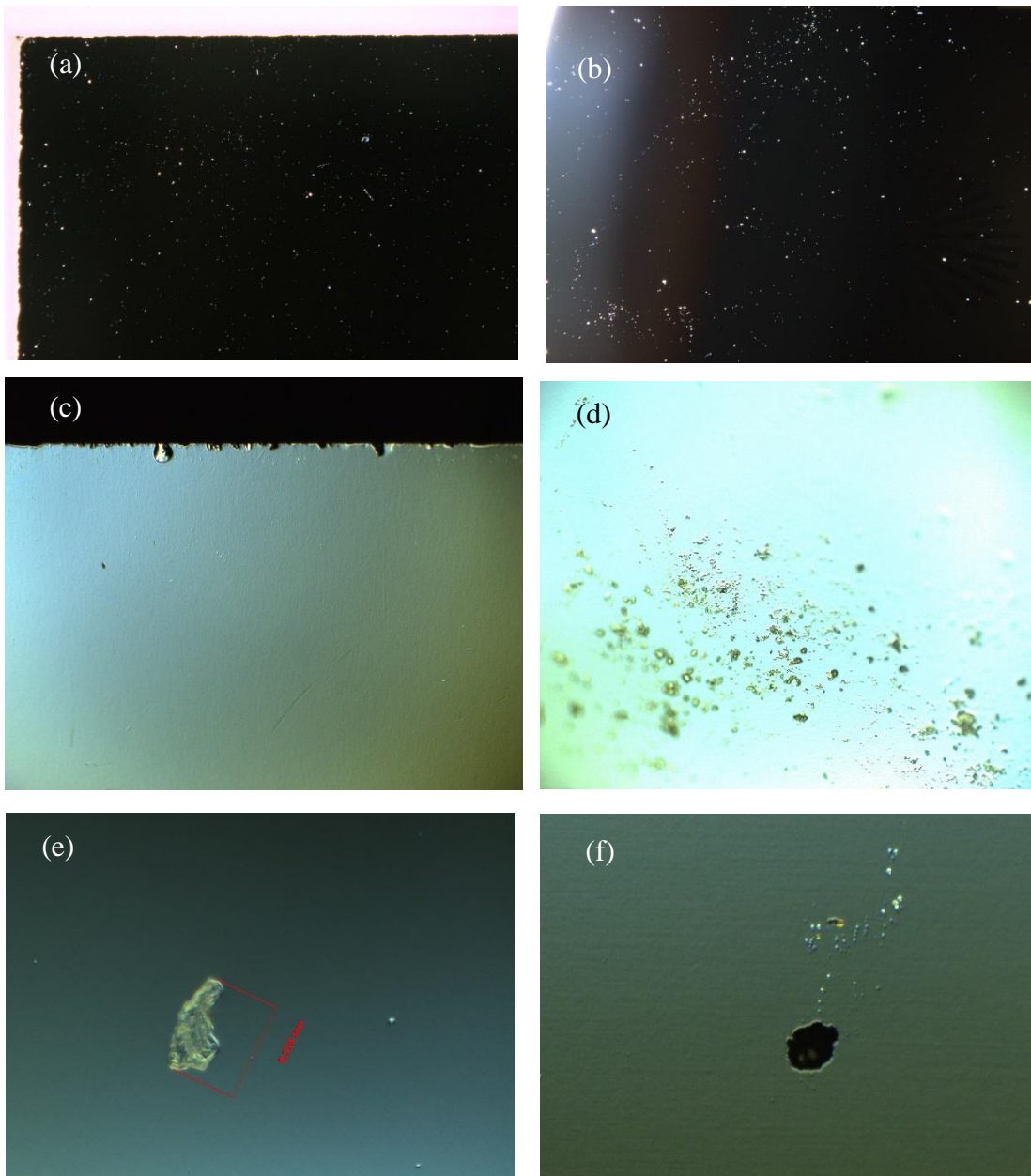


Figure 42 Microscope measurements of multi-pass matrix optics. (a) Left edge of mirror T_1 , 10x magnification, Stereo microscope. (b) Edge of O_1 , 10x magnification, Stereo microscope. (c) Top edge of T_1 , 5x magnification, Nomarski microscope. (d) Middle of T_1 , 5x magnification, Nomarski microscope. (e) A scratch on O_1 , 50x magnification, Nomarski microscope. (f) T_2 , 5x magnification, Nomarski microscope.

The reflectivity of silver coating was measured with The Agilent Cary 7000 universal measurement spectrophotometer (UMS) from 6° and 45° degrees. Reflectivity measurements could not be measured directly by the original mirrors due to the geometry of the optics. For this reason, measurements were made on a 1-inch flat dummy surface coated in the same coating chamber with multi-pass optics. Figure 43 indicates the reflectivity vs wavelength graph of protected silver coating for 6° and 45° angles. According to the graph, between 400 and 2400 nm which cover UV-VIS-NIR spectra, the average reflectivity is above 98% as expected.

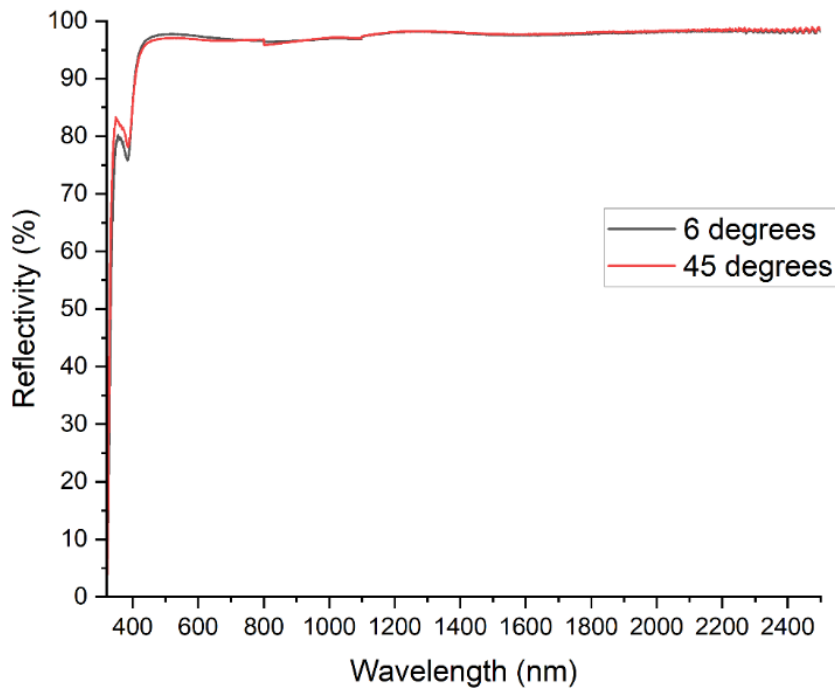


Figure 43 Reflectivity vs wavelength graph of protected silver coating of multi-pass mirror matrix system from 300 nm to 2500 nm spectral range.

In order for silver to reach this reflectivity value, it needs to be coated on the surface by 100-200 nm, but after these thicknesses, maximum reflectivity has been reached, and it does not make sense to coat more. However, silver cannot be directly coated on optical surfaces due to its atomic structure. For this reason, it should be coated

with an intermediate material called "magic layer" or "adhesion layer" about a few nm between the silver coating and the optical surface.

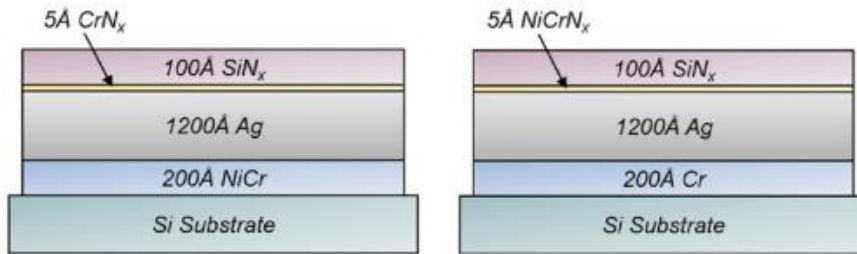


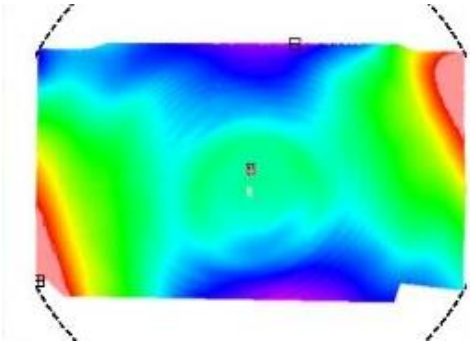
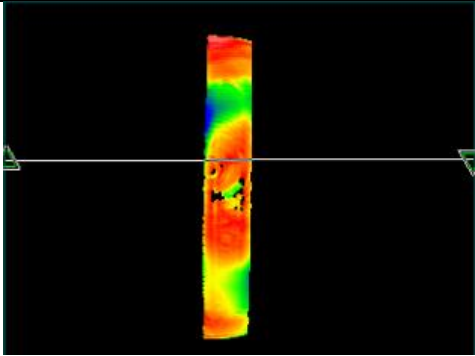
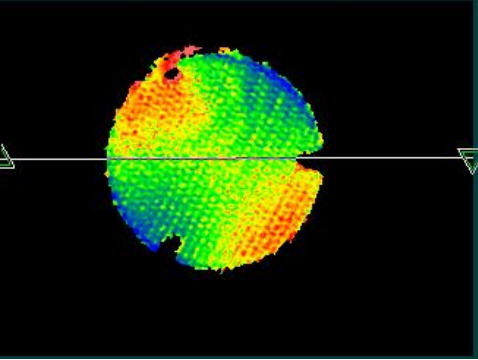
Figure 44 The layers and thicknesses given as an example of silver coating [58].

After the reflectivity measurements of the optics supplied from Worldhawk company were made, surface characterizations and radius of curvature measurements were also carried out with the Zygo test-plate. Test plates are used as reference for testing surface flatness, strength, irregularity and radius of curvature. The transparent test plate used as a reference is placed on a polished surface and flatness is verified. Two surfaces in contact are illuminated using a monochromatic light and an estimation of the surface morphology is made based on the fringes formed on the test plate. The analysis of the surface is determined by the number and irregularity of the fringes in the formed fringe map. It is an effective method to determine whether the required values such as irregularity and roughness are met at every stage of optical production. In this way, optical manufacturers determine whether the surface needs more polishing.

Automatic polishing benches are required for form correction in order to reduce surface irregularities on optical surfaces to ratios such as $\lambda/8$. Although it is more possible to obtain low irregularity in the middle of the optical surface in conventional polishing, it is difficult to obtain these values due to distortions towards the edges of the optics. Therefore, 1λ irregularity is considered typical quality, $\lambda/4$ irregularity precision, and $\lambda/20$ high precision. A fringe corresponds to $1/2$ of a wave.

Table 8 shows the surface morphology and analysis of multi-pass matrix optics. According to the surface characterization results, all surface properties and especially the irregularity (PV) and roughness (RMS) values were quite outside the expected values.

Table 11 Surface map of multi-pass matrix optics with surface irregularity (PV) and roughness (RMS) values.

	<i>Surface Map</i>	<i>Analysis</i>				
T ₁ Field Mirror		<table border="1"> <thead> <tr> <th><i>PV</i></th> <th><i>RMS</i></th> </tr> </thead> <tbody> <tr> <td>2.3469 fr</td> <td>0.3577 fr</td> </tr> </tbody> </table>	<i>PV</i>	<i>RMS</i>	2.3469 fr	0.3577 fr
<i>PV</i>	<i>RMS</i>					
2.3469 fr	0.3577 fr					
T ₂ Field Mirror		<table border="1"> <thead> <tr> <th><i>PV</i></th> <th><i>RMS</i></th> </tr> </thead> <tbody> <tr> <td>0.978 fr</td> <td>0.144 fr</td> </tr> </tbody> </table>	<i>PV</i>	<i>RMS</i>	0.978 fr	0.144 fr
<i>PV</i>	<i>RMS</i>					
0.978 fr	0.144 fr					
C ₁ Objective Mirror		<table border="1"> <thead> <tr> <th><i>PV</i></th> <th><i>RMS</i></th> </tr> </thead> <tbody> <tr> <td>1.005 fr</td> <td>0.134 fr</td> </tr> </tbody> </table>	<i>PV</i>	<i>RMS</i>	1.005 fr	0.134 fr
<i>PV</i>	<i>RMS</i>					
1.005 fr	0.134 fr					

The centering, surface quality and the amount of tilt could not be investigated due to lack of characterization instruments. Table 9 gives the specifications of multi-pass matrix optics after fabrication.

Table 12 Specifications of the optics of multi-pass matrix system after manufacturing.

<i>Specification</i>	<i>T₁</i>	<i>T₂</i>	<i>O₁, O₂, O₃</i>
Radius of curvature	598.516	599.235	600.898
Dimension	112 mm x 78 mm	78 mm x 14 mm	50.8 mm
Surface quality	-	-	-
Surface roughness	0.3577 fr	0.144 fr	0.134 fr
Clear aperture	108 mm x 74 mm	74 mm x 10 mm	46.8 mm
Irregularity (P-V)	2.3469 fr	0.978 fr	1.005 fr
Tilt	-	-	-
Material	Zerodur	Zerodur	Zerodur
Center Thickness	15 mm	15 mm	4 mm

2.3.2 Optomechanical Mounts

All the optomechanical mountings are provided by Thorlabs and Edmund Optics for tabletop prototype. The ultimate mounts will be designed by considering the conditions such as extreme temperature and pressure required for the atmospheric trace gas spectroscopy. However, the material of purchased optomechanics was chosen to be high vacuum compatible until 10^{-9} Torr and operable between -30 °C

and 100 °C temperatures. The provided optomechanics are 2 inches kinematic mirror mounts, plates for attaching field mirrors, kinematic holders to which the plates are fixed, linear stage to adjust focal point, and common tools such as posts, post holders and clamping forks.

Due to the non-standard geometry of the field mirrors, it was not possible to find ready-made optical holders. For this reason, a vacuum-operable plate was selected in accordance with the dimensions of the mirrors and attached with the help of an adhesive suitable for vacuum applications. In order for the system to work in different pass number configurations, it should be tilted at different degrees specific to each pass number. For this reason, the attached plate is fixed to another kinematic holder, which can be tilted in 3 axes, with the help of posts.

The bonding process was done very carefully in order not to deteriorate the wave front properties of the optics. As the system does not need imaging, wave front distortions are of little importance for spectroscopy measurements, but for other applications this bonding method is not suitable at all. Below are the surface characterization measurements of one of the optics before and after bonding.

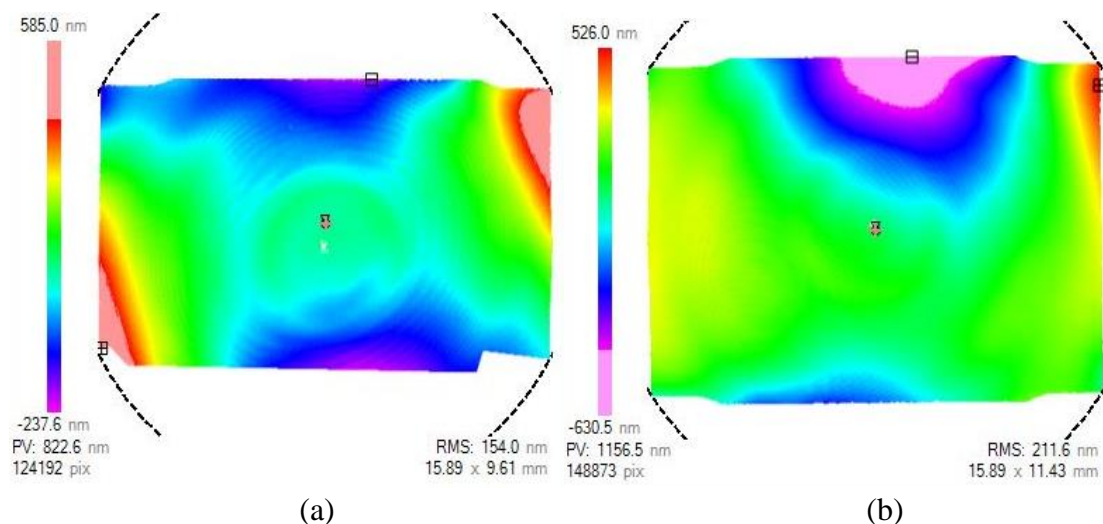


Figure 45 Surface maps of field mirror T₁ before bonding (a) and after bonding (b).

Table 13 PV and RMS values of surface of T₁ before and after bonding process.

<i>Measurement</i>	<i>PV</i>	<i>RMS</i>
Before bonding	2.3469 fr	0.3577 fr
After bonding	3.0927 fr	0.5129 fr

As a result of bonding the mirror T₁ to the plate, a serious decrease is observed in the irregularity (PV) and roughness (RMS) of the surface.

CHAPTER 3

EXPERIMENTAL RESULTS AND PERFORMANCE ANALYSIS

In the Chapter 3, the mathematical model, experimental setup and performance studies of the multi-pass matrix optical system, whose design, ray trace simulation, aberration analysis, production and post-production surface characterization have been completed, are explained. The performance of this system, whose ultimate purpose is atmospheric trace gas spectroscopy, is achieved by extinction spectroscopy of molecular absorber and scattering microparticle in a quartz absorption cuvette placed between two mirror groups on the optical path in an open atmosphere environment.

Measurements of different concentrations of molecules and microparticles in the liquid solvent were carried out at an optimally determined number of passes provided by the optical system. In addition, for the molecular absorber, measurements were taken and analyzed with different transition numbers at constant concentration. The performance of the optical system was evaluated in terms of the detection limit (LoD), which is the lowest concentration of molecules and scattering microparticles that can be detected by the system. Moreover, the extinction coefficients for the crystal violet molecule were calculated and compared with the literature.

3.1 Instruments and Experimental Setup

Both the measurements of molecular absorber and scattering microparticle were done in almost the same experimental setup whose schematic and 3D representation is given in Figure 46 and Figure 47.

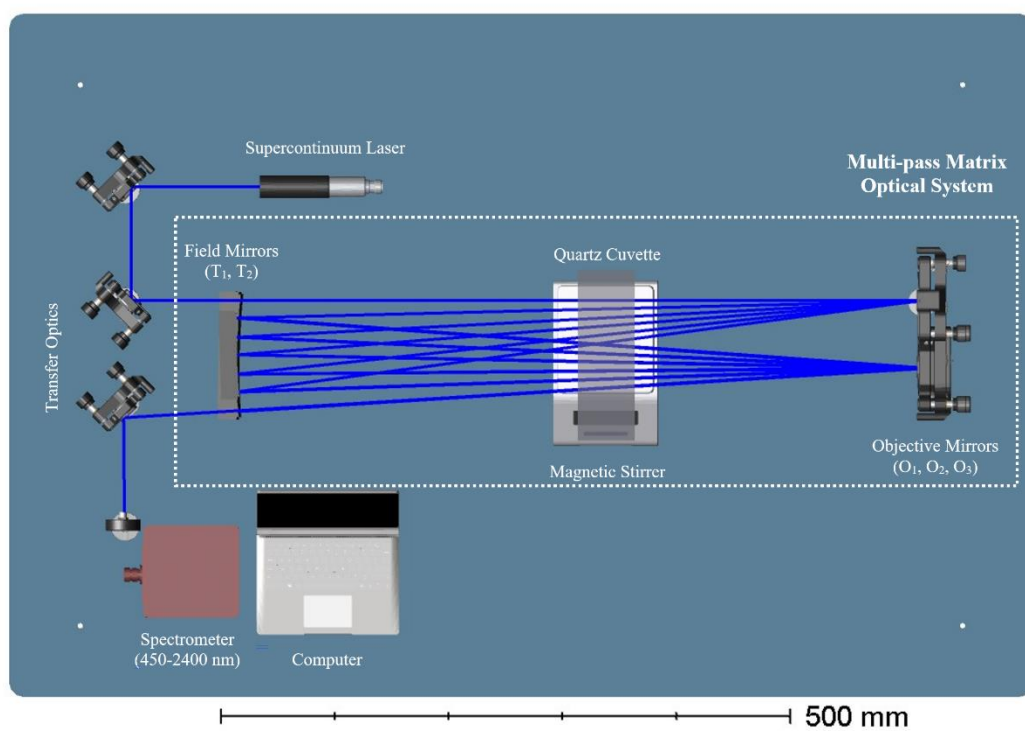


Figure 46 Schematic representation of experimental setup.

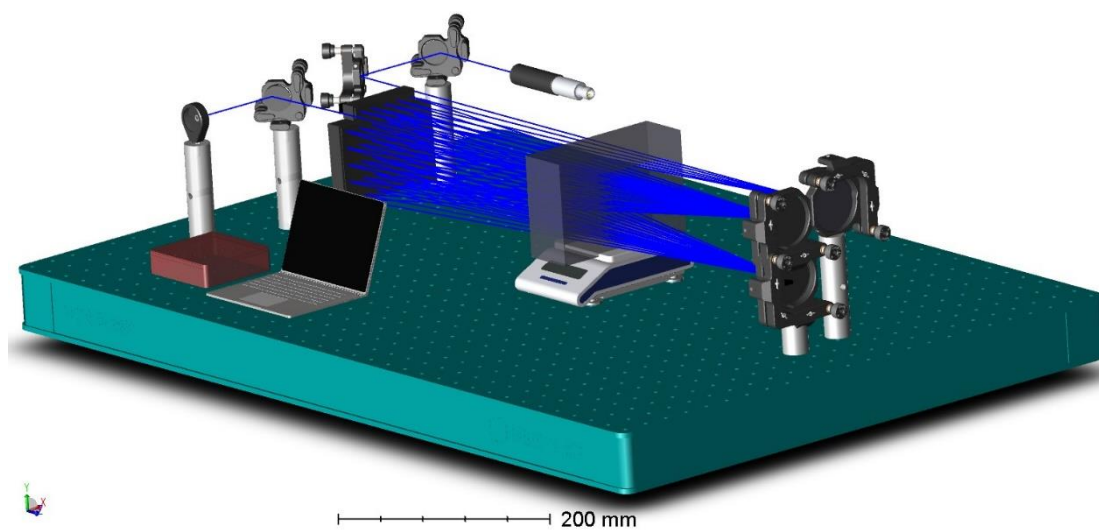


Figure 47 3D representation of experimental setup.

In the experiment since it is aimed to measure the visible spectrum of the molecules and scattering microparticles in broadband range, a supercontinuum white light laser (SuperK Compact, NKT Photonics, Denmark) is used. The total power of the laser, which gives diffraction limited light between 450-2500 nm wavelengths, is 110 mW, and its power between 450-850 nm wavelengths is around 20 mW. However, the laser was never used at maximum power during the experiments, and it was generally operated at around 50% of power. The collimated beam diameter of the laser is approximately 1 mm at 530 nm wavelength. Other optical properties of the supercontinuum laser can be found in Appendix A.

All optics that transfer the laser beam to the multi-pass matrix optical system are coated with protected silver to minimize the power loss of the laser light. Due to molecular absorbers active in the IR range, the distance between the transfer optics is kept as short as possible in the case of measurements in the infrared spectrum with this system.

For the extinction spectroscopy experiments, a large absorption cuvette was purchased from Hellma Analytics. The cuvette was chosen to be large enough to cover all rays passing through the multi-pass mirror system and to be transparent to visible wavelengths. The specifications of the cuvette are given in the table below:

Table 14 General properties of absorption cuvette [59].

<i>Cuvette</i>	<i>Volume</i>	<i>Size</i>	<i>Wavelength</i>	<i>Pathlength</i>	<i>Material</i>	<i>Refractive Index</i>
Hellma 700-061-10	600000 μ l	143 x 3.5 x 50 mm^3	Visible (360 - 2500 nm)	50 mm	Quartz	1,544

A magnetic stirrer was placed at the bottom of the cuvette so that the scattering microparticles were aggregated as little as possible and suspended in the liquid

solvent. The mixing speed was determined in such a way that the microplastics were homogeneously spread in the liquid solvent and did not create vortex. The same speed was used for all experiments.

The extinction spectrum of the molecules and microparticles were observed with VIS Spectrometer (Maya, Ocean Optics, USA). The wavelength range of the spectrometer is 450-2000 nm, the spectral resolution is 0.18 nm FWHM and integration time is 7.2 ms – 5 s.

3.2 Trace Detection of a Molecular Absorber

In a multi-pass matrix optical system with a cuvette filled with an absorber molecule in its optical path, the transmissivity of the molecules can be represented by a mathematical model.

In the Figure 48, one round trip of the incident beam of light inside the multi-pass matrix optical system is represented. The numbers 1, 6, 8 and 13 show the air environment; 2, 5, 9 and 12 indicate the air-quartz interface; 3, 4, 10 and 11 illustrate the quartz-water interface; 7 and 14 show the air and multi-pass mirror interface.

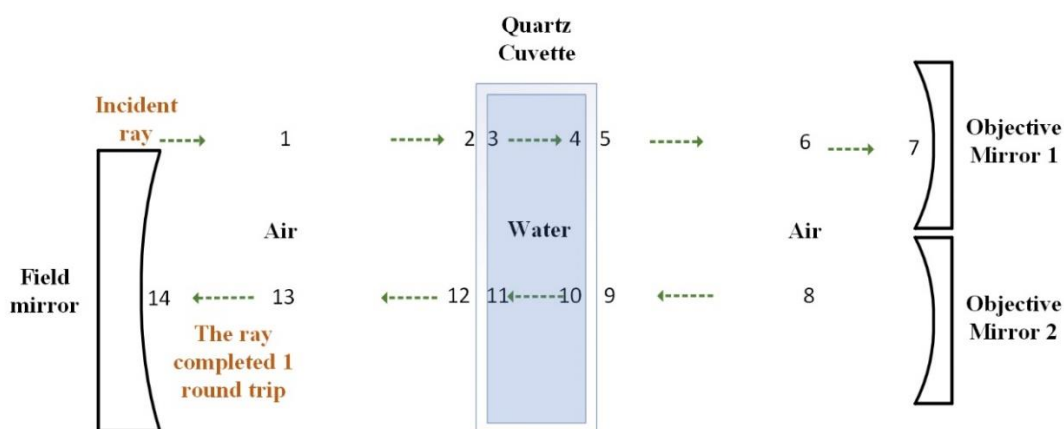


Figure 48 A round trip of ray of light inside the multi-pass matrix optical system.

In the experiment the reference measurements were done with a cuvette filled with distilled water. Therefore, the reference intensity value after one round trip can be written as following:

$$\prod_{i=1}^n I_0 (1 - R_{q_{11}})(1 - R_{q_{21}})(1 - R_{q_{12}})(1 - R_{q_{22}})(1 - R_{O_1})(1 - R_{T_2}) e^{-2\sigma_a l_1} e^{-4\sigma_q d} e^{-2\sigma_w l} e^{-2\sigma_a l_2} \quad (17)$$

$$n = a \times b \quad (18)$$

where, n is half of number of passes which is equal to multiplication of number of rows (a) and number of columns (b) on the field mirrors, I_0 is the incident ray of light, $R_{q_{11}}$ is the reflectivity of the first surface of the first wall of quartz cuvette, $R_{q_{21}}$ is reflectivity of first surface of the second wall of quartz, $R_{q_{12}}$ is reflectivity of second surface of first wall of quartz, $R_{q_{22}}$ is reflectivity of second surface of second wall of quartz, R_{O_1} is the reflectivity of the mirror O_1 , R_{T_2} is the reflectivity of the mirror T_2 , σ_a is the extinction coefficient of air, σ_q is the extinction coefficient of quartz, σ_w is the extinction coefficient of water, l_1 is the approximate distance between field mirrors and quartz cuvette, d is the thickness of the walls of quartz cuvette, l is the effective width of the quartz cuvette, l_2 is the approximate distance between objective mirrors and quartz cuvette.

If the reflectivity of the walls of the quartz cuvette and the reflectivity of the multi-pass mirrors are assumed to be the same, the equation 17 can be expressed as,

$$I_{ref} = \prod_{i=1}^n I_0 (1 - R_q)^4 (1 - R_{mp})^2 e^{-2\sigma_a l_1} e^{-4\sigma_q d} e^{-2\sigma_w l} e^{-2\sigma_a l_2} \quad (19)$$

where R_{mp} is the reflectivity of multi-pass optics, R_q is the reflectivity of quartz cuvette. When the cuvette is filled with the absorbance material, one round trip of the beam of light can be written as:

$$I = \prod_{i=2}^n I_0 (1 - R_q)^4 (1 - R_{mp})^2 e^{-2\sigma_a l_1} e^{-4\sigma_q d} e^{-2\sigma_w l} e^{-2\sigma_A c_A l} e^{-2\sigma_a l_2} \quad (20)$$

$$\sigma_{Extinction} = \sigma_{Absorption} + \sigma_{Scattering} \quad (21)$$

where c_A is the molar concentration of molecular absorber, σ_A is the extinction coefficient of molecular absorber which is equal to the sum of absorption coefficient and scattering coefficient. Although the molecules have also Rayleigh scattering, when the light wave travels at visible wavelength, it is considered as negligible. Therefore, the extinction coefficient of molecular absorber can be assumed as absorption coefficient for this case. The ratio of Equation 20 to Equation 19 gives the transmission of the molecular absorber inside the cuvette:

$$\frac{I}{I_{ref}} = \frac{\prod_{i=1}^n I_0 (1 - R_q)^4 (1 - R_{mp})^2 e^{-2\sigma_a l_1} e^{-4\sigma_q d} e^{-2\sigma_w l} e^{-2\sigma_A c_A l} e^{-2\sigma_a l_2}}{\prod_{i=1}^n I_0 (1 - R_q)^4 (1 - R_{mp})^2 e^{-2\sigma_a l_1} e^{-4\sigma_q d} e^{-2\sigma_w l} e^{-2\sigma_a l_2}} \quad (22)$$

$$T = e^{-2\sigma_A c_A l} \quad (23)$$

Since the light passes through the multi-pass system at least two times, the transmission of the light is calculated as in Equation 23. According to Beer Lambert's law, the absorption (A) can be found as:

$$A = -\log T \quad (24)$$

Experiments were carried out using crystal violet molecule in water solution as molecular absorber. CV purchased from Sigma-Aldrich was of analytical grade and used without further purification. All solutions were prepared using 17.2 M Ω cm ultrapure water produced by a water purification system in experimental procedures.

Figure 49 gives the experimental setup of measurement system for trace amounts of molecular absorbers.

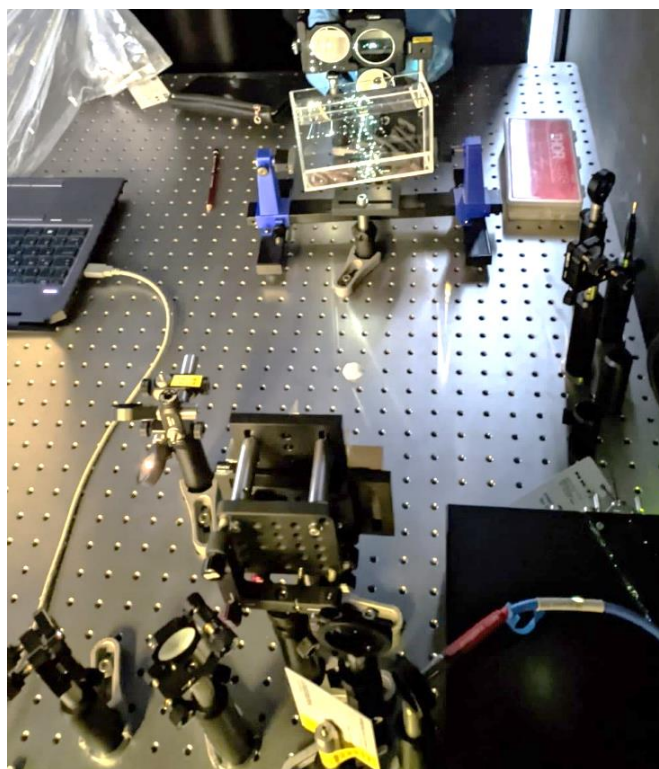


Figure 49 Photograph of the experimental setup of measurement system for trace amounts of molecular absorbers.

In the first part of the experiment, the absorption spectra were measured at different number of passes for 10^{-8} M crystal violet - water solution. According to the normalized spectra of CV, the absorption amount for different number of passes at several wavelengths were recorded and normalized absorption vs number of passes graphs are plotted as shown in the figures below:

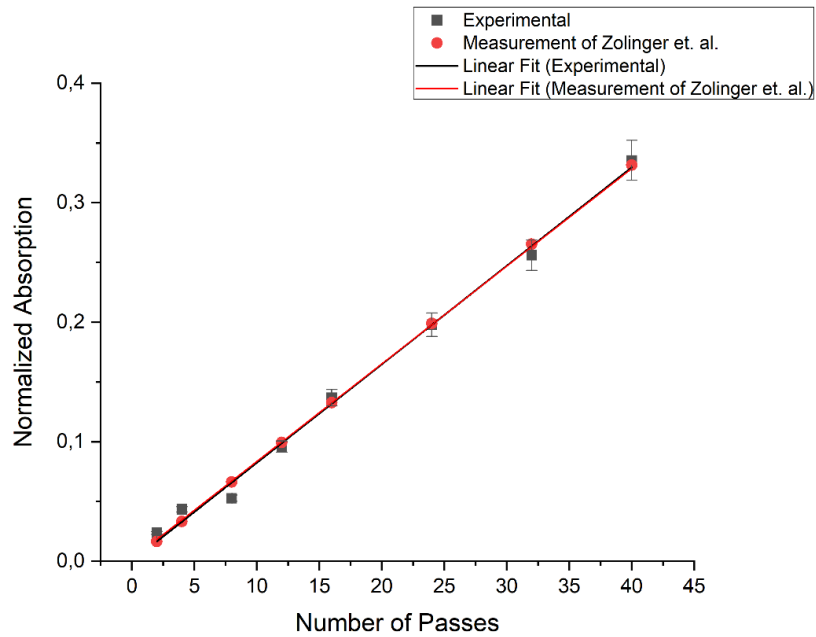


Figure 50 The normalized absorption vs number of passes graph of crystal violet with the concentration of 10^{-8} M at 509.5 nm wavelength.

The normalized absorption vs number of passes graph for crystal violet molecules with 10^{-8} M concentration at 509.5 nm wavelength were obtained from the measurements of multi-pass optical systems (black dots), and measurements of Zolinger *et. al.* [60] (red dots).

The extinction coefficient calculated by Zolinger *et. al.* was reported as $112000 \text{ cm}^{-1}/\text{M}$ at 509.5 nm. The absorption coefficient can be calculated according to Beer's law by using the slope of the graph.

$$\frac{A}{n} = \sigma cl \quad (25)$$

where A/n is equal to 0,00825; c is 10^{-8} M, l is 5 cm; then the absorption coefficient of the CV molecule at 509.5 nm is $164800 \text{ cm}^{-1}/\text{M}$.

Figure 51 and Figure 52 show the normalized absorption vs number of passes graphs of CV with 10^{-8} M at 545.2 nm and 592.0 nm respectively.

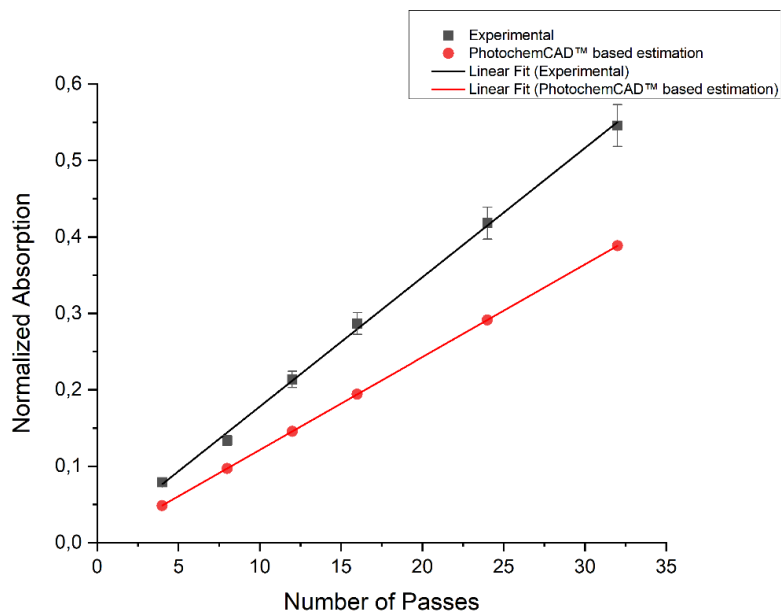


Figure 51 The normalized absorption vs number of passes graph of crystal violet with the concentration of 10^{-8} M at 545.2 nm wavelength.

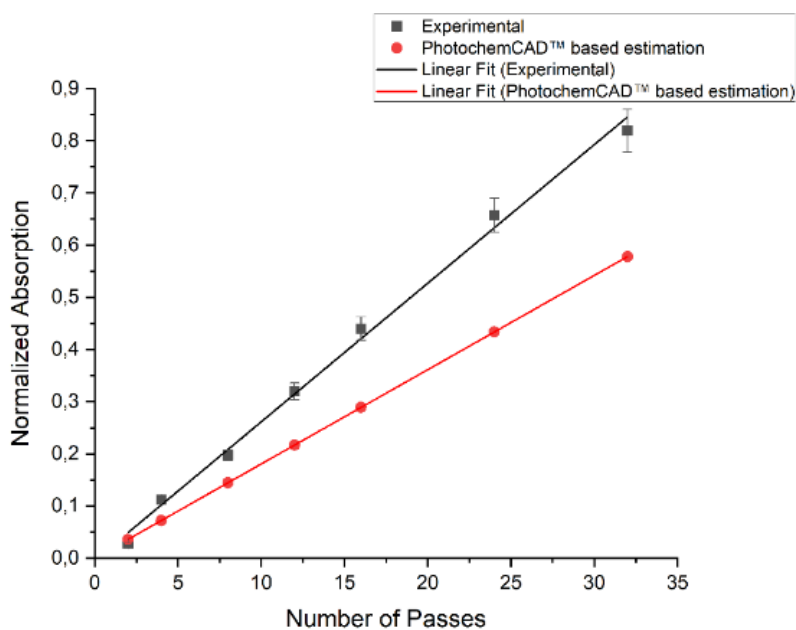


Figure 52 The normalized absorption vs number of passes graph of crystal violet with the concentration of 10^{-8} M at 592.0 nm wavelength.

In the rest of the theoretical calculations, the values of the extinction coefficients at different wavelengths are obtained from the PhotochemCAD [16] software and its database. To obtain the synthetic absorption spectra of the molecules, the database uses Lorentzian, Gaussian or Delta functions and existing spectra [61]. The database was created by interpolating the absorption spectrum for crystal violet, based on the measurement taken by Zolinger *et. al.* at 509.5 nm. Then by using the normalized absorption spectrum provided by database, the extinction coefficient was calculated for 545.2 nm and 592.0 nm which is the peak absorption wavelength of CV.

Then, absorption measurements were made at different concentrations from 10^{-7} to 2.5×10^{-9} M in order to calculate the minimum concentration at which the CV molecule could be detected by the measurement system with 32 passes. The normalized absorption spectra of the crystal violet with respect to wavelength at different concentrations is given in the Figure 53.

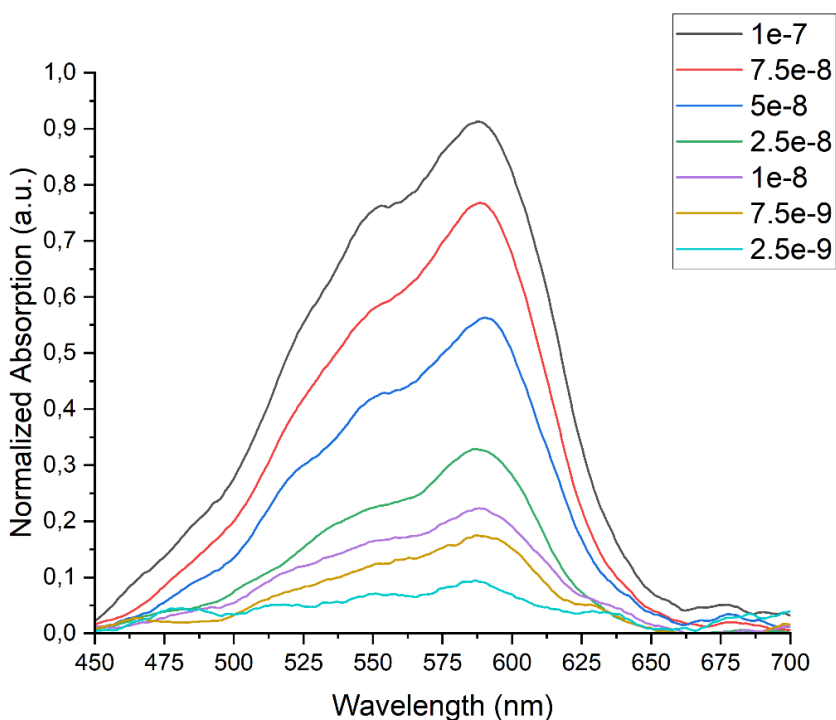


Figure 53 Normalized absorption vs wavelength graph of crystal violet for different concentrations.

3.3 Trace Detection of a Microscopic Scatterers

The amount of extinction caused by scattering microparticles also obeys Beer-Lambert's law, which is used to determine the amount of absorption caused by molecules. As expressed in Equation 21 in the previous section, the extinction coefficient is the sum of the absorption and scattering coefficients. For molecular absorbers such as CV, the absorption coefficient is more dominant, while for dielectric particles such as scattering microparticles, scattering is the main extinction factor. Practically speaking, the absorption coefficient of the scattering microparticle is almost zero. The scattering depends on the particle size and the surface roughness of the particles. However, since there is not sufficient information about the surface structure and size of the particles, in this study no scattering analysis based on these properties was performed.

In this experiment, polypropylene (PP) type microplastics used as microscattering particles were supplied from Petkim Inc. The general characteristics of the sample is given in the table below:

Table 15 Several specifications of PP type microplastics.

<i>Scattering microparticle</i>	<i>Type</i>	<i>Dimension</i>	<i>Molar Mass</i>	<i>Density</i>
Polypropylene (PP)	Primary	< 100 μm	354.6 g/mol	0.92 g/cm ³

In this experiment, the extinction spectra of microplastic particles were measured in ethanol-water medium. The reason for choosing this mixture is to ensure that PP, with an average density of 0.92 g/cm³, is suspended in the liquid medium and dispersed homogeneously in the absorption cuvette. The mixture was obtained by taking 30% of ethanol with a density of 0.789 g/cm³ and 70% of water with a density of 0.997 g/cm³. The density of the mixture obtained was determined as approximately 0.934 g/cm³ which allows the particles were homogeneously

dispersed since it was almost equal to the density of PP. In addition, the cuvette is additionally placed on a magnetic stirrer so that the multi-pass laser beam can encounter an equal amount of particles at every point it passes through the cuvette.

Figure 54 gives the experimental setup of measurement system for scattering microparticles.

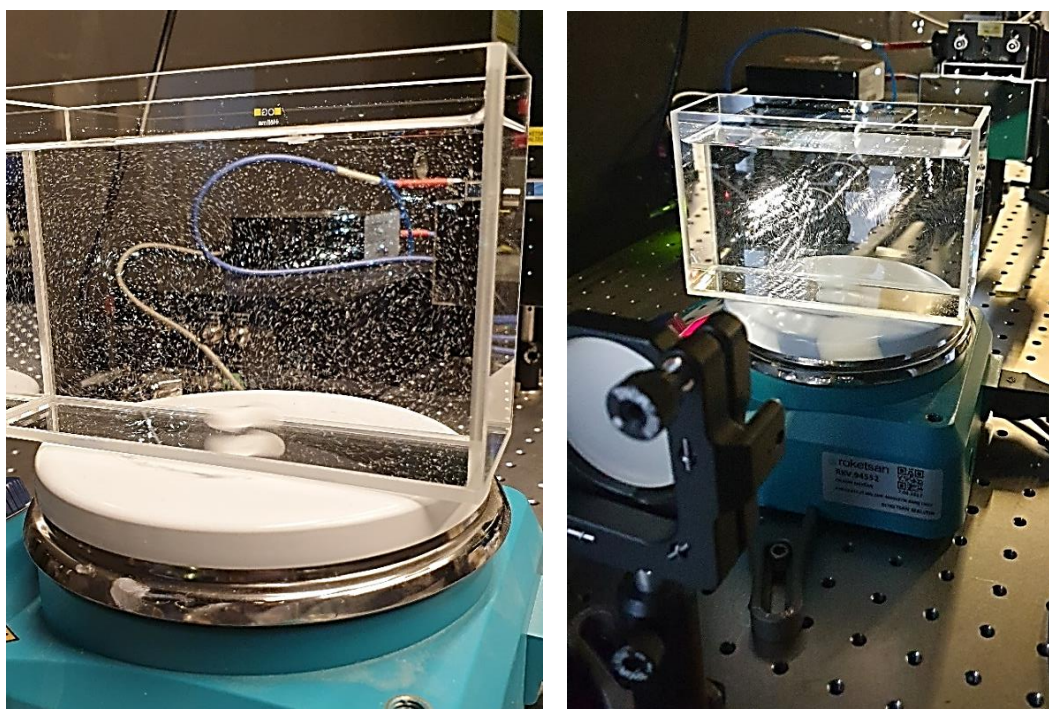


Figure 54 Photographs of PP type microplastics inside the cuvette.

The extinction spectra measurements of microplastics were carried out in 12 different masses ranging from 0.001 grams to 0.1 grams. The molarity of the microparticles in the water-ethanol mixture was calculated according to the masses to be used in the experiment.

The extinction measurements were made at different concentrations from 4.7×10^{-4} to 4.7×10^{-6} M in order to calculate the minimum concentration at which PP could be detected by the measurement system with 32 passes. The normalized extinction

spectra of the polypropylene with respect to wavelength at different concentrations is given in the Figure 55.

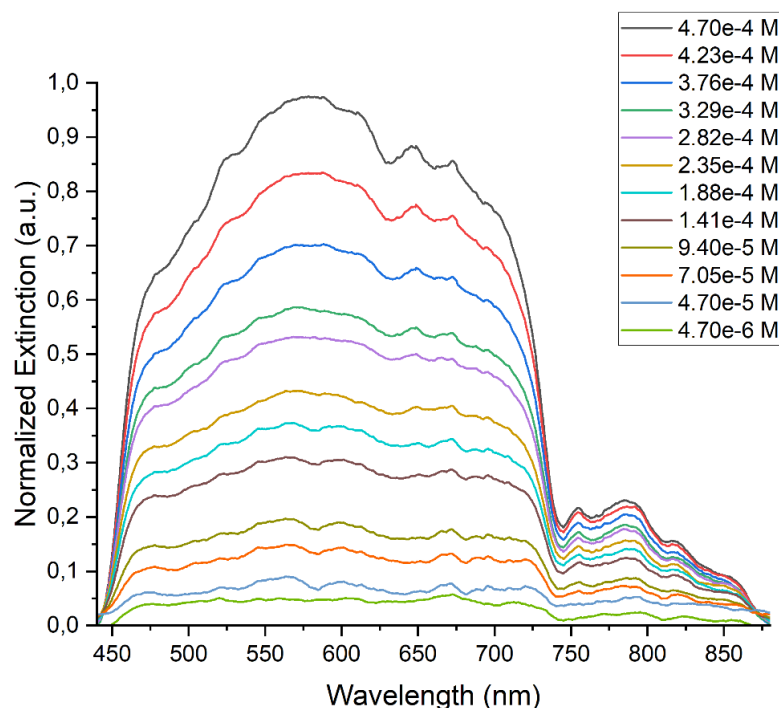


Figure 55 Normalized extinction vs wavelength graph of PP type microplastics according to different concentrations.

3.4 Limit of Detections

Limit of detections (LoD) can be defined as the lowest concentration or amount of analyte in the test sample which can be reliably distinguished from zero [62].

To determine the lowest detectable concentration of both crystal violet and polypropylene, the concentrations mentioned in the previous sections were individually prepared. In order to increase the measurement reliability; the location of the instruments, including the fiber cable of the spectrometer, the transfer mirrors, the mirrors of the multi-pass optical system, was not changed according to the

initially installed configuration. In order to be able to change the concentrations required for the measurements, the cuvette was removed each time to prepare for the next experiment. However, great care was taken to put it back in place at the same angle and position.

Reference measurements prepared with a water-filled cuvette for a CV and a water-ethanol-filled cuvette for MP were repeated in both different concentration measurement experiments. Since it was observed that the reference measurements were compatible with each other, the experiment was completed by taking safe measurements.

The lowest detectable concentration was obtained from the extinction spectra measured at different concentrations for both molecules and the microplastics. To find the average absorption amount of CV, an integer was obtained by calculating the integral of each curve corresponding to the spectra at different concentrations in the 450-650 nm spectral range and dividing by the total wavelength. For microplastic measurements, similar calculations were made by considering the spectral range of 450-840 nm. Noise were recorded several times in an environment where the spectrometer could not receive signals from anywhere. The baseline was calculated by considering the noise of the spectrometer and the instability of the laser. By taking the standard deviation of the noise measurements, the baseline was determined.

Baseline and spectrally averaged extinction amounts were plotted on the same graph, and the intersection points determined as the lowest detection limit were taken. The lowest detection amount for CV was measured as 2.5×10^{-9} M, while for PP type microplastics it was measured as 1.68×10^{-5} M.

CHAPTER 4

DISCUSSION & CONCLUSION

In this thesis; the design, production and performance analysis of a Chernin cell based multi-pass matrix optical system intended for atmospheric trace gas spectroscopy are presented. According to the simulation analysis carried out with Zemax OpticStudio Software, zero geometric loss, ignorable astigmatism, preserved focal properties compared to original White cell design and small off-axis angles are accomplished. Then the system was constructed according to the design parameters and tolerance analysis obtained from simulation results. The performance analysis were achieved by performing extinction spectroscopy of CV and PP in a optical cuvette large enough to cover the area the light rays cycling inside the cavity formed by the objective and field mirrors. Finally, the limit of detection values for both molecular absorber and scattering microparticle were calculated from spectrally averaged extinction vs concentration graphs.

The multi-pass matrix optical system is not an imaging system. Therefore, the distortion of the waveform of the laser beam, which passes through the cavity between the mirrors many times, does not affect the system performance. The most important thing in the spectroscopy studies carried out is that the amount of photons falling on the detector does not decrease due to optical design reasons. For this reason, it is aimed to have zero geometric loss with the right design parameters.

The second condition evaluated from the analysis studies is that the wavelengths contained in the supercontinuum white light laser source used, do not suffer from chromatic aberration at the system output. For this reason, geometrical and RMS deviations of different wavelengths were evaluated on the detector located at the exit aperture of the multi-pass matrix optical system. As a result of the analysis, it was

evaluated that the geometrical loss and the chromatic aberration was negligible for spectroscopy studies.

The ultimate purpose in this study is to reduce the limit of detection of the measurement as much as possible by detecting trace amounts of sample in liquid solution or atmospheric gas environment with high sensitivity and accuracy. According to the working principle of the system, this is possible by increasing the optical path through which the light passes. Since the optical path extension will cause the sample to be measured to be exposed to more light, more absorption will occur. In this way, measurement can be performed above the detection limit of the detector. One way to extend the optical path is to increase the inter-mirror cavity length. To accommodate, this approach will require increasing the radius of curvature of the mirrors. However, increasing the radii of curvature too much makes the optical system susceptible to aberrations. During the production phase of the optics, while the optical surfaces are lapped, measurements must be made with a test plate or interferometer at every stage to control the radius of curvature and surface irregularities. Since the optics must be placed at the focal point during the measurement, a special test plate would be required for optics with a very large radii of curvature. Surface characterizations would not be possible with a standard test plate, thus the production would become technically challenging and the cost would dramatically increase. During the design phase of multi-pass matrix optical system, initially the radius of curvature was determined as 1000 mm, it had to be changed to 600 mm for aforementioned reasons. Ultimately for industrial applications, it is best practice to discuss with optical production engineers whether the system can be produced or not during the design process.

A second way to extend the optical path is to increase the number of rows and columns on the field mirror. This is only possible either by using a larger mirror with the same beam diameter or by using a smaller laser beam diameter using the same mirror size. Since the substrate of optics is chosen to be resistant to extreme conditions such as very high temperatures, it is a material that is both difficult to supply and very expensive compared to standard optical glasses. Likewise, silver or

gold is generally preferred for high reflectivity, so the cost of coating is also high. In addition, since the weight of the optics will increase as the amount of material increases, the optomechanics must be durable enough to carry the weight of the optics; adding to cost. For these reasons, enlarging the mirrors will increase the amount of material used, the production price and weight considerably marking this solution not suitable.

As mentioned, another alternative way to lengthen the path is to reduce the diameter of the laser beam. Broadband laser sources are preferred for spectroscopy studies since they allow for faster spectroscopic scans. However in this case, standard lenses cannot be used to collimate the light or reduce the beam diameter, since each wavelength will refract at a different angle because of the wavelength dependency of refractive index of the lens, which would cause chromatic aberrations and even geometric losses. For this reason, concave and off-axis parabolic mirrors should be used to reduce and collimate the beam diameter. In any case, the extra optics used would make the optical system more complex and costly. It is also possible to reduce the diameter of the beam by limiting the light with the help of an aperture, as used in this experiment setup, to ensure that it reaches the desired dimensions. Nevertheless, in this case, the power of the light is lost to an extent. To compensate, the laser source must be able to produce light at high powers and the reflectivity of the coatings used in the multi-pass mirror system must be as high as possible.

Despite of enhancing the optical path is geometrically possible by increasing the number of beams on the field mirror, it is restricted by the amount of absorption of the mirror surfaces. As they have 98% reflectivity for between 2 and 12 μm wavelength range, 2% of power will be lost in each reflection, so when the number of passes reaches a certain point, the total absorbance of the mirrors overcomes the detectable absorption amount of the sample to be tested.

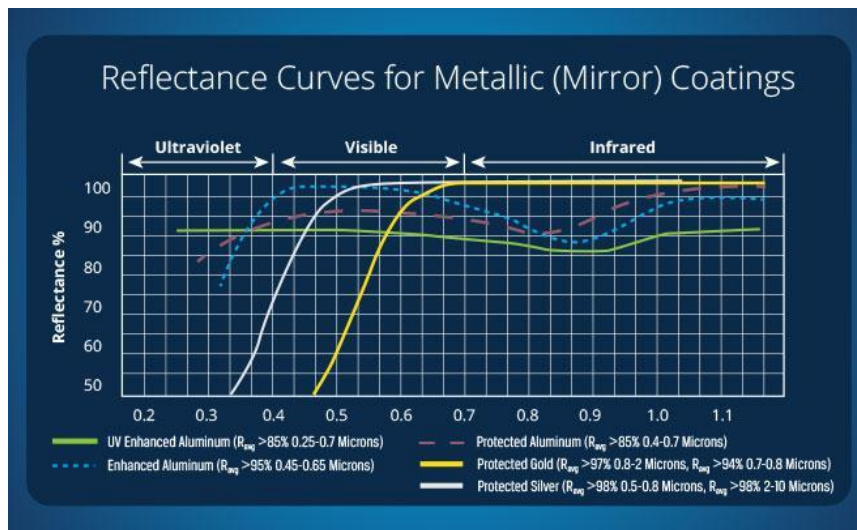


Figure 56 Reflective curves for metallic mirror coating [63].

Although the multi-pass matrix optical system is designed for 72 number of passes calculated as optimal for weak absorption lines, it is a design in which more number of passes configurations can be applied. With this system, a maximum of 288 passes can be obtained with the 12x12 matrix array, which ensures the optical path length is approximately 173 meters despite a cavity length of 0,6 meter. Maximum path length can only be achieved using coating with 98% reflectivity and supercontinuum laser source with maximum power and submillimeter beam diameter.

In atmospheric trace gas absorption studies, since the absorption bands of each gas type are of different wavelengths, the mirror coatings were chosen to provide an average reflectivity in the broadband. However, in a study where the specific absorption wavelength is determined, the number of transitions can be increased dramatically by increasing the reflectivity if a special coating is used for that wavelength.

Since the cuvette is not coated with antireflective coating, the huge amount of power is lost because of the surface reflections which limits the number of passes. For the experimental setup in this study, the optimum number of passes have been determined as 32 with 4x4 matrix array arrangement.

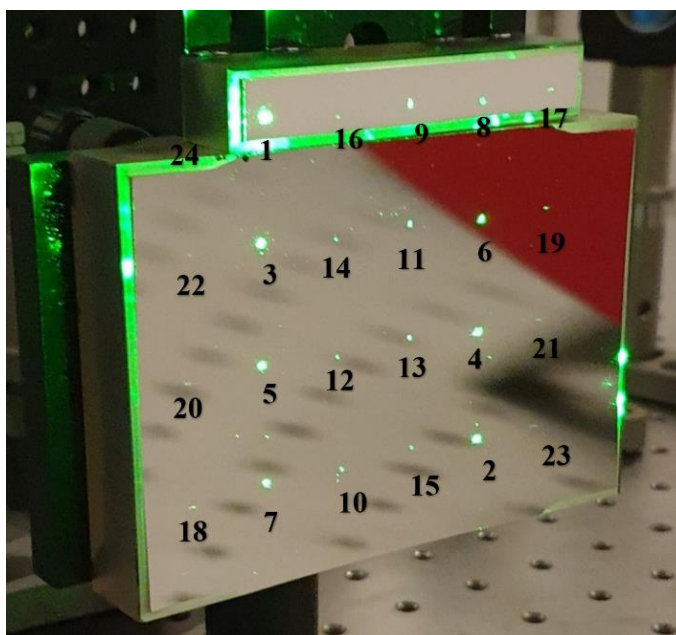


Figure 57 48 passes with 6x4 matrix arrangement. In this configuration quartz cuvette filled with water was placed in the optical path between field and objective mirrors.

Figure 57 shows 48 passage configuration with 6x4 matrix arrangement when the quartz cuvette is placed in the optical cavity between the field and objective mirror groups. Due to the back reflection from the surface of the cuvette filled with water, on the the field mirrors both original laser beams that aim to reach to the detector and back-reflected beams are shown. In this configuration, after second matrix group which starts with 17th image shown on the field mirror, although there is no absorber molecule in the cuvette yet, the laser beam loses its almost full power so that it is nearly invisible on the mirror. Therefore, it has determined experimentally that the number of passes would not exceed 32 which corresponds to 4x4 matrix arrangement.

For different number of passes configurations, molecular absorption spectrums of 10^{-8} M CV in aqueous solution have been measured. Figure 53 gives the normalized absorption vs number of passes graph. According to the graph, with the increase of the number of passes, the absorption also increases linearly, as suggested by Beer-Lambert's law.

The absorption spectrum was compared with the extinction coefficient at 509.5 nm measured by Zolinger *et. al.* [60]. This value found in the literature was obtained by the single-pass direct spectroscopy method and the graph was adapted for multi-pass configurations for comparison purposes in this application. According to the graph, the extinction coefficient of the value in the literature is $0.12 \text{ cm}^{-1}/\mu\text{M}$, which satisfies the experimental result of the multi-pass measurement technique with $0.16 \text{ cm}^{-1}/\mu\text{M}$ (Figure 58 (a)).

The error bars in Figure 58 were determined by considering the deviation of the spectrometer, the power instability of the laser and the molar concentration errors. To calculate the spectrometer error, the background measurement was taken multiple times. Then, the difference between the values calculated by taking into account the noise of the spectrometer and the values calculated without taking into account the spectrometer noise was calculated for each measurement and this was evaluated as the spectrometer error. The power instability of the laser was reported in the datasheet as 1% that can be found in Appendix A. Finally, the mass error caused by the precision scale may have caused the error in the molecule concentration.

Figure 58 (b) and (c) show the normalized absorption vs number of passes graphs of CV with the concentration of 10^{-8} M at 545.2 and 592.0 nm. Although the extinction coefficient measured by Zolinger *et. al.* for 509.5 nm wavelength coincides with the multi-pass system measurement, the extinction coefficient values obtained from multi-pass measurement do not overlap with the literature values for larger wavelengths.

The wavelength dependent extinction coefficients of CV were found in PhotochemCAD database [16] for 545.2 and 592.0 nm wavelengths. The database provides synthetic spectrum which were derived by combination of Lorentzian or Gaussian curves, present spectra or/and delta functions. The model used to construct the synthetic spectrum of CV in this database is not specified in the literature. The spectrum created with an incorrect model used may not coincide with the spectrum obtained by the measurement method. In addition, if the molecule has a degenerate

transition, there may be deviations from degeneracy because the theoretical approach cannot distinguish it.

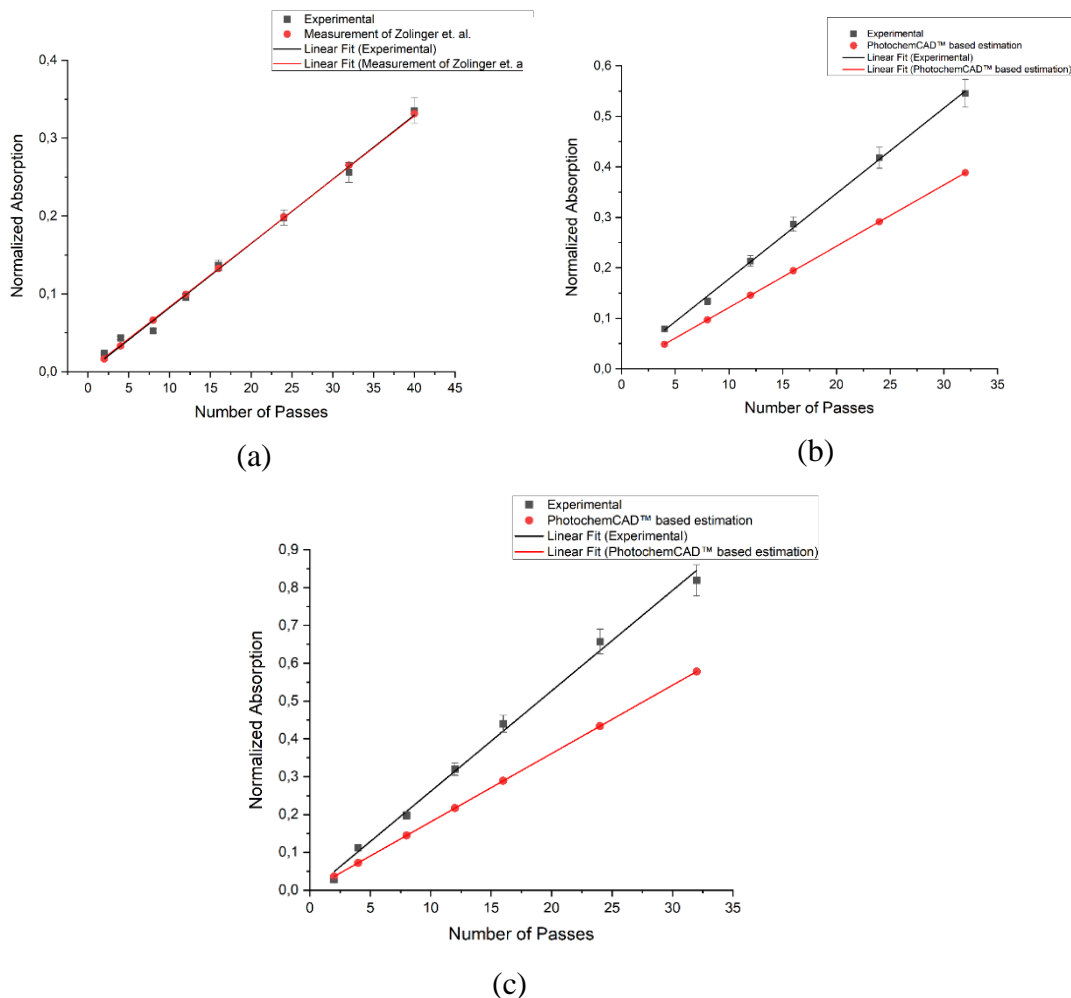


Figure 58 The normalized absorption vs number of passes graph of crystal violet with the concentration of 10^{-8} M at 509.5 nm (a) at 545.2 nm (b) at 592.0 nm wavelengths.

The wavelength dependent dispersion effects should also be taken account. If the wavelength approaches an absorption resonance, the refractive index is dominated by the molecule. The absorption of the molecule is determined by the complex part of the refractive index which is absorption coefficient k . According to the Kramer-Kronig relationship, where k increases, the real part of the refractive index, n , also

changes. Since absorption is observed at the measured wavelengths, k has a different value from 0, so n should also be high. As the wavelength coincides with the absorption resonances of the molecule, the index of refraction of the solution should be taken into account rather than the index of refraction of the liquid it is in. The concentration of the molecule in the solution determines the effective index of that solution which may be increased too much. According to Snell's law, when the refractive index increases, the physical path changes.

Furthermore, during the experiment, the quartz cuvette was tilted slightly off-axis to minimize unwanted scattering from surfaces. Therefore, the laser beam, which is already off-axis, had to travel more distance than 5 cm in the cuvette for each passage which leads to increase in optical path. Therefore, both the physical and optical path of the light beam can vary depending on the angle of the light entering the cuvette, the angle of the cuvette relative to the axis, and the diffraction effects caused by the molecule. As a result, the necessity of calculating the distance the light takes in the experiments to be carried out with the cuvette can be considered as a potential drawback of this system.

Despite this limited passage numbers obtained by 4x4 matrix arrangement, the detection limit of CV was calculated as 2.48×10^{-9} M which is competitive with traditional detection techniques. In Figure 45, the spectrally averaged absorption vs concentration graph of CV for 32 passes is given. The red line indicates the background noise level which is the minimum amount of absorption that the system is able to detect.

As the multiplication factor of multi-pass measurement system is directly proportional to the number of pass, with a proper coating that provides extensive optical path, the multi-pass measurement technique may become competitive with state of art, surface enhanced raman scattering (SERS) whose multiplication factor is determined by the electromagnetic and chemical field enhancement. Furthermore, if the loss caused by the system itself are eliminated, it would be possible to measure molecules with lower concentration by enhancing the dynamic range. While, SERS

is able to detect samples even at the single molecule level, multi-pass measurement technique is only effective for collective atmospheric and fluid samples.

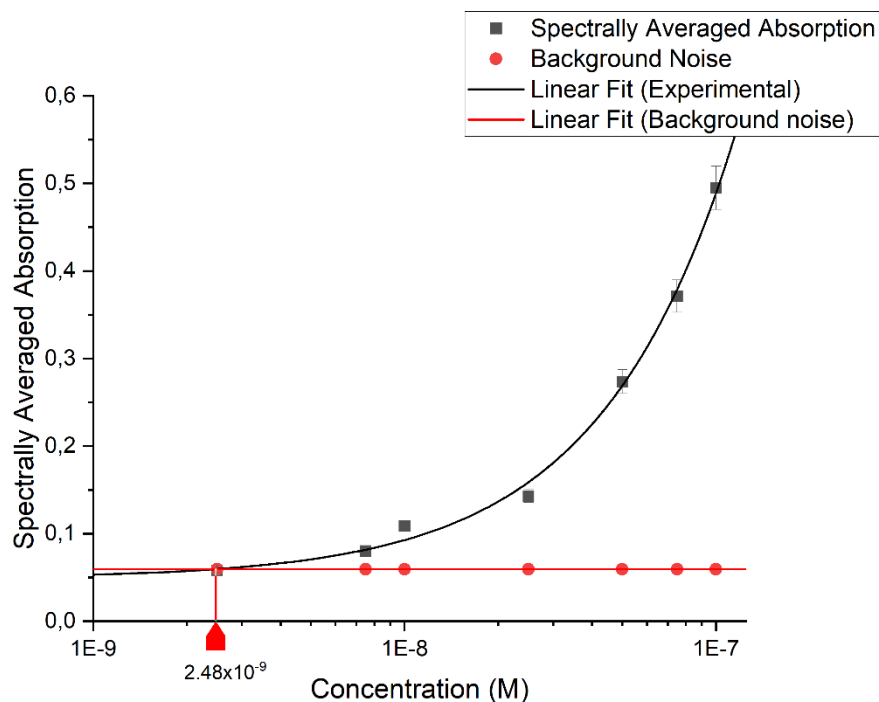


Figure 59 Spectrally averaged absorption vs concentration graph of Crystal Violet.

Since the smallest detectable molarity is 2.48×10^{-9} , there are a total of 1.48×10^{-9} moles of CV molecules in the 0.6 liter cuvette. But actually the number of moles measured is equal to the number of moles in the cross section through which the beam passes. Since the cuvette is placed close to the objective mirrors, we can roughly assume that the laser beam passes in a cylindrical shape without taking into account the gaussian. In this case, the volume of the laser beam, which passes 32 times through the 5 cm long cuvette, will be 5024 mm^3 . In this volume, the laser beam was absorbed by an average of 1.24×10^{-11} moles, ie 7.46×10^{12} molecules CV.

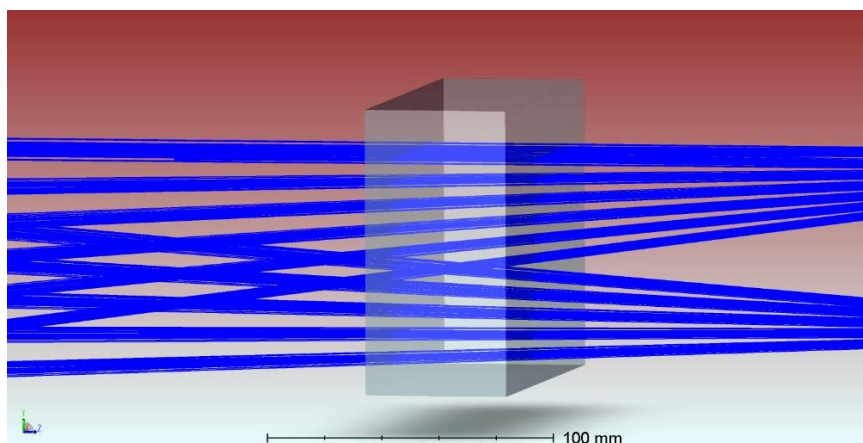


Figure 60 Laser beam passages through cuvette obtained by OpticStudio software.

However, as SERS requires extra time to prepare the samples and special operators, multi-pass system is operationally simple and does not require prior preparation. In addition, the cost of multi-pass system is dramatically lower than SERS.

The table below shows the comparison of general features, positive and negative aspects of several methods developed to detect trace amount of crystal violet.

Table 16 Comparison of different methods to detect trace amount of crystal violet.

<i>Method/ Property</i>	<i>Measurement time</i>	<i>Sensitivity</i>	<i>Operational Simplicity</i>	<i>Low cost</i>	<i>Amount of sample</i>
SERS	+ ₂₁ - ₂₇	+ ₂₇ + ₃₀	- ₂₅	- ₂₁ - ₂₇	+ ₂₉
Fluorescence	- ₂₀ + ₂₆	+ ₂₀	+ ₂₀ + ₂₆	- ₂₆ + ₂₀ - ₂₆	+ ₂₆
Spectrophotometry	- ₂₀ - ₂₁ + ₂₄	+ ₂₄	- ₂₀ + ₂₄	+ ₆₅ + ₂₄ - ₂₁	+ ₂₄
Electrochemi-luminescence	+ ₂₁	+ ₂₁	+ ₂₁	+ ₆₅	+ ₂₁
HPLC	- ₂₀ - ₂₆	+ ₆₆	- ₂₀ - ₂₆	+ ₆₅	+ ₆₄
Multi-pass Spectrometry	+	+	+	+	-

A similar extinction spectra measurement was repeated for PP type microplastics to calculate the limit of detection value indicated in Figure 62. In the experiment, which was carried out according to the microplastic concentration from 10^{-4} M to 10^{-6} M, a 32-pass test setup was used again. Since the measurement for 10^{-6} M crystal violet was below the background noise level, the lowest concentration that the system could measure, was calculated as 1.68×10^{-5} M.

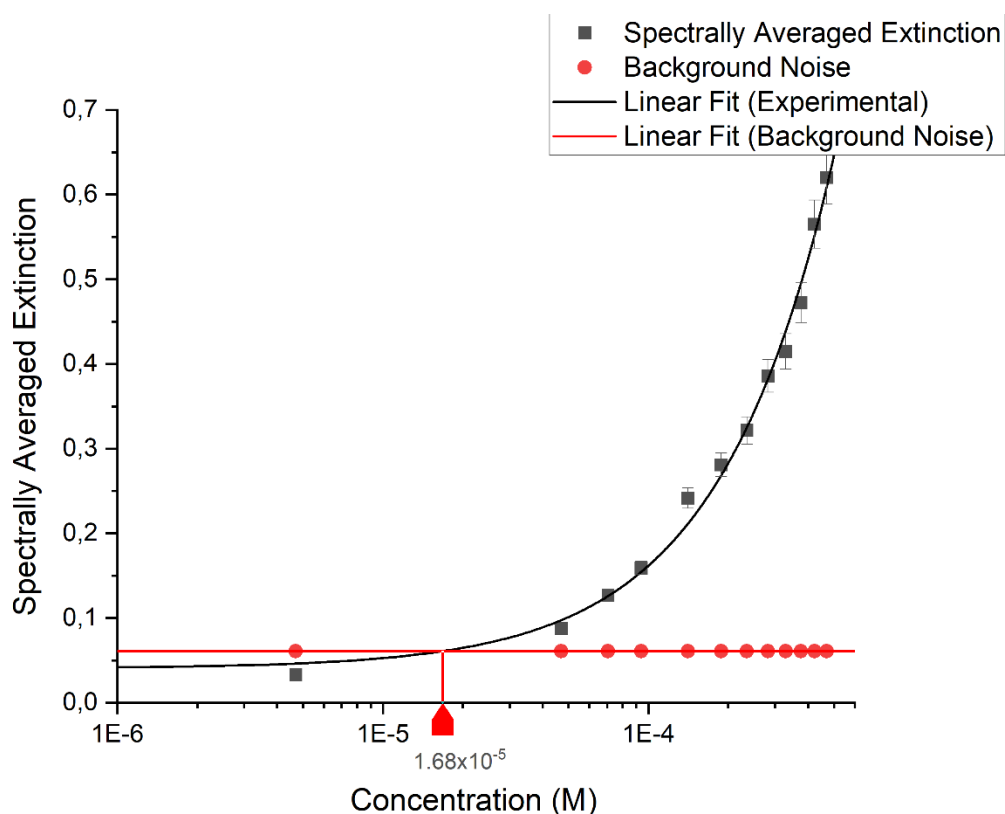


Figure 61 Spectrally averaged extinction vs concentration graph of PP type microplastics.

For microplastics, extinction is due not only to absorption and single particle scattering, but also to cluster scattering as they tend to agglomerate. While photons are less likely to interact with individual scattering microparticles, they may not escape scattering microparticles in clusters due to the photon-trap effect. According to Rayleigh scattering, for very small dielectric particles compared to wavelength, it

will show very weak scattering behavior as it is directly proportional to the particle size. If the wavelength of the light source to be used in the measurement does not coincide with the internal frequency of the material, it may not be measured.

Since the multi-pass optical system cannot distinguish the extinction whether it is caused by absorption or scattering, it would not be a perfect detection technique for samples showing characteristics of both absorber and scatterer. However, in trace gas absorption studies of atmosphere, it is not such a case since the scattering is almost negligible.

In the future, it is planned to setup a state of art atmospheric trace gas measurement chamber with complementary optics and optomechanics capable of operating in extreme temperature, pressure and humidity conditions. The multi-pass mirror system will be combined with the broadband transmissive windows of the atmospheric trace gas chamber and the tunable laser spectroscopy system, which includes spectrometers, photodetectors and lock-in amplifier located outside the system. Performance analysis of the multi-pass mirror system will be carried out according to the different environmental conditions to be created within the system. The spectra of gases with different absorption bands will be measured and analyzed in a controlled manner at various temperature and pressure configurations. The durability of optomechanics and optical aberrations due to vibration caused by mixing fans and vacuum pumps planned to be placed in the system will be evaluated. According to the analysis results, the vacuuming and gas mixing procedure that will not damage the optics, optomechanics and optical signal will be determined and the system will be put into use. If the multi-pass matrix system can still function satisfactorily in the harsh conditions inside the chamber, the system will continue to operate with regular maintenance. Otherwise the design will be repeated with the new design parameters.

REFERENCES

- [1] Chernin, S. M.; Barskaya, E. G. (1991). *Optical multi-pass matrix systems*. *ao/30/1/ao-30-1-51.pdf*, 30(1), 51–0. doi:10.1364/AO.30.000051
- [2] *OpticStudio*. Zemax. (n.d.). <https://www.zemax.com/pages/opticstudio>.
- [3] A. Rogalski and K. Chrzanowski, “*Infrared Devices and Techniques*”, *Opto-Electronics Review*, 2002, Vol. 10, pp 111-136
- [4] Daniels, A. (2018). Planck’s Radiation Law. In *Field guide to infrared optics, materials, and radiometry*. essay, SPIE Press.
- [5] Infrared signature prediction software. (n.d.). <http://www.thermofluids.co.uk/fe-mview2.php>.
- [6] Liou, K. (2002). *An introduction to atmospheric radiation*. Amsterdam: Academic Press.
- [7] A. Berk, P. Conforti, R. Kennett, T. Perkins, F. Hawes, and J. van den Bosch, “*MODTRAN6: a major upgrade of the MODTRAN radiative transfer code*,” Proc. SPIE 9088, Algorithms and Technologies for Multispectral, Hyperspectral, and Ultraspectral Imagery XX, 90880H (June 13, 2014); doi:10.1117/12.2050433.
- [8] U.S. Standard Atmosphere, 1976, U.S. Government Printing Office, Washington, D.C., 1976
- [9] I.E. Gordon, L.S. Rothman, C. Hill et. al., “The HITRAN2016 Molecular Spectroscopic Database”, *Journal of Quantitative Spectroscopy and Radiative Transfer* 203, 3-69 (2017).

- [10] Vaidyanathan, Mohan (1998). *Spectral band selection and classifier design for a multispectral imaging laser radar*. *Optical Engineering*, 37(3), 752–. doi:10.1117/1.601907
- [11] Isaksen, I., Granier, C., Myhre, G., Berntsen, T., Dalsøren, S., Gauss, M., . . . Wuebbles, D. (2009). *Atmospheric composition change: Climate–Chemistry interactions*. *Atmospheric Environment*, 43(33), 5138-5192. doi:10.1016/j.atmosenv.2009.08.003
- [12] Laj, P., Klausen, J., Bilde, M., Plaß-Duelmer, C., Pappalardo, G., Clerbaux, C., . . . Zardini, A. (2009). *Measuring atmospheric composition change*. *Atmospheric Environment*, 43(33), 5351-5414. doi:10.1016/j.atmosenv.2009.08.020
- [13] Cabib, D., Gil, A., & Biran, O. (2010). *Complete affordable system for simultaneous VIS/NIR and MWIR/LWIR spectral atmospheric transmittance measurements (ATMS)*. *Atmospheric Propagation VII*. doi: 10.1117/12.850078
- [14] L. S. Rothman, “*The evolution and impact of the HITRAN molecular spectroscopic database*“, *J. Quant. Spectrosc.* 111, 1565-1567 (2010)
- [15] Zhu M., Zhang F., Li W., Wu Y., Xu N., “*The impact of various HITRAN molecular spectroscopic databases on infrared radiative transfer simulation*“, *J. Quant. Spectrosc.* 234, 55-63 (2019)
- [16] Taniguchi, Masahiko; Du, Hai; Lindsey, Jonathan S. (2017). *PhotochemCAD 3: Diverse Modules for Photophysical Calculations with Multiple Spectral Databases*. *Photochemistry and Photobiology*, (), -. doi:10.1111/php.12862
- [17] Lu, X. W.; Dang, Z.; Yang, C. (2009). *Preliminary investigation of chloramphenicol in fish, water and sediment from freshwater aquaculture pond*. *International Journal of Environmental Science & Technology*, 6(4), 597–604. doi:10.1007/BF03326100

- [18] L. He, N.J. Kim, H. Li, Z. Hu, M. Lin, Use of a fractal-like gold nanostructure in surface-enhanced Raman spectroscopy for detection of selected food contaminants, *J. Agric. Food Chem.* 56 (2008) 9843–9847.
- [19] Keqiang Lai; Yuanyuan Zhang; Rui Du; Fuli Zhai; Barbara A. Rasco; Yiqun Huang (2011). *Determination of chloramphenicol and crystal violet with surface enhanced Raman spectroscopy.* , 5(1), 19–24. doi:10.1007/s11694-011-9106-8
- [20] Han, Y., Chen, Y., Liu, J., Niu, X., Ma, Y., Ma, S., & Chen, X. (2018). Room temperature synthesis of yellow-emitting fluorescent silicon nanoparticles for sensitive and selective determination of crystal violet in fish tissues. *Sensors and Actuators B: Chemical*, 263, 508–516. <https://doi.org/10.1016/j.snb.2018.02.163>
- [21] Lan, Q., Li, Q., Zhang, X., & Chen, Z. (2018). A novel electrochemiluminescence system of CUS film and k₂s₂o₈ for determination of crystal violet. *Journal of Electroanalytical Chemistry*, 810, 216–221. <https://doi.org/10.1016/j.jelechem.2018.01.008>
- [22] Shi, G., Wang, M., Zhu, Y., Wang, Y., & Xu, H. (2018). A novel natural SERS system for crystal VIOLET detection based on graphene oxide WRAPPED AG Micro-islands SUBSTRATE fabricated from lotus Leaf as a template. *Applied Surface Science*, 459, 802–811. <https://doi.org/10.1016/j.apsusc.2018.08.065>
- [23] Zhou, Z., Fu, Y., Qin, Q., Lu, X., Shi, X., Zhao, C., & Xu, G. (2018). Synthesis of magnetic mesoporous metal-organic framework-5 for the effective enrichment of malachite green and crystal violet in fish samples. *Journal of Chromatography A*, 1560, 19–25. <https://doi.org/10.1016/j.chroma.2018.05.016>
- [24] Sadeghi, S., & Nasehi, Z. (2018). Simultaneous determination of brilliant green and CRYSTAL VIOLET dyes in fish and water samples with dispersive liquid-liquid micro-extraction using ionic liquid followed by zero crossing first derivative

spectrophotometric analysis method. *Spectrochimica Acta Part A: Molecular and Biomolecular Spectroscopy*, 201, 134–142. <https://doi.org/10.1016/j.saa.2018.04.061>

[25] Yan, X., Wang, M., Sun, X., Wang, Y., Shi, G., Ma, W., & Hou, P. (2019). Sandwich-like Ag@Cu@CW SERS substrate with tunable nanogaps and component based on The PLASMONIC NANONODULE structures for sensitive detection crystal violet and 4-aminothiophenol. *Applied Surface Science*, 479, 879–886. <https://doi.org/10.1016/j.apsusc.2019.02.072>

[26] Hu, Y., & Gao, Z. (2020). Yellow emissive se,n-codoped carbon dots toward sensitive fluorescence assay of crystal violet. *Journal of Hazardous Materials*, 388, 122073. <https://doi.org/10.1016/j.jhazmat.2020.122073>

[27] Yang, G., Fang, X., Jia, Q., Gu, H., Li, Y., Han, C., & Qu, L.-L. (2020). Fabrication of Paper-based SERS substrates by Spraying silver and gold nanoparticles for sers determination of malachite GREEN, methylene blue, and crystal violet in fish. *Microchimica Acta*, 187(5). <https://doi.org/10.1007/s00604-020-04262-2>

[28] Wu, X., Si, S., Tan, W., Lu, X., Ye, F., & Zhao, S. (2021). Preparation of magnetic mesoporous metal-phenolic coordination spheres for extraction of crystal violet and leuco-metabolites in fish. *Journal of Chromatography A*, 1636, 461776. <https://doi.org/10.1016/j.chroma.2020.461776>

[29] Wang, K., Sun, D.-W., Pu, H., & Wei, Q. (2021). Polymer multilayers enabled stable and FLEXIBLE Au@Ag NANOPARTICLE array for nondestructive SERS detection of pesticide residues. *Talanta*, 223, 121782. <https://doi.org/10.1016/j.talanta.2020.121782>

[30] Miao, Y., Yang, K., Zong, S., Wang, Z., & Cui, Y. (2021). Au/Ag bimetallic Nanocuboid SUPERLATTICES coated WITH Ti3C2 NANOSHEETS for Surface-enhanced Raman SPECTROSCOPY detection of Fish DRUG residues in pond

water. *ACS Applied Nano Materials*, 4(7), 6844–6851.
<https://doi.org/10.1021/acsnm.1c00905>

[31] Wei, W.-xian, Xi, Z.-qian, & Huang, Q.-li. (2021). Fabrication of SERS-active AU@AU@AG DOUBLE shell nanoparticles for LOW-ABUNDANCE pigment detection. *Chinese Journal of Chemical Physics*, 34(2), 197–202.
<https://doi.org/10.1063/1674-0068/cjcp2005062>

[32] Hammer, M.H.S. Kraak and J.R. Parsons D.M. Whitacre (Ed.), *Reviews of Environmental Contamination and Toxicology*, Springer New York, New York, NY (2012), pp. 1-44

[33] Matthew Cole; Pennie Lindeque; Claudia Halsband; Tamara S. Galloway (2011). *Microplastics as contaminants in the marine environment: A review*. , 62(12), 2588–2597. doi:10.1016/j.marpolbul.2011.09.025

[34] Thompson, R. C.; Moore, C. J.; vom Saal, F. S.; Swan, S. H. (2009). *Plastics, the environment and human health: current consensus and future trends*. *Philosophical Transactions of the Royal Society B: Biological Sciences*, 364(1526), 2153–2166. doi:10.1098/rstb.2009.0053

[35] Lv, L.; He, L.; Jiang, S.; Chen, J.; Zhou, C.; Qu, J.; Lu, Y.; Hong, P.; Sun, S.; Li, C. In situ surface-enhanced Raman spectroscopy for detecting microplastics and nanoplastics in aquatic environments. *Sci. Total Environ.* **2020**, 728, 138449

[36] Ornik, J.; Sommer, S.; Gies, S.; Weber, M.; Lott, C.; Balzer, J.C.; Koch, M. Could photoluminescence spectroscopy be an alternative technique for the detection of microplastics? First experiments using a 405 nm laser for excitation. *Appl. Phys. B Lasers O* **2020**, 126, 1–7.

- [37] Takahashi, T.; Liu, Z.; Thevar, T.; Burns, N.; Mahajan, S.; Lindsay, D.; Watson, J.; Thornton, B. Identification of microplastics in a large water volume by integrated holography and Raman spectroscopy. *Appl. Opt.* **2020**, *59*, 5073–5078.
- [38] White, J. U. (1942). *Long Optical Paths of Large Aperture*. *Journal of the Optical Society of America*, *32*(5), 285. doi:10.1364/josa.32.000285
- [39] Grassi, L., & Guzzi, R. (2001). *Theoretical and practical consideration of the construction of a zero-geometric-loss multiple-pass cell based on the use of monolithic multiple-face retroreflectors*. *Applied Optics*, *40*(33), 6062. doi:10.1364/ao.40.006062 Allmendinger, R. W.1999. Introduction to Structural Geology. Lecture notes. 279 p.
- [40] Bernstein, H. J.; Herzberg, G. (1948). *Rotation-Vibration Spectra of Diatomic and Simple Polyatomic Molecules with Long Absorbing Paths. I. The Spectrum of Fluoroform (CHF₃) from 2.4 μ to 0.7 μ* . *The Journal of Chemical Physics*, *16*(1), 30–. doi:10.1063/1.1746650
- [41] Tobin, David C.; Strow, L. Larrabee; Lafferty, Walter J.; Olson, W. Bruce (1996). *Experimental investigation of the self- and N₂-broadened continuum within the ν_2 band of water vapor*. *ao/35/24/ao-35-24-4724.pdf*, *35*(24), 4724–0. doi:10.1364/AO.35.004724
- [42] David R. Glowacki, Andrew Goddard, and Paul W. Seakins, "Design and performance of a throughput-matched, zero-geometric-loss, modified three objective multi-pass matrix system for FTIR spectrometry," *Appl. Opt.* *46*, 7872-7883 (2007)
- [43] Shetter, R. E.; Davidson, J. A.; Cantrell, C. A.; Calvert, J. G. (1987). *Temperature variable long path cell for absorption measurements*. *Review of Scientific Instruments*, *58*(8), 1427–. doi:10.1063/1.1139426

- [44] Horn, D.; Pimentel, G. C. (1971). *25-km Low-Temperature Multiple-Reflection Cell*. *ao/10/8/ao-10-8-1892.pdf*, 10(8), 1892–0. doi:10.1364/AO.10.001892
- [45] Herriott, Donald R.; Schulte, Harry J. (1965). *Folded Optical Delay Lines*. *ao/4/8/ao-4-8-883.pdf*, 4(8), 883–0. doi:10.1364/AO.4.000883
- [46] Doussin, Jean-François; Dominique, Ritz; Patrick, Carlier (1999). *Multiple-Pass Cell for Very-Long-Path Infrared Spectrometry*. *ao/38/19/ao-38-19-4145.pdf*, 38(19), 4145–0. doi:10.1364/AO.38.004145
- [47] J. White, “Very long optical paths in air,” *J. Opt. Soc. Am.* **66**, 411–416 (1976).
- [48] D. Ritz, M. Hausmann, and U. Platt, “Improved open multireflection cell for the measurement of NO₂ and NO₃,” in *Optical Methods in Atmospheric Chemistry*, H. I. Schiff and U. Platt, eds., *Proc. SPIE 1715*, 200–211 ~1992!.
- [49] Steyert, D. W., Sirota, J. M., Mickelson, M. E., & Reuter, D. C. (2001). *Two new long-pass cells for infrared and visible spectroscopy*. *Review of Scientific Instruments*, 72(12), 4337–4343. doi:10.1063/1.1409565
- [50] S. Chernin, “Promising version of the three-objective multi-pass matrix system,” *Opt. Express* **10**, 104–107 (2002).
- [51] *Metallic mirror Coatings: Edmund Optics*. Edmund Optics Worldwide. (n.d.). <https://www.edmundoptics.com/knowledge-center/application-notes/optics/metallic-mirror-coatings/>.
- [52] *Exploring non-sequential mode In opticstudio*. Knowledgebase. (n.d.). <https://support.zemax.com/hc/en-us/articles/1500005487761-Exploring-Non-Sequential-Mode-in-OpticStudio>
- [53] *Superk compact supercontinuum lasers - nkt photonics*. LASERS & FIBERS. (2021, July 30). <https://www.nktphotonics.com/lasers-fibers/product/superk-compact-supercontinuum-lasers/>.

[54] Goodwin, E. P., Wyant J. C., *Field Guide to Interferometric Optical Testing*, SPIE Press, Bellingham, WA (2006).

[55] *How to perform a non-sequential tolerance analysis*. Knowledgebase. (n.d.).
<https://support.zemax.com/hc/en-us/articles/1500005575322-How-to-perform-a-Non-Sequential-tolerance-analysis>.

[56] J.M. Bennett, L. Mattsson, *Introduction to Surface Roughness and Scattering*, Pg 3, OSA, Washington. DC, 1993

[57] Ralf Jedamzik, Thorsten Doehring, Rolf Mueller, and Peter Hartmann "*Homogeneity of the coefficient of linear thermal expansion of ZEDRODUR*", Proc. SPIE 5868, *Optical Materials and Structures Technologies II*, 58680S (18 August 2005); <https://doi.org/10.1117/12.614424>

[58] Kelsey A. Folgner, Chung-Tse Chu, Scott D. Sitzman, Sean C. Stuart, Zachary R. Lingley, and James D. Barrie, "*Development and growth of corrosion features on protected silver mirrors during accelerated environmental exposure*," *Appl. Opt.* 59, A187-A197 (2020)

[59] *Article NO.: 700-061-10. Large cells 700-061-10.* (n.d.).
https://www.hellma.com/en/laboratory-supplies/cuvettes/cuvette-finder/cuvette/?tx_rlhellma_cuvetteplugin%5Bcuvette%5D=223&tx_rlhellma_cuvetteplugin%5Baction%5D=show&tx_rlhellma_cuvetteplugin%5Bcontroller%5D=Cuvette&cHash=dc0c2c3d364d77d2564cf763f3a22963.

[60] Zollinger, H. (1987) *Color Chemistry: Syntheses, Properties and Applications of Organic Dyes and Pigments*, VCH Verlagsgesellschaft mbH, Weinheim, Federal Republic of Germany.

- [61] Taniguchi, Masahiko; Lindsey, Jonathan S. (2017). *Database of Absorption and Fluorescence Spectra of >300 Common Compounds for use in PhotochemCAD*. *Photochemistry and Photobiology*, (), -. doi:10.1111/php.12860
- [62] McNaught, A. D., & Wilkinson, A. (2000). *Iupac compendium of chemical terminology*. Royal Society of Chemistry.
- [63] *Best optical Coating services by ESCO Optics, Inc.* Esco Optics, Inc. (n.d.). <https://escooptics.com/pages/coatings>.
- [64] John L. Allen; Jeffery R. Meinertz (1991). *Post-column reaction for simultaneous analysis of chromatic and leuco forms of malachite green and crystal violet by high-performance liquid chromatography with photometric detection*. , 536(*none*), 217–222. doi:10.1016/s0021-9673(01)89252-9
- [65] A. Asfaram; M. Ghaedi; A. Goudarzi; M. Soylak; S. Mehdizadeh Langroodi (2015). *Magnetic nanoparticles based dispersive micro-solid-phase extraction for the determination of malachite green in water samples: Optimized experimental design*. , (), -. doi:10.1039/C5NJ01730K
- [66] Zhang, Leilei; Zhang, Yiying; Tang, Yurong; Li, Xiaorong; Zhang, Xinfeng; Li, Chaobi; Xu, Shuxia (2018). *Magnetic solid-phase extraction based on Fe₃O₄ graphene oxide nanoparticles for the determination of malachite green and crystal violet in environmental water samples by HPLC*. *International Journal of Environmental Analytical Chemistry*, (), 1–14. doi:10.1080/03067319.2018.1441837

APPENDIX A

SPECIFICATIONS

Optical

Repetition rate [Hz]	Variable 1 Hz to min. 20 kHz
Spectral coverage [nm]	450-2400
Total power [mW] ²⁾	> 110
Total visible power (450-850 nm) [mW] ²⁾	> 20
Total power stability [%] ¹⁾	< ± 1.0
Output pulse width [ns]	< 2
Pulse-pulse jitter (standard dev.) [µs] ²⁾	< 2
Polarization	Unpolarized
Beam quality, TEM ₀₀	M ² < 1.1
Beam diameter, collimated [mm]	1 @ 530 nm 2 @ 1100 nm 3 @ 2000 nm

1) Contact us for ± 0.5 %.

2) Repetition rate dependent.